

Politecnico di Torino

Master's degree in Mechanical Engineering

A.Y. 2024/2025

Graduation session March/April 2025



**Multibody study of tracked
vehicle's dynamics and track
chain modeling.**

Supervisors:

GALVAGNO ENRICO (DIMEAS)

VENTURINI SIMONE (DIMEAS)

DIMAURO LUCA (DIMEAS)

VELARDOCCHIA MAURO (DIMEAS)

Candidate:

ANDI COBA S305855

Abstract

This thesis has two main objectives. The first one is the study of the tracked vehicle's upper portion of chain under static conditions, by using Adams Tracked Vehicle (ATV), a toolkit of the Adams Car multibody software. The results of the ATV simulation will serve as the benchmark, against which results obtained by modeling the chain using different analytical tools will be compared. This analytical approach has the great advantage of providing satisfactory results, while needing few inputs and being very cost effective and easy to implement.

The second goal is that of studying the dynamic behavior of the tracked vehicle. More specifically, the vertical dynamics of the default vehicle model will be studied by analyzing the frequency content of the road profile and the vehicle's vertical acceleration. Certain parameters of the vehicle model will then be modified and the simulation will be repeated, in order to understand the influence and importance of the said modification. In this way, a comprehensive study of the vertical dynamics can be realized and the contribution of the most important parameters be evaluated.

Acknowledgments

I would like to express my gratitude to Prof. Galvagno, Ing. Dimauro and Ing. Venturini for their invaluable support and advice throughout these past months. Without their guidance, this thesis would not have been possible.

I would like to thank my dear friends, Fiorelo, Elio, Genald, Bogachan, Andi, Robert and Samuel, for always being there to support me throughout these challenging university years.

Finally, the biggest gratitude goes towards my entire family. It is only thanks to their patience, support, discipline, and most importantly, the motivation they instilled in me from a young age that I have been able to become a mechanical engineer.

Andi Coba, Torino 2025

Table of Contents

Abstract.....	3
Acknowledgments.....	5
List of tables	9
List of figures.....	11
Acronyms	15
1 Introduction	16
1.1 Introduction and literature review.	16
1.2 ATV default tank model.....	21
2 Track chain modeling.....	22
2.1 Geometrical data of the model.....	23
2.2 ATV simulation results.....	25
2.3 Modeling the track chain vertical bending behavior.	35
2.3.1 Continuous string in tension with analytically evaluated tension.....	35
2.3.2 Continuous string in tension with ATV provided tension.....	37
2.3.3 Longitudinal bending discrete model.	38
2.4 Modeling the track chain torsional behavior.....	45
2.5 Modeling the track chain lateral bending behavior.....	48
2.5.1 Euler-Bernoulli beam model.	48
2.5.2 Discrete modeling of the chain lateral bending.	52
2.6 Summarizing the modeling results.....	59
3 Sensitivity analysis	67
3.1 Rotational stiffness modification.	67
3.2 Rotational damping modification.	72
3.3 Unload angle modification.	78
4 Modified tank model	84
4.1 Geometrical data of the modified model.	85
4.2 ATV simulation results.....	86
4.3 Modeling the track chain vertical bending behavior.	93
4.3.1 Continuous string with analytically evaluated tension.....	93
4.3.2 Continuous string with ATV provided tension.....	95

4.4	Modeling the track chain torsional behavior.....	96
4.5	Modeling the track chain lateral bending behavior.....	98
4.6	Summarizing the results for the modified tank model.....	103
5	Vertical dynamics of the tracked vehicle.....	104
5.1	Generating the road profile.....	107
5.2	Setting the simulation.....	113
5.3	Simulation results.....	115
5.3.1	Tensioner force variation.....	117
5.3.2	Rotational springs stiffness variation.....	119
5.3.3	Rotational damping coefficient variation.....	120
5.3.4	Frequency response of the system.....	122
6	Conclusions.....	129
	Appendix A.....	134
A.1	ATV simulation setup for the static frequency analysis.....	134
A.2	ATV simulation setup for the vertical dynamics study of the tracked vehicle.....	139
	Appendix B.....	143
B.1	Procedure to obtain the natural frequency of the equivalent continuous string in tension.....	143
B.2	Procedure to obtain the natural frequency of the equivalent shaft in torsion model.....	145
B.3	Procedure to obtain the natural frequency expression of the equivalent Euler-Bernoulli beam model.....	149
	References.....	152

List of tables

Table 2.1. Geometrical data of the default tank model's components.....	23
Table 2.2. Properties of segments 1 and 2.	24
Table 2.3. Simulation results for chain vertical bending.	31
Table 2.4. Simulation results for chain lateral bending.	31
Table 2.5. Simulation results for chain torsion.	32
Table 2.6. Tension on strings 1 and 2, as a function of the idle wheel tension.	36
Table 2.7. The first five analytical frequencies for strings 1 and 2.	37
Table 2.8. The first five natural frequencies for strings 1 and 2, with ATV tension values.	38
Table 2.9. Results summary for segment 1.	42
Table 2.10. Results summary for segment 2.	43
Table 2.11. The first five harmonics for the torsion model.	47
Table 2.12. Comparison between the analytical and simulation results for torsion.	47
Table 2.13. The first five analytical natural frequencies for the chain lateral bending....	51
Table 2.14. Comparison between the analytical and simulation results for chain lateral bending.	51
Table 2.15. Summary of the results obtained for the two models and simulation.	56
Table 2.16. Segment 1 results for vertical bending ((X-Z) plane).	59
Table 2.17. Segment 2 results for vertical bending ((X-Z) plane).	61
Table 2.18. Chain torsional oscillations results.....	62
Table 2.19. Chain lateral bending results.	64
Table 3.1. The left side shows the results of the original simulation, while the right side shows the results with the modified stiffness (3000 Nmm/°).....	68
Table 3.2. The left side shows the results of the original simulation, while the left side shows the results with the modified stiffness (30000 Nmm/°).....	70
Table 3.3. The left side shows the results of the default model, while the right side shows the results obtained with the modified damping (17.45 Nmms/°).	74
Table 3.4. The left side shows the results of the default model, while the right side shows the results obtained with the modified damping (174.45 Nmms/°).	75
Table 3.5. The left table shows the results of the original simulation (12°), whereas the right table shows the results with the modification (0°).	78
Table 3.6. The left table shows the results of the original simulation (12°), whereas the right table shows the results with the modification (24°).	81
Table 4.1. Geometrical data of the modified tank model.	85
Table 4.2. Data for each of the three segment of the upper chain.	86
Table 4.3. Simulation results for segment 1 vertical bending.	91
Table 4.4. Simulation results for segment 2 vertical bending.	92
Table 4.5. Simulation results for segment 3 vertical bending.	92
Table 4.6. Chain lateral bending simulation results.	92
Table 4.7. Chain torsion simulation results.	93
Table 4.8. The first five harmonics for the three strings in tension (analytically evaluated tension).	95

Table 4.9. The first five harmonics for the three segments, calculated with ATV tension values.	95
Table 4.10. The first five harmonics for the shaft in torsion model.	97
Table 4.11. Results summary for the modified tank model lateral bending.	101
Table 5.1. Dynamic model frequency collection.	124

List of figures

Figure 1.1. Free body diagram of the tracked vehicle in top view, as proposed by (Galvagno, et al., 2012) [2].....	17
Figure 1.2. Tank model proposed by (Lessem & Murphy, 1972) [3].	18
Figure 1.3. Experimental findings by (Lessem & Murphy, 1972) [3].	19
Figure 1.4. ATV default tank model.	21
Figure 2.1. Default ATV tank model reference frame.....	22
Figure 2.2. Table of eigenvalues.	26
Figure 2.3. ATV interface for mode shape animation.....	26
Figure 2.4. Segment 1 vertical bending first mode shape (2.53 Hz).....	27
Figure 2.5. Segment 2 vertical bending first mode shape (3.37 Hz).....	27
Figure 2.6. Segment 1 vertical bending second mode shape (4.27 Hz).	28
Figure 2.7. Segment 2 vertical bending second mode shape (6.32 Hz).	28
Figure 2.8. Segment 1 vertical bending third mode shape (6.58 Hz).	28
Figure 2.9. Segment 2 vertical bending third mode shape (9.76 Hz).	29
Figure 2.10. Chain lateral bending second mode shape (6.31 Hz).	29
Figure 2.11. Chain lateral bending third mode shape (12.22 Hz).....	29
Figure 2.12. Chain lateral bending fourth mode shape (19.6 Hz).	30
Figure 2.13. Chain torsion first mode shape (17.13 Hz).	30
Figure 2.14. Chain torsion second mode shapes (27.22 Hz).....	30
Figure 2.15. Chain torsion third mode shape (41.33 Hz).....	31
Figure 2.16. Simulation results for segment 1 vertical bending.....	32
Figure 2.17. Simulation results for chain torsion vertical bending.....	33
Figure 2.18. Simulation results for chain torsion.....	33
Figure 2.19. Simulation results for chain lateral bending.....	34
Figure 2.20. Force equilibrium around the idle wheel.	36
Figure 2.21. Schematic representation of the discrete MDOF chain model.	39
Figure 2.22. Boundary conditions on the chain extremes.....	39
Figure 2.23. FBD of the first, last and generic pad.....	40
Figure 2.24. Comparison between the modeling methods and simulation results for segment 1.....	43
Figure 2.25. . Comparison between the modeling methods and simulation results for segment 2.....	44
Figure 2.26. Similarity between a mode shape and its corresponding eigenvector.	45
Figure 2.27. Comparison between the analytical and simulation results for chain torsion.	47
Figure 2.28. Equilibrium around point O in the (X-Y) plane.	49
Figure 2.29. Graphical comparison between the analytical and simulation results for chain lateral bending.	51
Figure 2.30. Schematic representation of MDOF model for lateral bending.....	52
Figure 2.31. Schematic representation of the equivalent lumped spring.....	53
Figure 2.32. Free body diagrams of the track pads.	53
Figure 2.33. Graphical comparison between the models and simulation.....	57

Figure 2.34. Graphical representation between the discrete model and simulation.	57
Figure 2.35. Comparison between simulation mode shape and discrete model eigenvector.	58
Figure 2.36. Segment 1 vertical bending absolute error.	60
Figure 2.37. Segment 1 vertical bending relative error	60
Figure 2.38. Segment 2 vertical bending absolute error.	61
Figure 2.39. Segment 2 vertical bending relative error.	62
Figure 2.40. Chain torsion absolute error.	63
Figure 2.41. Chain torsion relative error.	63
Figure 2.42. Chain lateral bending absolute error.	64
Figure 2.43. Chain lateral bending relative error.	65
Figure 3.1. Local reference frame for the track segment.	67
Figure 3.2. Deviation between the original and modified results for an increase of two orders of magnitude.	69
Figure 3.3. Deviation between the original and modified results for an increase of three orders of magnitude.	69
Figure 3.4. Chain does not fully wrap around the wheels.	71
Figure 3.5. Track deformation for the z-direction stiffness of 300000 Nmm/°	71
Figure 3.6. Segment 1 vertical bending sensitivity to rotational bending.	72
Figure 3.7. Segment 2 vertical bending sensitivity to rotational bending.	73
Figure 3.8. Lateral bending sensitivity to rotational bending.	73
Figure 3.9. Torsion sensitivity to rotational damping.	74
Figure 3.10. Segment 1 vertical bending sensitivity to rotational damping.	76
Figure 3.11. Segment 2 vertical bending sensitivity to rotational damping.	76
Figure 3.12. Lateral bending sensitivity to rotational damping.	77
Figure 3.13. Torsion sensitivity to rotational damping.	77
Figure 3.14. Segment 1 vertical bending sensitivity to unload angle.	79
Figure 3.15. Segment 2 vertical bending sensitivity to unload angle.	79
Figure 3.16. Lateral bending sensitivity to unload angle.	80
Figure 3.17. Torsion sensitivity to unload angle.	80
Figure 3.18. Segment 1 vertical bending sensitivity to unload angle.	81
Figure 3.19. Segment 2 vertical bending sensitivity to unload angle.	82
Figure 3.20. Lateral bending sensitivity to unload angle.	82
Figure 3.21. Torsion sensitivity to unload angle.	83
Figure 4.1. Modified tank model.	84
Figure 4.2. Segment 1 vertical bending first mode shape (3.76 Hz).	87
Figure 4.3. Segment 1 vertical bending second mode shape (7.07 Hz).	87
Figure 4.4. Segment 1 vertical bending third mode shape (10.82 Hz).	87
Figure 4.5. Segment 2 vertical bending first mode shape (5.69 Hz).	88
Figure 4.6. Segment 2 vertical bending second mode shape (11.84 Hz).	88
Figure 4.7. Segment 2 vertical bending third mode shape (18.42 Hz).	88
Figure 4.8. Segment 3 vertical bending first mode shape (3.19 Hz).	89
Figure 4.9. Segment 3 vertical bending second mode shape (6.13 Hz).	89
Figure 4.10. Segment 3 vertical bending third mode shape (9.39 Hz).	89

Figure 4.11. Chain torsion first mode shape (18.13 Hz).	90
Figure 4.12. Chain torsion second mode shape (27.93 Hz).	90
Figure 4.13. Chain torsion third mode shape (40.61 Hz).	90
Figure 4.14. Chain lateral bending third mode shape (12.6 Hz).	91
Figure 4.15. Chain lateral bending fourth mode shape (16.5 Hz).	91
Figure 4.16. Force balance around the idle wheel.	94
Figure 4.17. Graphical comparison of the analytical and simulation results for the torsional behavior.	98
Figure 4.18. Graphical representation of the comparison between the analytical model results and simulation for chain lateral bending.	101
Figure 4.19. Lateral bending absolute error for the modified tank model.	102
Figure 4.20. Lateral bending relative error for the modified tank model.	102
Figure 5.1. Schematic representation of the 4 DOF car model.	104
Figure 5.2. Default tank model schematic representation.	105
Figure 5.3. "ride_quality_3inch_measured" road profile.	107
Figure 5.4. PSD of the road profile in space domain.	108
Figure 5.5. Left: spatial PSD of the road profile. Right: standard ISO road profiles [7]. ..	109
Figure 5.6. PSD of the road profile in time domain.	110
Figure 5.7. Temporal PSD of the road profile obtained with Welch's method.	110
Figure 5.8. Left: spectrogram of the road profile in space domain. Right: Magnification of the low frequency range.	111
Figure 5.9. The blue line shows the original road signal. The red line shows the road signal with the trend removed.	111
Figure 5.10. Spectrogram of the "detrended" signal.	112
Figure 5.11. Matching between the road PSD and spectrogram.	112
Figure 5.12. Velocity controller dialog window.	113
Figure 5.13. Road profile generation.	114
Figure 5.14. Sprung mass vertical acceleration in time.	115
Figure 5.15. The script used to obtain the acceleration PSD.	116
Figure 5.16. Center of gravity's vertical acceleration PSD.	116
Figure 5.17. RMS acceleration for the different tensioner force values.	117
Figure 5.18. PSDs for the different tensioner force values.	118
Figure 5.19. RMS acceleration for the different stiffness values.	119
Figure 5.20. PSD for the different stiffness values.	120
Figure 5.21. . RMS acceleration for the different damping values.	121
Figure 5.22. PSDs for the different damping values.	121
Figure 5.23. FRF of the vertical acceleration of the center of gravity.	123
Figure 5.24. FRF intersected with the frequencies.	124
Figure 5.25. Vertical acceleration PSD for the flat road simulation (only sprocket excitation).	126
Figure 5.26. Vertical acceleration PSD (sinusoidal road).	127
Figure 5.27. Time domain PSD of the sinusoidal road.	127
Figure 5.28. Response of the vehicle under combined excitation.	128
Figure A.0.1. Generating the default tank assembly.	134

Figure A.0.2. Performing the dynamic track wrapping.....	135
Figure A.0.3. Loading the road profile.	135
Figure A.0.4. Creating track segment requests.....	136
Figure A.0.5. Setting the tracked vehicle simulation.	137
Figure A.0.6. Modifying the simulation file to perform the modal analysis.....	138
Figure A.0.7. Reading the simulation results.	138
Figure A.0.8. Adding the velocity controller subsystem.	139
Figure A.0.9. Loading the rough road profile.....	140
Figure A.0.10. Setting the velocity controller parameters.	141
Figure A.0.11. Setting the simulation settings.....	142
Figure B.0.1. FBD of the string.	143

Acronyms

ATV

Adams Tracked Vehicles

FBD

Free Body Diagram

DOF

Degree of Freedom

MDOF

Multi-Degree of Freedom

EVP

Eigenvalue Problem

PDE

Partial Differential Equation

ODE

Ordinary Differential Equation

BC

Boundary Conditions

IC

Initial Conditions

TSL

Track Segment Link

PSD

Power Spectral Density

FRF

Frequency Response Function

FFT

Fast Fourier Transform

1 Introduction

1.1 Introduction and literature review.

Tracked vehicles have long been used in off-road applications, where the conventional vehicles equipped with pneumatic tires are not able to easily, if at all, perform the tasks that they otherwise excel at in paved surfaces. The need for tracked vehicles is relevant in many sectors, such as the construction, agriculture, forestry and mining industries. Also their use for recreational activities has increased, such as in snow mobiles and all-terrain side-by-sides, where users can enjoy the benefits of tracks to tackle the most difficult conditions.

An important sector where such vehicles are highly appreciated is the military, which has always been the one to push the technology forward. The stringent requirements of the combat vehicles' mission profiles require exceptional performance, in terms of weight carrying capacity, maneuverability, high speed runs and handling extreme terrain.

As used as these vehicles are, there is a general lack of models (at least compared to other conventional vehicles) to describe and simulate the behavior under different conditions. Many aspects of their dynamics are not properly studied or modeled, and the characterization is based on experimental tests and empirical models, which are obtained from the experience of engineers. As useful as the experimental tests are, they can be very expensive and time-consuming, especially in the design phase and they do not allow for minor modifications performed in real time.

This thesis aims at providing a dynamic model to study the vertical dynamics of the tracked vehicle and the frequency analysis of the track itself. It is the continuation of a long line of research of this university, whose aim is to achieve a complete and thorough understanding of these vehicles, by implementing different methodologies, and eventually providing the user a means by which to easily simulate the system of choice. The study of the terrain-track interaction, and consequently the tracked vehicles as a whole, is known as terramechanics and its foundations were laid by M. G. Bekker, who starting from the 1950s published a number of papers and books on the topic. His successor can be considered J. Y. Wong, who has also published many papers and is the author of the most prominent book on the topic.

The most complete book by (Wong, 2010)[1] is "Terramechanics and off-road vehicle engineering", where the author provides a thorough review of the methods of characterizing the vehicle and terrain, both experimentally and analytically. However, in this thesis, the vehicle-terrain interaction will not play an important part, as the vehicle will be studied on hard roads (dry asphalt), since the goal is the modeling and characterization of vehicle systems, rather than performance evaluation.

There are many dynamic models of tracked vehicles in the literature, typically of a tank, and what follows is a summary of some models which are quite interesting for the purposes of this thesis. It is important to underline that even though tracked vehicles

come in many types, the tank is the most interesting, as it can be quite heavy, while at the same time showing quite impressive dynamics, compared to the others. Close attention will be paid to the assumptions of these models, because they are the foundations of the simplified model that will be used to study the parameters of interest.

A very complete model was reported by (Galvagno, et al., 2012)[2], reported in Figure 1.1, which will be used as reference in this thesis, not only due to the association with that paper, but also because the nomenclature is the same that is customarily used in this university.

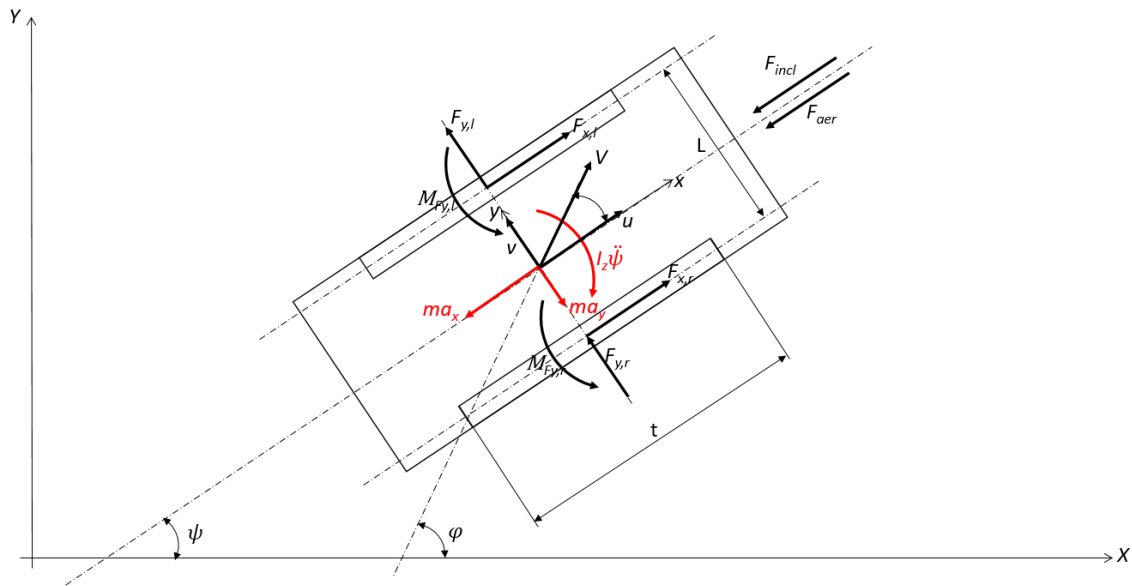


Figure 1.1. Free body diagram of the tracked vehicle in top view, as proposed by (Galvagno, et al., 2012) [2].

The authors introduce the following assumptions to their model (only the most important for the purposes of this work are reported below):

- Forces applied to the ground are concentrated under the road wheels.
- Smoother Coulomb friction model.
- Continuous track-terrain contact is discretized in a finite number of contact patches, equal to the number of road wheels. Contact patch forces are modeled as smoothed friction functions, depending on the longitudinal slip and sideslip angle of the tracks.
- Firm ground (sink effect is neglected).
- Cohesion of the track-terrain interface is neglected.
- Independent wheel suspension with the same vertical stiffness for each road wheel.
- Equal ground loading in static configuration.

Another interesting model is proposed in a technical report by (Lessem & Murphy, 1972)[3], who conducted a study on behalf of the US army. Even though the report is very old, the model they propose and the assumptions they make are useful, because they offer a realistic, yet simplified approach to modelling the vehicles under study. The report models the tank using coupled, second-order differential equations that describe the motion of each degree of freedom. The authors apply the Newtonian approach to obtain the equations of motion of the equivalent vehicle model, that consists of masses, springs and dampers. The assumptions they propose are the following:

- Mass elements are assumed to be rigid bodies.
- Spring elements are assumed to be of negligible mass and represent the elastic properties of the structure.
- Damping elements are assumed to have neither mass, nor elasticity, and represent the dissipative forces or energy losses of the system.
- The model has one degree of freedom for the pitch, one for the bounce, and one for each of the road wheels.
- The road wheels are represented by radially projecting linear springs. This takes into account the stiffness and deformation of the road wheel.
- The track compliance is represented by connecting the axles with springs. The authors call these systems “feelers” and in their model they are necessary, since the track is not included. This ensures that no important information is lost by neglecting the track.

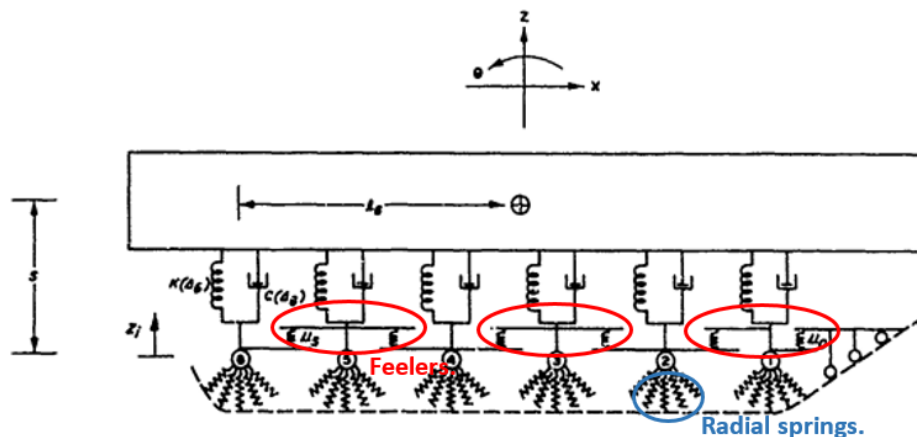


Figure 1.2. Tank model proposed by (Lessem & Murphy, 1972) [3].

A. S. Lessem and N. R. Murphy, Jr in their work obtain some very important conclusions, which will be useful to this thesis when studying the dynamic behavior of the tracked vehicle:

- There are no ranges of vehicle characteristics, velocities or obstacle sizes sufficiently broad to permit the neglect of track contributions to hull dynamics.

- Within the range of speeds studied, contributions of the track were usually most pronounced at low speeds and of lesser importance at the higher speeds.
- The nature of the suspension system significantly affects the track contribution to dynamics.
- The mathematical model for tracked vehicle dynamics, as developed by the authors, shows promise as a practical means for simulating the hull dynamics of tracked vehicles.

The following figure shows a clear picture of the distinction between the tests performed with and without the tracks. What is reported here is only one of the results the authors obtain, but it serves to show the distinction between the two scenarios. The graph is quite old, so additional information has been added to clarify its contents.

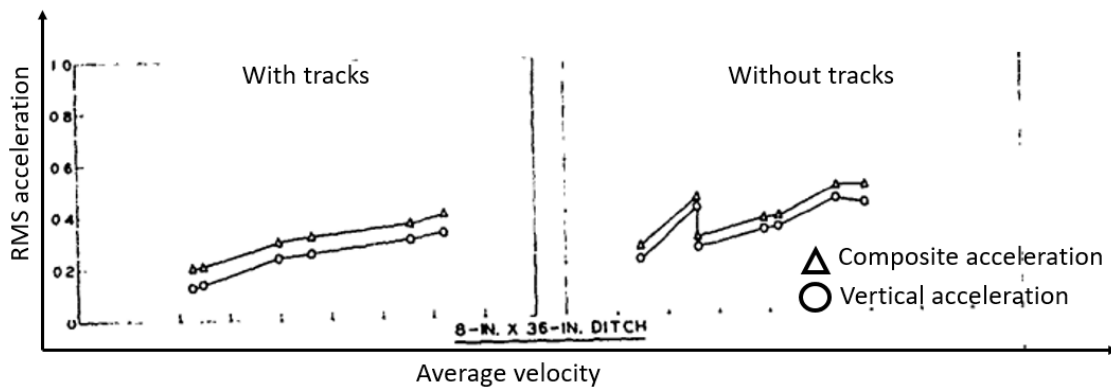


Figure 1.3. Experimental findings by (Lessem & Murphy, 1972) [3].

Another technical report that is quite useful to this work is “Methods for tracked vehicle modeling and simulation”, by (Madsen, et al., 2010)[4]. This report compares different software and methodologies that are used for tracked vehicle simulations, highlighting their advantages and disadvantages. In particular, it analyses the Adams ATV toolkit, which is a multi-body simulation tool that will be used in this thesis. More importantly, it summarizes some features of ATV that make it one of the best for studying tracked vehicles:

- It features a built-in routine that automatically wraps the track chain around the rolling elements.
- Force-based connection elements between track shoes that allow for compliance in the track chain.
- A method for switching between half-vehicle and full-vehicle models, assuming the model is symmetric along its centerline.
- The track chain can be made up of many rigid track shoes that allow for compliance in the track chain.
- A method for easy-switching between half-vehicle and full-vehicle models, assuming the model is symmetric along its centerline.

- The track chain can be made up of many rigid track shoes with compliant connection elements, or as one degree of freedom flexible band.
- Allows for the definition of custom road profiles.
- Both soft and rigid soil models are supported.
- Automatically initiates the rigid body frictional contacts between the track chain and rolling elements (and if using a rigid soil model, contacts are also created between the track shoes and terrain).

The report extends the observation to the modeling of the military tracked vehicles (such as tanks) and it recommends ATV for these simulations, due to three main reasons:

- The track shoes are connected with compliant force elements. High speed operation causes large forces in the track chain tension, which in turn would cause non-negligible deflections in the bushing and pin elements that connect the track shoes.
- There is an option to use rigid or soft soil terrain models, which is desirable when considering non-paved surfaces.
- The template based design allows for easy substitution of entire subsystems, rather than individual bodies. If dealing with multiple instances of complex subsystems, this feature will greatly reduce the redundancy of recreating the subsystem.

1.2 ATV default tank model.

The simulations required for this thesis will be performed using the ATV toolkit of the Adams Car multi-body software. This software has many advantages, as anticipated in the previous section. What follows is a description of the ATV default tank model, which will be used through most the simulations. Certain situations will require modifications of the default model, but these will be detailed in their dedicated sections. Figure 1.4 shows the default tank model and its subsystems.

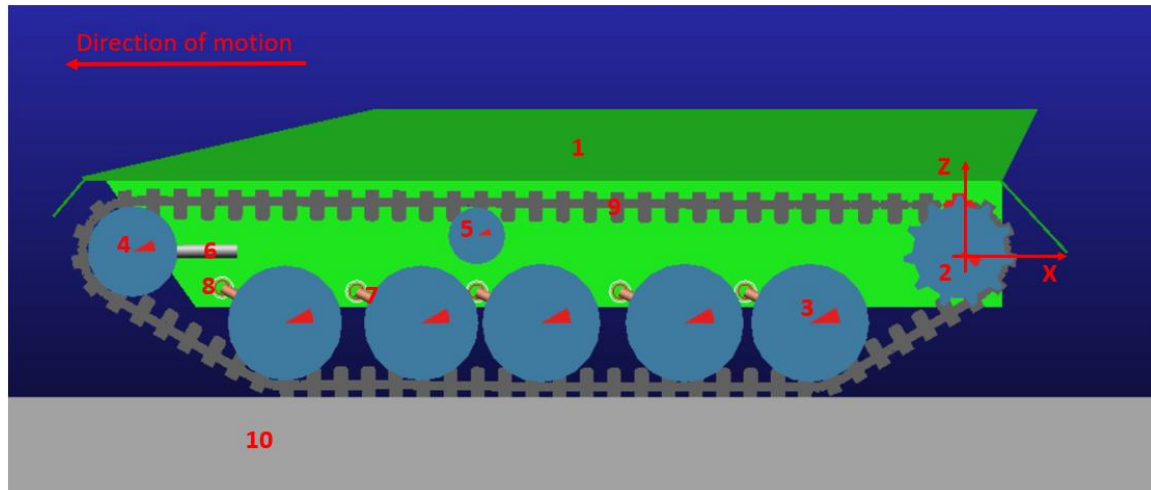


Figure 1.4. ATV default tank model.

The subsystems of the default tank model are:

1. Hull.
2. Sprocket wheel.
3. Road wheel.
4. Idler wheel.
5. Support roll.
6. Tensioner.
7. Road wheel connecting arm
8. Suspension system.
9. Track.
10. Ground.

Modifications will include the addition of a second support roll, tuning of the suspension parameters and the addition of a velocity controller subsystem, which imposes a PID controller that ensures the correct velocity during the maneuvers.

2 Track chain modeling

The modes of vibration of the upper part of the track chain show a very interesting behavior, because visually they resemble those of simple continuous elements, whose dynamics is well studied and understood. This serves as the motivation for the following analysis, which strives to model this section of the chain using analytical methods and validating these methods by comparing their results with results obtained from ATV simulations. If this can be achieved, it would be possible to provide standard models for simple analyses, where the user can plug in geometrical characteristics of the tank and obtain the natural frequencies of the track chain of interest.

Depending on the behavior under study, the entire upper chain can be modeled as a single element, or two individual elements, where the first one ranges from the sprocket wheel to the support wheel (segment 1), and the second from the support wheel to the tensioner wheel (segment 2), as shown in Figure 2.1.

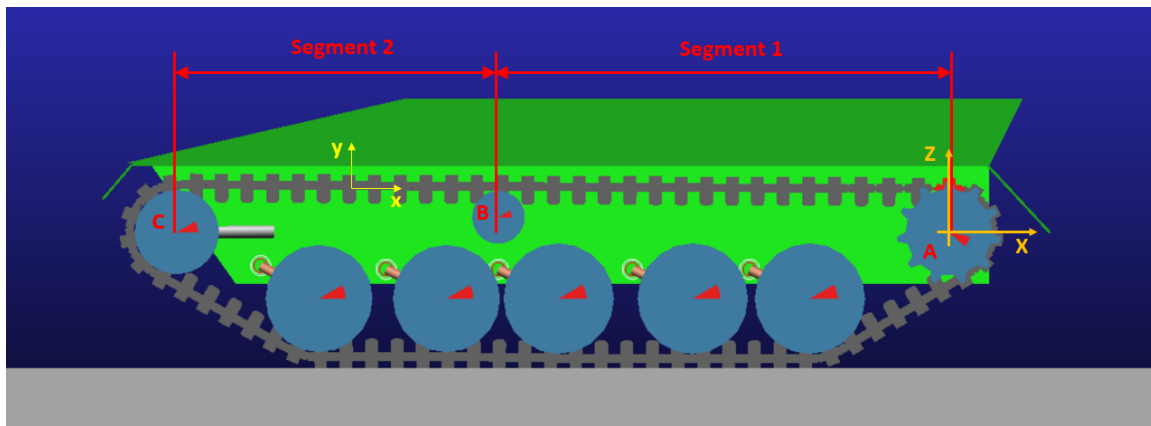


Figure 2.1. Default ATV tank model reference frame.

Figure 2.1 also shows how the global reference frame (X, Y, Z) and local reference frame (x, y, z) are defined. For users of ATV, this is an important distinction, because the same letters in the two references might define completely different orientations. The global reference is positioned in such a way that its origin lies in the intersection of the middle plane of the vehicle and the line that connects the centers of the two sprocket wheels. Furthermore, the global reference frame remains fixed. On the other hand, the local reference is centered in the part's center of mass and is fixed with respect to the part, so it might translate and rotate in relation to the global reference during the simulation.

2.1 Geometrical data of the model.

In order to perform the analyses, some parameters of the tank model need to be identified. In this case, they are obtained from the ATV default tank model, which features five road wheels and only one support wheel. These can vary depending on the type of tank, but such variations can be easily accounted for in the analytical models. ATV provides the location of each component with respect to its global coordinate system. In addition to that, the properties of each segment and the connection between them are also reported. These will all be useful in the following analyses.

Part	x_position [mm]	y_position [mm]	z_position [mm]	Mass [kg]	Radius [mm]	Width [mm]
Sprocket wheel	0	-1270	0	50	255	480
Support wheel	2690	-1270	89	30	158	300
Idle wheel	4610	-1270	1	50	250	355
Road wheel 1	3761	-1270	-396	35	320	355

Table 2.1. Geometrical data of the default tank model's components.

Starting from this table of data, the characteristics of segments 1 and 2 are evaluated. In particular, the mass of the segment and its linear mass density are calculated as follows:

$$m_{segment,i} = n_i \cdot m_{pad}$$

- $m_{segment,i}$ [kg]: mass of the i^{th} segment, as defined in Figure 1.
- n_i [–]: number of track pads that belong to the i^{th} segment.
- m_{pad} [kg]: mass of each single pad.

$$\mu = \frac{m_{tot}}{l_{tot}} = \frac{m_{segment,1} + m_{segment,2}}{l_{segment,1} + l_{segment,2}}$$

- μ $\left[\frac{kg}{m}\right]$: linear density of the chain, the same for each segment.
- m_{tot} [kg]: total mass of the upper track chain.
- l_{tot} [m]: total length of the upper track chain.

Segment	Nr. segments [-]	Segment mass [kg]	Length [mm]	Mass [kg]	μ [kg/m]
Segment 1	18	15	2690	270	100.87
Segment 2	13	15	1920	195	100.87

Table 2.2. Properties of segments 1 and 2.

Another important step lies in understanding how ATV models the connection between consecutive track pads, known as “tsl” (track segment link). Being a multibody software, the approach that ATV follows is that of considering the bodies as rigid and of a certain mass, and assigning the elastic and dissipative properties to the connection between these rigid bodies. The property file of each pad provides the pad’s dimensions, mass and inertia properties, stiffness and damping of the connection in the three directions of the local reference frame. These properties are important, because they characterize the behavior of the chain and will be fundamental in describing the latter in the following sections.

Relevant properties of the chain are reported below:

- Mass:
 - $m = 15 \text{ kg}$
- Inertia tensor:
 - $I_{xx} = 2.5E + 05 \text{ kg} \cdot \text{mm}^2$
 - $I_{yy} = 2.7E + 05 \text{ kg} \cdot \text{mm}^2$
 - $I_{zz} = 2.5E + 05 \text{ kg} \cdot \text{mm}^2$
- Translational stiffness of the connection:
 - $k_x = 5.2E + 05 \text{ N/mm}$
 - $k_y = 5.2E + 05 \text{ N/mm}$
 - $k_z = 5.2E + 05 \text{ N/mm}$
- Translational damping of the connection:
 - $c_x = 50 \frac{\text{N}\cdot\text{s}}{\text{mm}}$
 - $c_y = 50 \frac{\text{N}\cdot\text{s}}{\text{mm}}$
 - $c_z = 50 \frac{\text{N}\cdot\text{s}}{\text{mm}}$
- Rotational stiffness of the connection:
 - $k_{r,x} = 3.0E + 06 \frac{\text{N}\cdot\text{mm}}{\circ}$
 - $k_{r,y} = 3.0E + 06 \frac{\text{N}\cdot\text{mm}}{\circ}$
 - $k_{r,z} = 30 \frac{\text{N}\cdot\text{mm}}{\circ}$
- Rotational damping of the connection:
 - $c_{r,x} = 200 \frac{\text{N}\cdot\text{mm}\cdot\text{s}}{\circ}$
 - $c_{r,y} = 200 \frac{\text{N}\cdot\text{mm}\cdot\text{s}}{\circ}$
 - $c_{r,z} = 200 \frac{\text{N}\cdot\text{mm}\cdot\text{s}}{\circ}$

An interesting remark is that judging from the stiffness of the connection, and seeing how in two directions it is very large, while on the third it is 4 orders of magnitude lower, the connection can be considered as a revolute joint. This will play an important role in the modeling assumptions and when assigning the BC.

Having defined these characteristics for each segment, the next step is the analysis and characterization of the behavior of the chain.

2.2 ATV simulation results.

The tank model is a highly non-linear system. To perform the modal analysis, ATV linearizes the system at the time instant that the user requires and performs a complex modal analysis related to that instantaneous state of the system. In this way, even during a simulation, modal analyses performed at different time instants will likely give different results, if the system is not in static or steady-state conditions (more details on how the simulation is setup are given in Appendix A).

For the purposes of this thesis, the duration of the simulations is 20 seconds, so as to allow enough time for the vehicle to settle and achieve steady state. The modal analysis of the linearized system is performed at the end of the 20 seconds. To reduce the time of simulations, the half-tank model is considered. This model studies only the left half of the tank, taking into account the tank's symmetry along its middle longitudinal plane. The results do not differ from the full tank model, but the simulation is significantly decreased. The parameter that is tuned throughout the simulations is the tension imposed by the idle wheel. The values of tension used are the following:

- 15000 N
- 30000 N
- 45000 N
- 60000 N

The results of these modal analyses are shown in the ATV post-processing window, under the menu "Load mode shape animation", found in the "View" tab. The results are shown graphically by animating the modes as in Figure 2.2. For each mode, the graphical user interface (GUI) show the mode number (according to the ordering that ATV assigns to the modes), the natural frequency and the damping ratio. A "Table of Eigenvalues" contains all the modes of the system (around 500 for this half-tank model), where the modes are ordered according to their eigenvalue's imaginary part. This table shows the natural frequency, damping ratio and eigenvalue for each of the modes. In ATV tutorials, it is suggested to refer to modes that have a non-zero imaginary part of the eigenvalue.

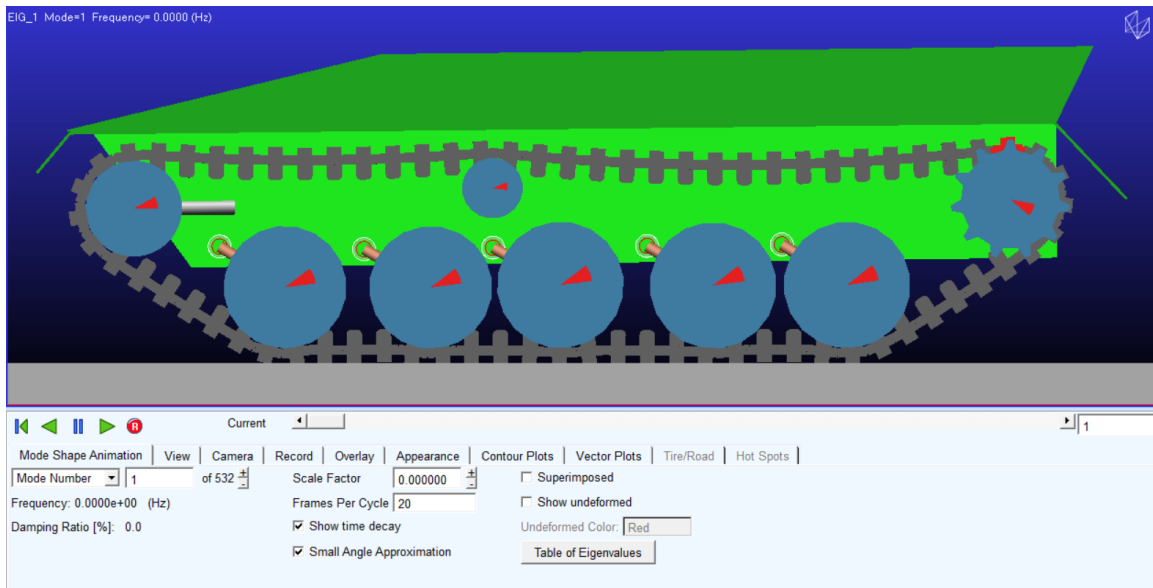


Figure 2.3. ATV interface for mode shape animation.

The following figure shows the table of eigenvalues as given in the ATV post-processing window.

EIGEN VALUES (Time = 20.0)				
FREQUENCY UNITS: (Hz)				
MODE NUMBER	UNDAMPED NATURAL FREQUENCY	DAMPING RATIO	REAL	IMAGINARY
1	0.000000E+00	0.000000E+00	0.000000E+00	0.000000E+00
2	8.294461E-09	1.000000E+00	-8.294461E-09	0.000000E+00
3	1.057140E-08	1.000000E+00	-1.057140E-08	0.000000E+00
4	1.284824E-08	1.000000E+00	-1.284824E-08	0.000000E+00
5	1.609783E-08	1.000000E+00	1.609783E-08	0.000000E+00
6	8.088345E-08	1.000000E+00	-8.088345E-08	0.000000E+00
7	3.167170E-07	1.000000E+00	3.167170E-07	0.000000E+00
8	1.341359E-03	1.000000E+00	1.341359E-03	0.000000E+00
9	2.252346E-03	1.000000E+00	-2.252346E-03	0.000000E+00
10	1.207393E-02	1.000000E+00	-1.207393E-02	0.000000E+00

Figure 2.2. Table of eigenvalues.

Looking at the results obtained from the ATV simulation, it is obvious that the upper part of the chain (both segments 1 and 2) displays three types of modes. These can be grouped in the following categories:

- Bending modes in the longitudinal plane ((X-Z) plane), which will be denoted as vertical bending.
- Bending modes in the lateral plane ((X-Y) plane), which will be denoted as lateral bending.
- Torsional modes around the X-axis, which will be denoted as torsion.

The figures that follow illustrate these modes. For simplicity, the mode shapes shown here will be the results of a single simulation. Changing the simulation parameters, the results change, but visually the modes remain identical. Furthermore, the first three modes for each of the aforementioned behaviors will be depicted, but for the analysis as many as twenty will be considered, in order to get a thorough comparison between the simulation and the analytical formulation.

The following mode shapes depict the vertical bending ((X-Z) plane). This behavior is characterized by the two segments 1 and 2 bending independently of each other and separated by the support roll. This leads to the conclusion that the support roll constitutes a rigid constraint in the vertical direction. Each of the segments, while bent, takes a form similar to a sinusoidal. The number of the modes is based on the relationship between the wavelength and the segment length. More specifically, it is such that:

$$\lambda_{r,i} = \frac{2L_i}{r}$$

- L_i : length of segment “i”.
- r : mode number.
- $\lambda_{r,i}$: wavelength of mode “r” of segment “i”.

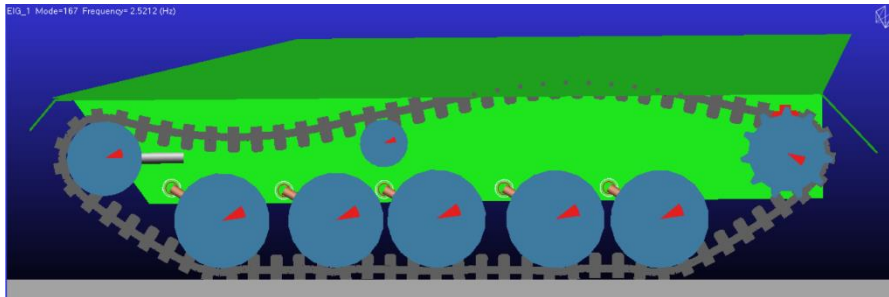


Figure 2.4. Segment 1 vertical bending first mode shape (2.53 Hz).

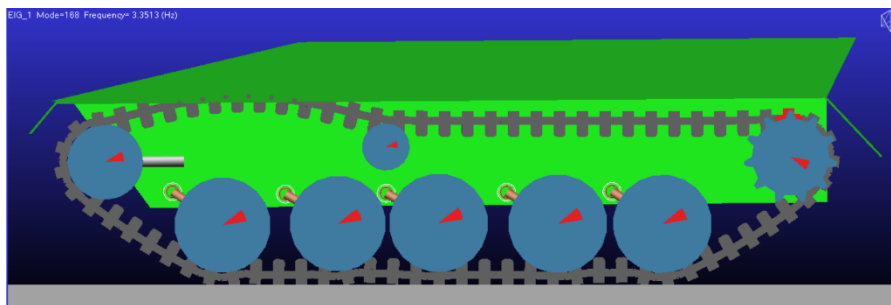


Figure 2.5. Segment 2 vertical bending first mode shape (3.37 Hz).

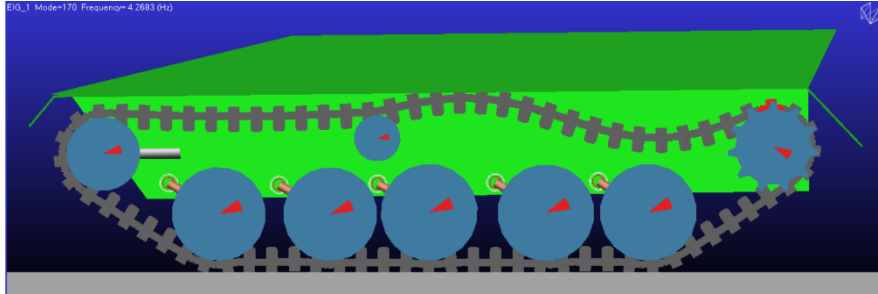


Figure 2.6. Segment 1 vertical bending second mode shape (4.27 Hz).

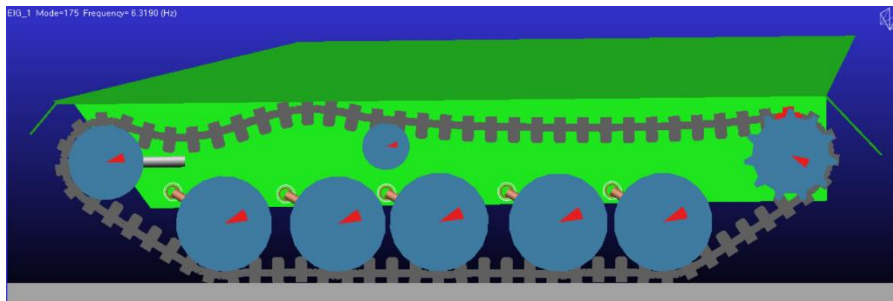


Figure 2.7. Segment 2 vertical bending second mode shape (6.32 Hz).

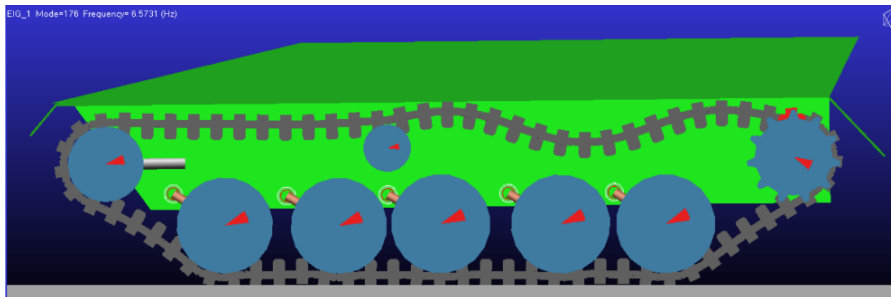


Figure 2.8. Segment 1 vertical bending third mode shape (6.58 Hz).

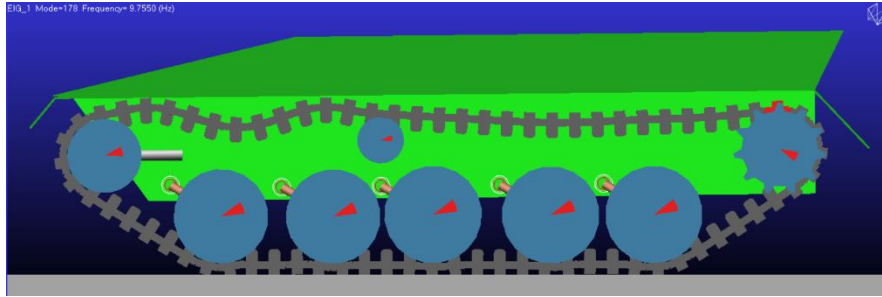


Figure 2.9. Segment 2 vertical bending third mode shape (9.76 Hz).

The lateral bending modes have been named in a manner similar to vertical bending modes. The difference in this case, based on what can be seen from the simulation results, the support roll does not define two independent segments, but the wave propagates through the entire length of the upper chain. The support roll instead, acts as a soft constraint of a certain stiffness, but not rigid as in the previous case. Notice also how for the chain lateral bending ((X-Y plane)), the modes shown start from the second. This is because the simulation does not show a mode shape that would correspond to the first.

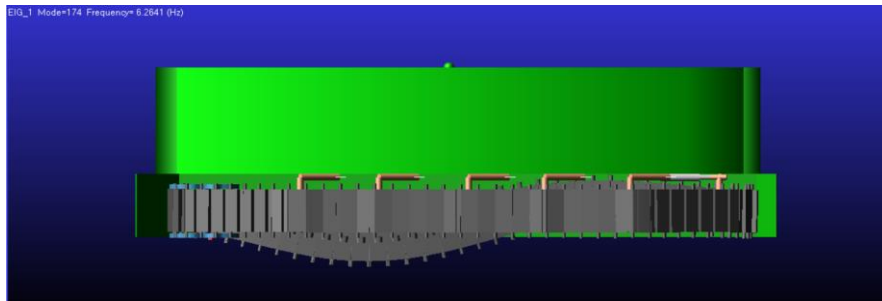


Figure 2.10. Chain lateral bending second mode shape (6.31 Hz).

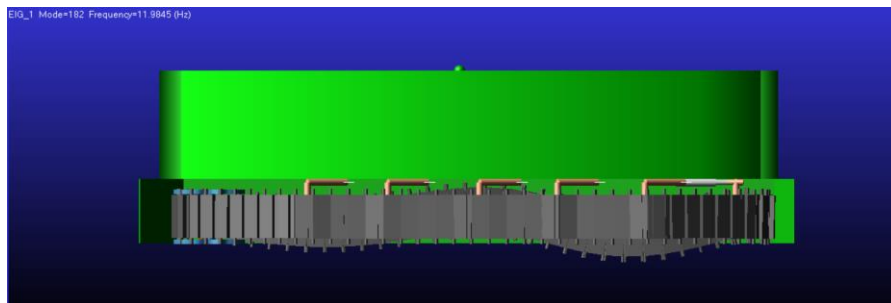


Figure 2.11. Chain lateral bending third mode shape (12.22 Hz).

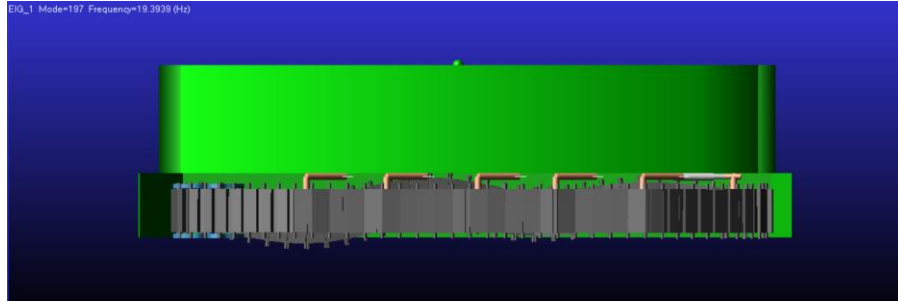


Figure 2.12. Chain lateral bending fourth mode shape (19.6 Hz).

Torsion modes can be identified as they resemble the rotation of the chain around its own longitudinal axis and that spans the entire length of the upper chain. Different modes are numbered considering the number of track pads that do not rotate, therefore separating the chain in segments that rotate in opposite directions. More specifically, the first mode shape is characterized by two pads that do not rotate, namely the first and last pads. The second mode is characterized by three pads that do not rotate; the first pad, the last pad and a stationary pad around the middle of the chain. And so on.

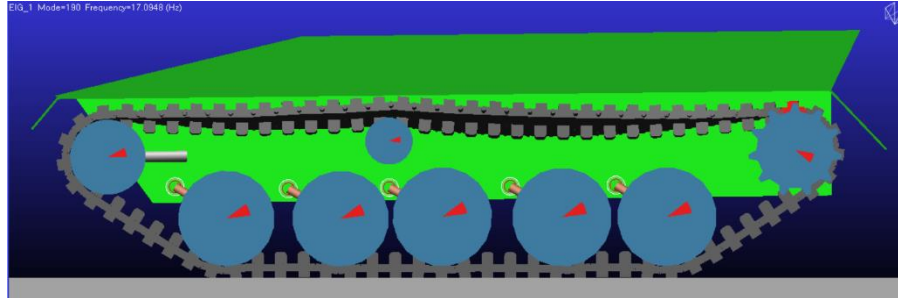


Figure 2.13. Chain torsion first mode shape (17.13 Hz).

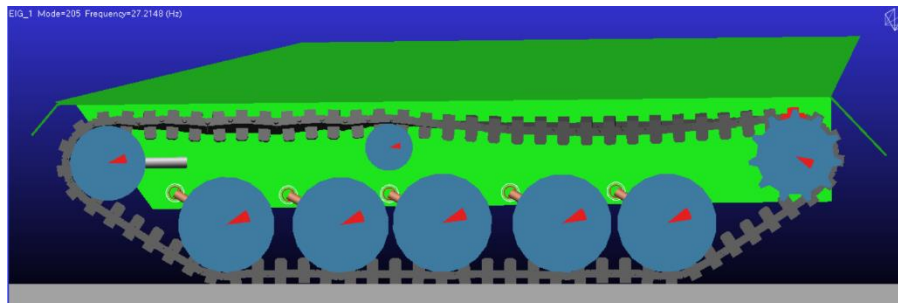


Figure 2.14. Chain torsion second mode shapes (27.22 Hz).

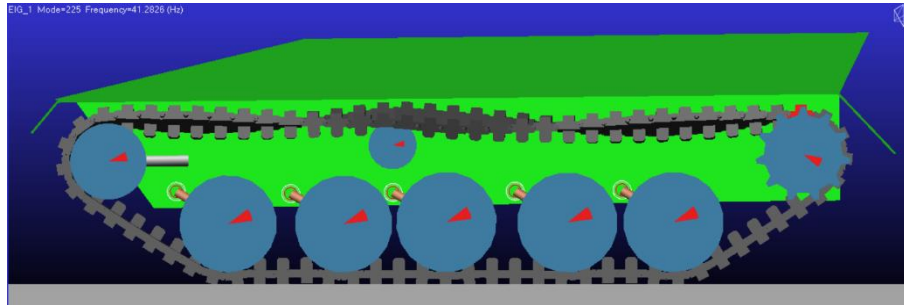


Figure 2.15. Chain torsion third mode shape (41.33 Hz).

The results of the simulations performed with different tensioner force values and for the three behaviors of the chain are reported in the tables that follow. For the longitudinal bending modes, the support roll defines a rigid constraint, which coupled with the low torsional stiffness of the chain in the Y-direction, allows treating segments 1 and 2 as separate.

String	Tension idler [N]	f1 [Hz]	f2 [Hz]	f3 [Hz]	f4 [Hz]	f5 [Hz]
Segment 1	15000	2.53	4.27	6.58	8.74	11.1
	30000	2.91	5.53	8.39	11.37	14.53
	45000	3.25	6.2	9.38	12.6	16
	60000	3.63	7.07	10.7	14.4	18.27
Segment 2	15000	3.37	6.32	9.76	13.53	17.51
	30000	4.21	8.16	12.6	17.59	22.89
	45000	4.6	8.98	13.8	18.84	24.37
	60000	5.12	10.13	15.5	21.07	27.08

Table 2.3. Simulation results for chain vertical bending.

Tension	f2 [Hz]	f3 [Hz]	f4 [Hz]	f5 [Hz]	f6 [Hz]	f7 [Hz]	f8 [Hz]
15000	6.31	12.22	19.6	33.3	40.6	57.2	69.84
30000	6.71	12.57	20.22	33.55	40.92	58	69.5
45000	6.94	12.79	20.49	33.82	41.03	58.17	69.64
60000	7.22	13.08	20.8	34.18	41.14	58.41	69.98

Table 2.4. Simulation results for chain lateral bending.

Tension	f1 [Hz]	f2 [Hz]	f3 [Hz]	f4 [Hz]	f5 [Hz]	f6 [Hz]
15000	17.13	27.22	41.33	54	67	80
30000	16.75	27.3	41.42	54.35	67.4	80.57
45000	16.73	27.31	41.45	54.4	67.45	80.74
60000	16.7	27.32	41.45	54.43	67.44	80.82

Table 2.5. Simulation results for chain torsion.

The following graphs will show how the frequency of the same harmonic changes for the different tensioner force values, for each of the track chain behaviors.

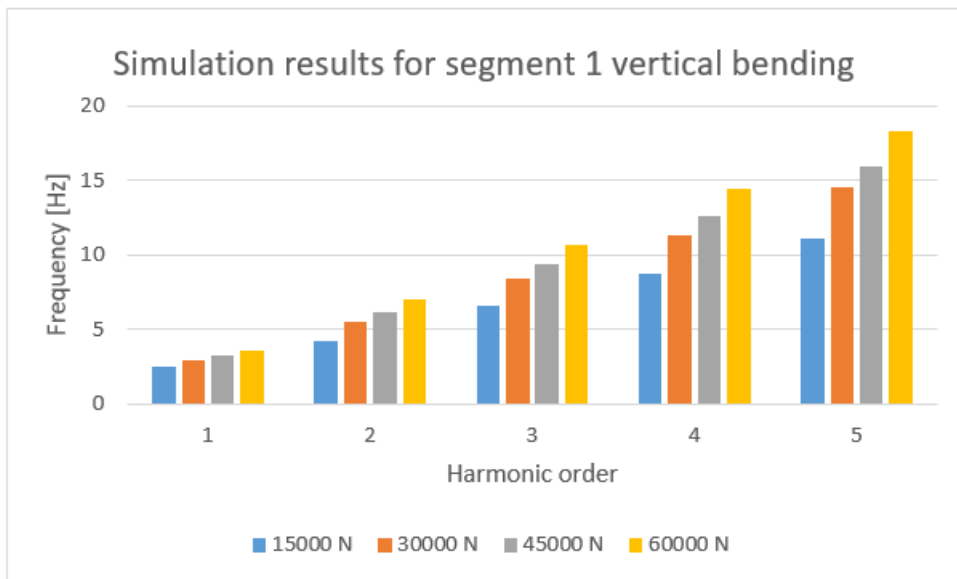


Figure 2.16. Simulation results for segment 1 vertical bending.

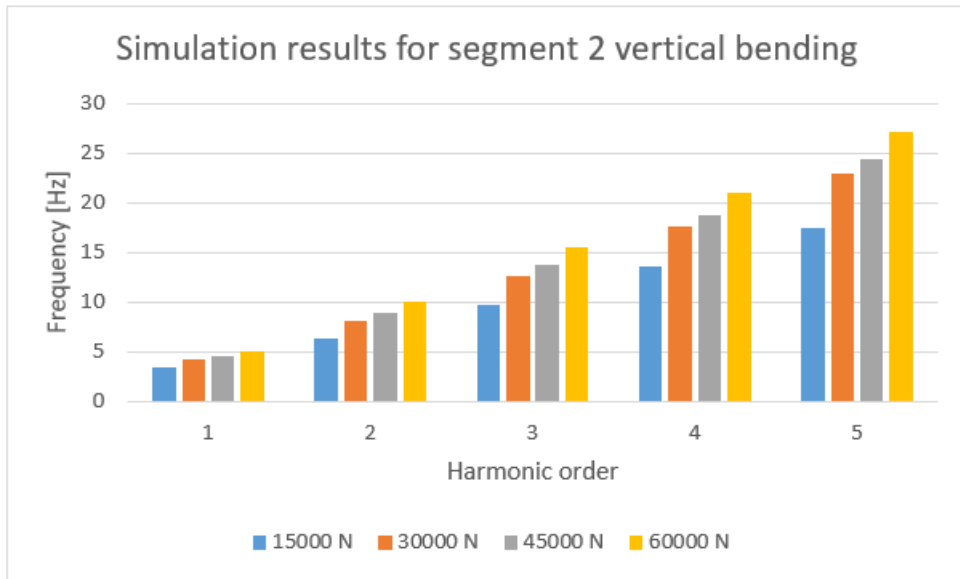


Figure 2.17. Simulation results for chain torsion vertical bending.

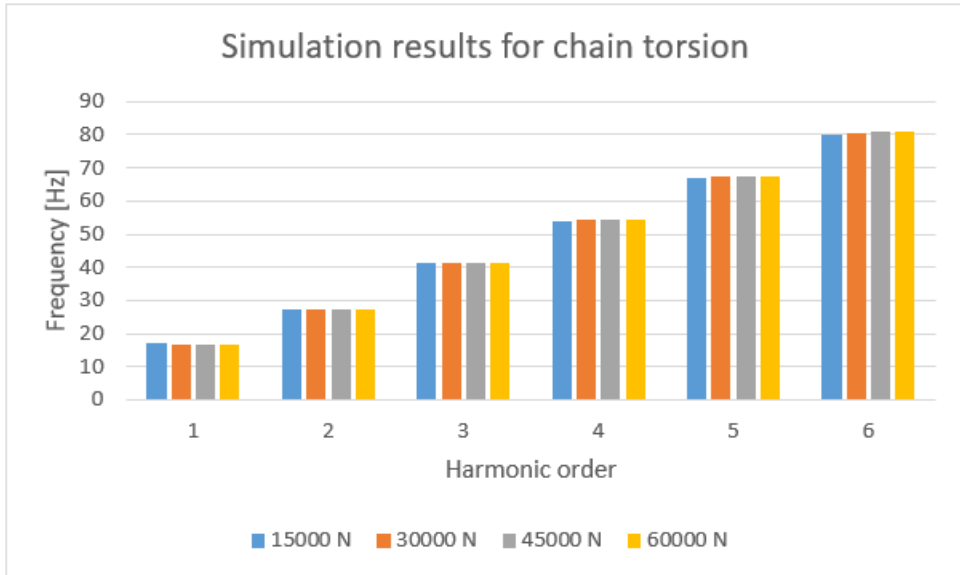


Figure 2.18. Simulation results for chain torsion.

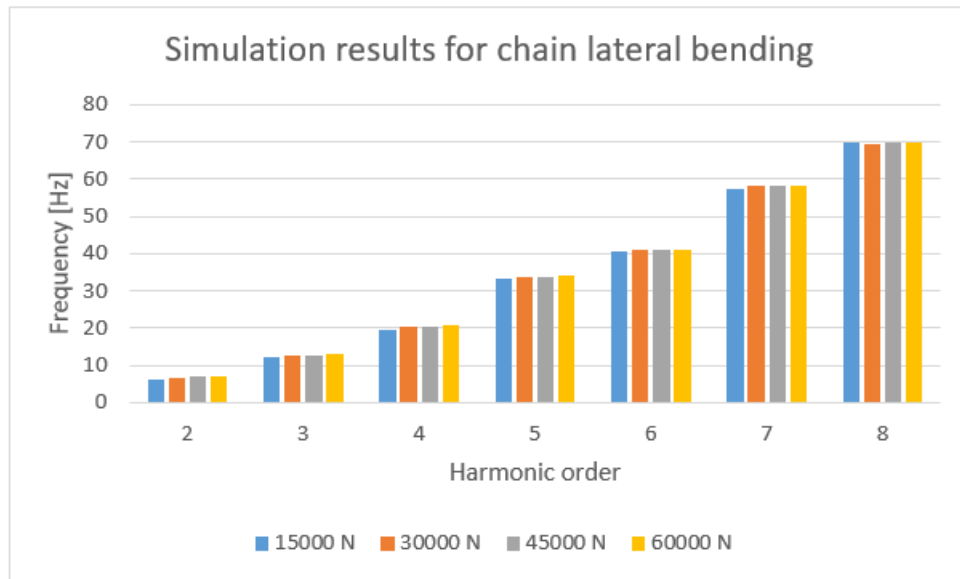


Figure 2.19. Simulation results for chain lateral bending.

Some remarks can be made regarding the results of the simulation:

- The support roll constitutes a rigid constraint in the longitudinal (X-Z) plane, separating the chain in two segments that can be studied individually, but in the lateral (X-Y) plane it has a small stiffness, so the chain can be studied as a whole.
- The vertical bending behavior is heavily dependent on the tensioner force, while the torsion and lateral bending show only a small increase in frequency for the same harmonic, as the tensioner force increases.

These remarks will influence the way that the analytical models to describe the chain are set up.

2.3 Modeling the track chain vertical bending behavior.

This first analysis aims at modeling the vertical bending ((X-Z) plane) of the chain. The methods proposed here consider the chain as:

1. Two continuous strings in tension, separated by the support roll, and where the tension on the chain is calculated analytically.
2. Two continuous strings in tension, separated by the support roll, and where the tension on the chain is obtained from the ATV post-processing window.
3. Discretized system where each track pad is a rigid body connected to the others by means of elastic elements (consistent with the multi-body approach).

2.3.1 Continuous string in tension with analytically evaluated tension.

The string-like behavior of the chain in the vertical direction is due to the very small (almost negligible) torsional stiffness of the connection between track pads in the Y-direction. The assumptions that are made when studying the chain as a string are the following:

- The chain is considered as a continuous system (rather than a discrete system made of track segments linked together by revolute joints).
- Tension is uniform on each of the strings.
- Constant linear density of the chain.
- Each of the strings can be considered as fixed on both ends.

Considering these hypotheses, the wave equation of the chain (string) will be solved, imposing the correct boundary conditions, in order to obtain the expressions of the natural frequencies. The natural frequencies will be computed and they will be compared to the frequencies that ATV shows for mode shapes that should correspond to the theoretical ones.

The tension of the upper part of the chain is not the one that the idle wheel provides. The force that the tensioner imposes in the chain is shared between the upper and lower parts of the chain. Isolating that part of the chain assembly, we can perform a force balance in order to obtain the expression of the tension for the part of chain we are interested in. Obviously, some assumptions are required to simplify the model:

- Null friction in the idler hub.
- Uniform tension in the string.
- Weightless string.

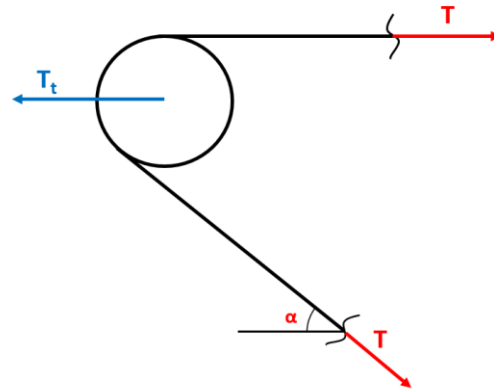


Figure 2.20. Force equilibrium around the idle wheel.

Performing the horizontal equilibrium, the tension T on the upper chain is given by the following expression:

$$T = \frac{T_t}{1 + \cos \alpha}$$

The value of the angle α is calculated by using some geometrical relations between the tensioner and the first road wheel. Knowing it, we can evaluate the tension on the upper chain.

The table below shows the tension in the string, as a function of the idle wheel tension. Note how the tension is the same in both string 1 and 2, for the same value of idle wheel tension. In the following section, this will be shown to be wrong.

String	Tension idler [N]	Tension string [N]
String 1	15000	7939.91
	30000	15879.81
	45000	23819.72
	60000	31759.62
String 2	15000	7939.91
	30000	15879.81
	45000	23819.72
	60000	31759.62

Table 2.6. Tension on strings 1 and 2, as a function of the idle wheel tension.

The wave equation for a continuous string in tension is as follows:

$$\frac{\partial^2 y}{\partial t^2} = \frac{T}{\mu} \frac{\partial^2 y}{\partial x^2}$$

Imposing the boundary conditions for a fixed-fixed string, allows obtaining the expression of the natural frequency:

$$f_i = \frac{i}{2L} \sqrt{\frac{T}{\mu}}$$

- f [Hz]: frequency of the i -th order harmonic.
- L [m]: length of the string of interest.
- T [N]: tension on the string.
- μ [kg/m]: linear density of the string.

Calculating the results with the formula above, we obtain the following frequencies:

String	Tension idler [N]	Tension string [N]	f1 [Hz]	f2 [Hz]	f3 [Hz]	f4 [Hz]	f5 [Hz]
String 1	15000	7939.91	1.65	3.30	4.95	6.60	8.25
	30000	15879.81	2.33	4.66	7.00	9.33	11.66
	45000	23819.72	2.86	5.71	8.57	11.43	14.28
	60000	31759.62	3.30	6.60	9.89	13.19	16.49
String 2	15000	7939.91	2.31	4.62	6.93	9.24	11.55
	30000	15879.81	3.27	6.53	9.80	13.07	16.34
	45000	23819.72	4.00	8.00	12.01	16.01	20.01
	60000	31759.62	4.62	9.24	13.86	18.48	23.10

Table 2.7. The first five analytical frequencies for strings 1 and 2.

2.3.2 Continuous string in tension with ATV provided tension.

ATV allows creating “track segment requests”, which basically provide information in the post-processing window, such as force, displacement and so on, for each track pad after the simulation is completed. The tension on segments 1 and 2 can be obtained by looking at the longitudinal force exchanged between consecutive pads contained in the segment (segments 1 or 2). It is interesting to notice that the longitudinal force between consecutive segments is the same, on each of the strings. This means that on each string, the tension is constant, which is in line with the theory of continuous systems. Table 2.8 summarizes the results for this analysis.

String	Tension idler [N]	Tension string [N]	f1 [Hz]	f2 [Hz]	f3 [Hz]	f4 [Hz]	f5 [Hz]
String 1	15000	11850	2.02	4.04	6.06	8.08	10.10
	30000	19368	2.58	5.16	7.75	10.33	12.91
	45000	25370	2.96	5.91	8.87	11.82	14.78
	60000	33242	3.38	6.77	10.15	13.53	16.91
String 2	15000	11730	2.80	5.60	8.40	11.19	13.99
	30000	19301	3.59	7.18	10.77	14.36	17.95
	45000	25320	4.11	8.22	12.34	16.45	20.56
	60000	33191	4.71	9.42	14.12	18.83	23.54

Table 2.8. The first five natural frequencies for strings 1 and 2, with ATV tension values.

As can be seen, the tension that ATV provides is quite different from the one that was analytically evaluated in the previous section. For this reason, the frequencies evaluated with the calculated tension are expected to be quite different from the ones that the simulation gives.

2.3.3 Longitudinal bending discrete model.

Adams Car, and consequently ATV, use a multi-body approach. This means that the system is considered as composed of rigid elements, that are connected by elastic links, and that have their own inertia, stiffness and damping properties. For this reason, it is interesting to study the upper chain as a multi-DOF system, where the bodies are connected to each other by linear and torsional springs (damping is neglected), in line with the way ATV models the connection. A scheme of how this approach works is shown in Figure 2.21.

The properties of the elements in the scheme above are all provided by ATV and are listed below:

- Mass of the pad: $m = 15 \text{ kg}$.
- Mass moment of inertia of the pad: $I = 2.5 * 10^5 \text{ kgmm}^2$
- Translational stiffness of the connection: $k_{trans} = 5.2 * 10^5 \frac{N}{mm}$
- Rotational stiffness of the connection: $k_{tor} = 30 \frac{Nmm}{\circ}$
- Length of the pad: $l = 152.4 \text{ mm}$
- Tension on the chain: depends on the value imposed for the simulation.

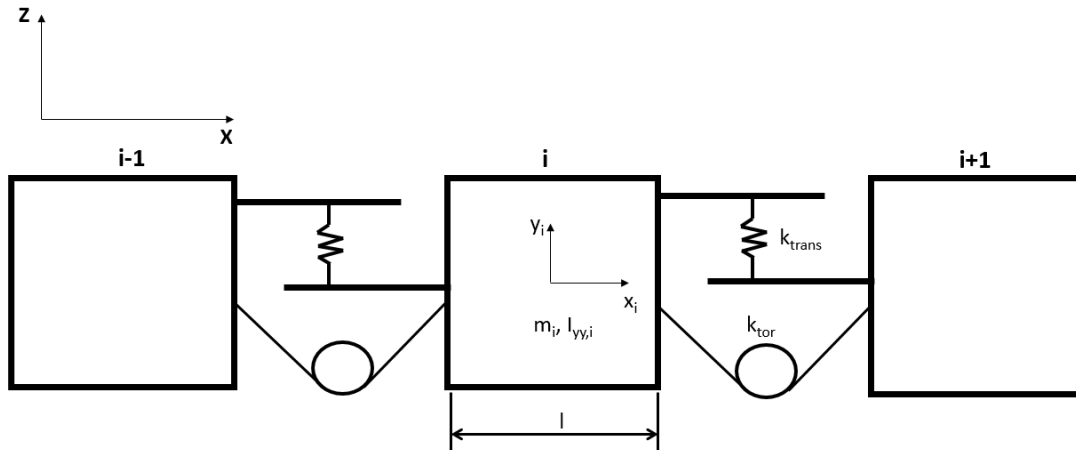


Figure 2.21. Schematic representation of the discrete MDOF chain model.

The two segments will be considered separated by the support roll, which would allow to study them independently. Segment 1 consists of 18 track pads, while segment 2 consists of 13 track pads. Each pad is considered to have two DOFs, namely vertical translation in the Z-direction and clockwise rotation around its center of mass. For this reason, segment 1 has 36 DOFs and segment 2 has 26 DOFs. By imposing pinned-pinned boundary conditions, the translation of the first and last pad of each segment is not allowed, so the total number of DOFs decreases by two for each segment, bringing the total to 34 for segment 1 and 24 for segment 2. The boundary conditions constrain the system as shown in Figure 2.22. The free body diagram of the generic pad “i”, the first and last pads for each of the segments are shown in Figure 2.23.

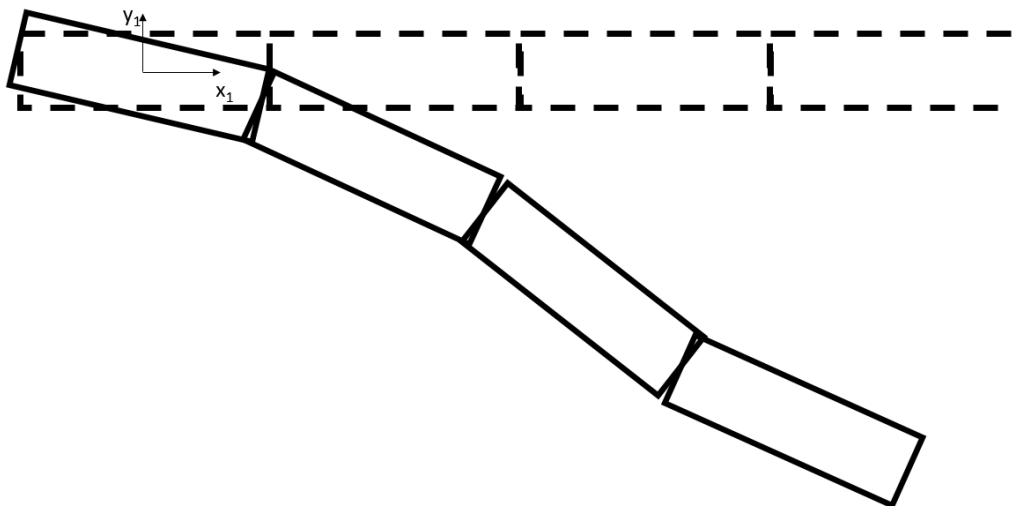


Figure 2.22. Boundary conditions on the chain extremes.

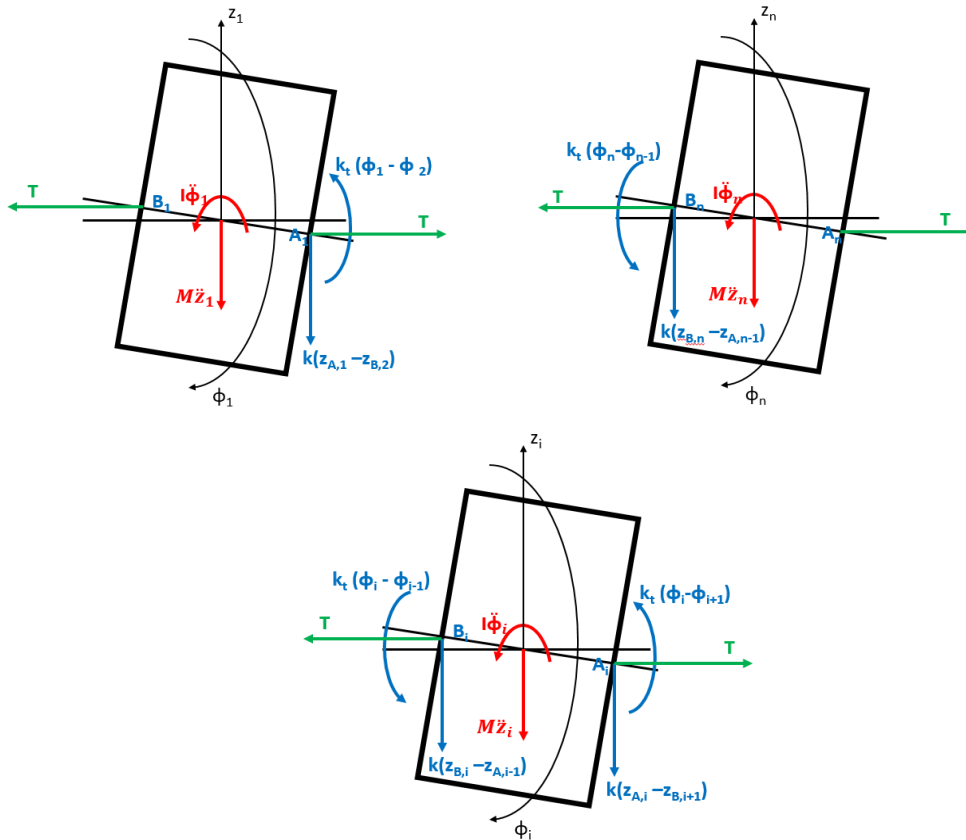


Figure 2.23. FBD of the first, last and generic pad.

Two equations of motion are written for each pad. One equation is about the vertical translation and the other about the rotation around the pad's center of mass.

The generalized displacement coordinate is: $\{q\} = \begin{Bmatrix} \{y_{i-1}\} \\ \{\theta_{i-1}\} \\ \{y_i\} \\ \{\theta_i\} \\ \{y_{i+1}\} \\ \{\theta_{i+1}\} \end{Bmatrix}$

EOM 1:

$$\begin{aligned} \uparrow) M\ddot{z}_1 + kz_1 - k\frac{l}{2}\theta_1 - kz_2 - k\frac{l}{2}\phi_2 &= 0 \\ \cup) I\ddot{\phi}_1 - k\frac{l}{2}z_1 + (k_t + \frac{kl^2}{4} + Tl)\phi_1 + k\frac{l}{2}z_2 - (k_t + \frac{kl^2}{4})\phi_2 &= 0 \end{aligned}$$

EOM 31:

$$\uparrow) M\ddot{z}_{31} + kz_{31} + k\frac{l}{2}\phi_{31} - kz_{30} + k\frac{l}{2}\phi_{30} = 0$$

$$\cup) I\ddot{\phi}_{31} - k\frac{l}{2}z_{30} - (k_t + \frac{kl^2}{4})\phi_{30} + k\frac{l}{2}z_{31} + (k_t + \frac{kl^2}{4} + Tl)\phi_{31} = 0$$

EOM i:

$$\uparrow) M\ddot{z}_i - kz_{i-1} + 2kz_i - kz_{i+1} + k\frac{l}{2}\phi_{i-1} - k\frac{l}{2}\phi_{i+1} = 0$$

$$\cup) I\ddot{\phi}_i - k\frac{l}{2}z_{i-1} - (k_t + \frac{kl^2}{4})\phi_{i-1} + (2k_t + \frac{kl^2}{2} + Tl)\phi_i + k\frac{l}{2}z_{i+1} - (k_t + \frac{kl^2}{4})\phi_{i+1} = 0$$

The terms on these equations are arranged on the mass and stiffness matrices as follows:

$$[M] = \begin{bmatrix} \begin{bmatrix} M_{i-1} & 0 \\ 0 & I_{i-1} \end{bmatrix} & 0 & 0 \\ 0 & \begin{bmatrix} M_i & 0 \\ 0 & I_i \end{bmatrix} & 0 \\ 0 & 0 & \begin{bmatrix} M_{i+1} & 0 \\ 0 & I_{i+1} \end{bmatrix} \end{bmatrix}$$

The stiffness matrix is more complicated and for ease of presentation it will be built in blocks.

$$[K_i] = \begin{bmatrix} 2k & 0 \\ 0 & 2k_t + \frac{kl^2}{2} + Tl \end{bmatrix}$$

$$[K_{i-1}] = \begin{bmatrix} -k & \frac{kl}{2} \\ -\frac{kl}{2} & -k_t + \frac{kl^2}{4} \end{bmatrix}$$

$$[K_{i+1}] = \begin{bmatrix} -k & -\frac{kl}{2} \\ \frac{kl}{2} & -k_t + \frac{kl^2}{4} \end{bmatrix}$$

$$[K_1] = \begin{bmatrix} k & 0 \\ 0 & k_t + \frac{kl^2}{4} + Tl \end{bmatrix}$$

$$[K_n] = \begin{bmatrix} k & 0 \\ 0 & k_t + \frac{kl^2}{4} + Tl \end{bmatrix}$$

$$[K] = \begin{bmatrix} [K_1] & [K_{i+1}] & 0 & 0 & 0 \\ 0 & \ddots & 0 & 0 & 0 \\ 0 & [K_{i-1}] & [K_i] & [K_{i+1}] & 0 \\ 0 & 0 & 0 & \ddots & 0 \\ 0 & 0 & 0 & [K_{i-1}] & [K_n] \end{bmatrix}$$

The mass and stiffness matrices are implemented in MATLAB and the eigenvalue problem is solved, giving the eigenvalues and natural frequencies. The following tables will summarize the results obtained with the continuous string model with calculated tension, continuous string with ATV provided tension, discrete model and simulation for each of the chain segments. The following denomination will be used for each scenario, to keep the notation more compact:

- Continuous 1: continuous string model with calculated tension results.
- Continuous 2: continuous string model with ATV provided tension results.
- Discrete: discrete model results.
- Simulation: simulation results.

Segment 1				
Harmonic	Continuous 1	Continuous 2	Discrete	Simulation
1	1.65	2.02	2.19	2.53
2	3.30	4.04	4.39	4.27
3	4.95	6.06	6.64	6.58
4	6.60	8.08	8.96	8.75
5	8.25	10.1	11.37	11.11
6	9.89	12.12	13.89	13.57
7	11.54	14.14	16.55	16.19
8	13.19	16.16	19.36	18.89
9	14.84	18.18	22.33	21.8
10	16.49	20.2	25.47	24.89
11	18.14	22.22	28.73	28
12	19.79	24.24	32.05	31.47
13	21.44	26.26	35.30	34.79
14	23.09	28.28	38.26	37.82
15	24.74	30.3	40.69	40.53
16	26.39	32.32	42.29	42.27

Table 2.9. Results summary for segment 1.

Segment 2				
Harmonic	Continuous 1	Continuous 2	Discrete	Simulation
1	2.31	2.8	3.14	3.37
2	4.62	5.6	6.35	6.32
3	6.93	8.4	9.68	9.76
4	9.24	11.2	13.21	13.53
5	11.55	14	16.99	17.5
6	13.86	16.8	21.08	22.07
7	16.17	19.6	25.49	26.88
8	18.48	22.4	30.13	32.16
9	20.79	25.2	34.75	37.3
10	23.1	28	38.86	41.17

Table 2.10. Results summary for segment 2.

The following figures plot the results of the last two tables, so it is clearer which of the methods proposed so far gives the closest approximation.

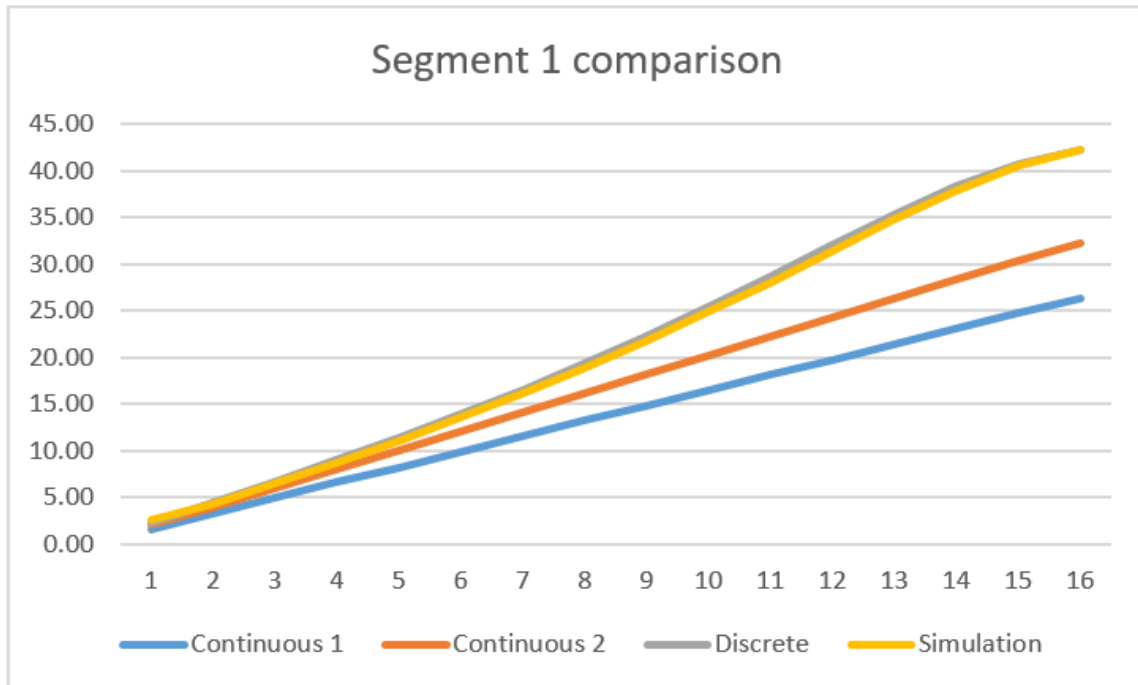


Figure 2.24. Comparison between the modeling methods and simulation results for segment 1.

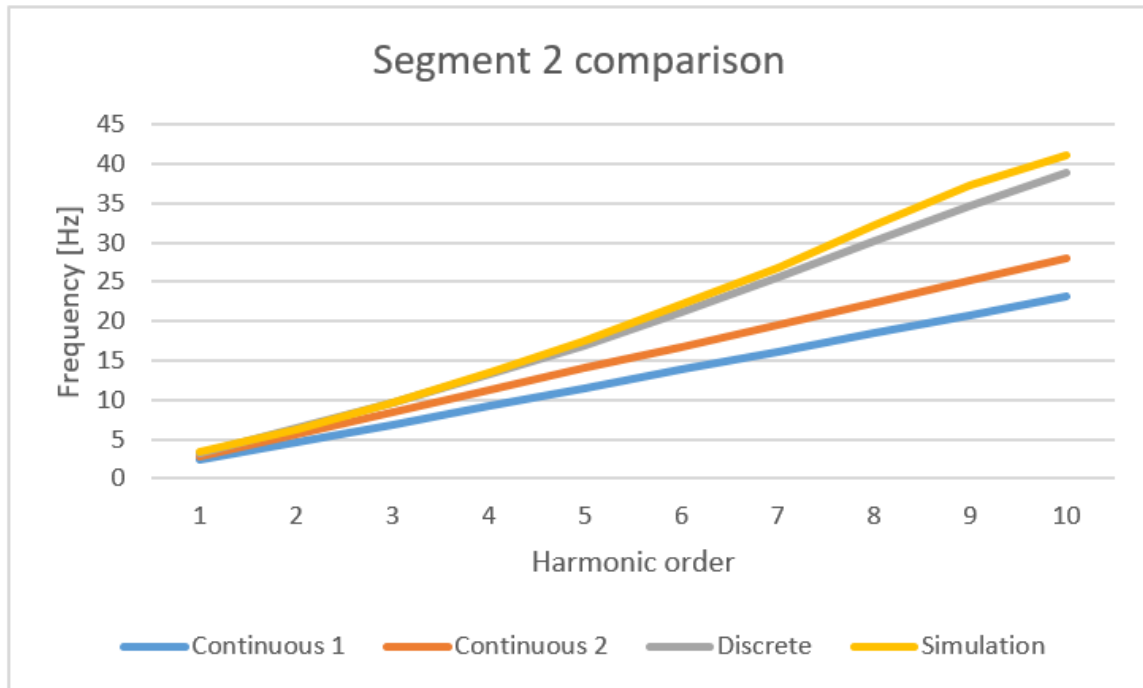


Figure 2.25. . Comparison between the modeling methods and simulation results for segment 2.

The tables, and the plots even clearer, show that the method which provides the best approximation is the discrete model. This is to be expected, since the discrete model follows very closely the multi-body approach (with minor differences). However, also the other models should not be discarded, because especially at the lower harmonics, they offer a decent approximation that might be acceptable when only a preliminary design is required.

An alternative method of implementing the discrete model is by considering the chain as a whole, and introducing a very large stiffness where the support roll is located. This method was not shown here, because considering two segments yields more approximate results. However, this method is interesting because plotting the eigenvectors obtained from it, can be noticed that they resemble the mode shape that corresponds to that eigenvector. This is illustrated in Figure 2.26.

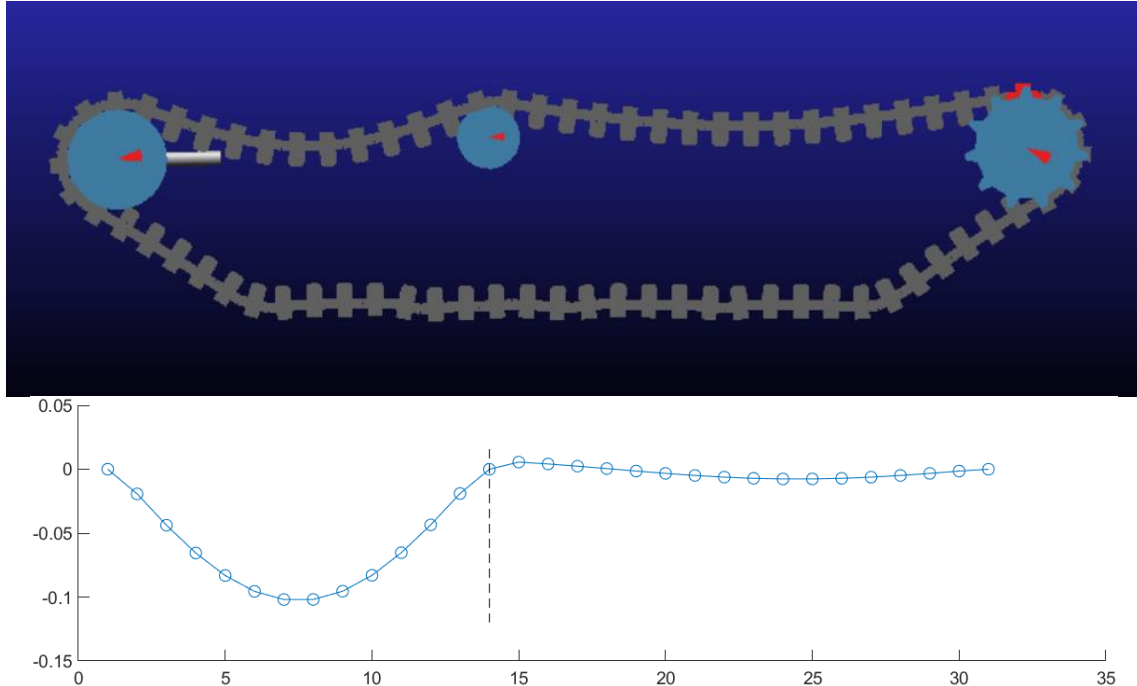


Figure 2.26. Similarity between a mode shape and its corresponding eigenvector.

2.4 Modeling the track chain torsional behavior.

The procedure for studying the torsional behavior will be detailed below. In particular, it is important to highlight the assumptions made:

- The chain can be considered as a shaft in torsion, which is clamped on both sides (boundary conditions).
- An analogy will be made between a lumped system, such as the chain under study, and a continuous system, by expressing the wave speed as a function of parameters that are present in the lumped model.
- Small vibration angles that allow to simplify the procedure from a computational point of view and linearize the system.
- Differently to what was done for the string model, where the upper part of the track chain was studied as two independent segments, for the torsion model the entire upper chain will be studied as a single element. This is enabled because the support roll does not act as a constraint for torsion.

The equation that describes the wave equation of a shaft that undergoes torsional loading is the following:

$$\frac{\delta^2 \theta}{\delta t^2} = \frac{GJ}{I_l} \frac{\delta^2 \theta}{\delta x^2}$$

Starting from this expression, it is possible to identify the term that represents the wave propagation speed. Knowing the speed that the wave travels with and the length of the shaft through which this wave travels, we can calculate the ratio of this length with the speed, in order to get the expression of the natural frequency. Obviously, this is only partly correct and it serves only as a way of reasoning, because to get a precise value of the natural frequency, the boundary conditions of the shaft have to be imposed, allowing for the shape function to be properly defined.

$$c = \frac{GJ}{I_l} \left[\frac{\frac{N}{m^2} * m^4}{\frac{Nkg^2}{m}} = \frac{m}{s} \right]$$

Coherently with the assumptions made for the model, a modification has to be made in the expression of the speed, so as to establish a link between the discrete (lumped) system that we are studying and the continuous system we would like to model. This is performed by considering the track chain as a wave motion demonstrator (WMD), following an approach introduced in the Mechanical System Dynamics [5] course held at Politecnico di Torino for the Mechanical Engineering MSc.

The following transformation is performed to get a different expression for the wave speed:

$$c^2 = \frac{GJ_p}{I_l} = \left[\frac{Pa * m^4}{kf * \frac{m^2}{m}} \right] = \left[m^2 \frac{\frac{Nm}{rad}}{kg * m^2} \right] = L^2 \frac{k_T}{I}$$

$$\Rightarrow c = L \sqrt{\frac{k_T}{nI}}$$

- G [MPa]: shear modulus of the material.
- J_p [m^4]: polar moment of inertia of the cross-section.
- I_l [$kg * m$]: mass moment of inertia per unit length.
- L [m]: length of the chain portion under study.
- k_T [Nm/rad]: torsional stiffness.
- I [$kg * m^2$]: mass moment of inertia.
- n : number of track segments.

The wave equation for the shaft in torsion can then be updated with the suggested modification:

$$\frac{\delta^2 \theta}{\delta t^2} = c^2 \frac{\delta^2 \theta}{\delta x^2} = \frac{GJ_p}{I_l} \frac{\delta^2 \theta}{\delta x^2} = L^2 \frac{k_T}{I} \frac{\delta^2 \theta}{\delta x^2}$$

Imposing the boundary conditions (clamped-clamped), allows obtaining the expression of natural frequency.

$$f_i = \frac{i}{2L} \sqrt{\frac{GJ_p}{I_l}} = \frac{i}{2} \sqrt{\frac{k_t}{nI}}$$

The formula for the natural frequency gives the following results for the first five torsional harmonics.

f1 [Hz]	f2 [Hz]	f3 [Hz]	f4 [Hz]	f5 [Hz]
13.37	26.75	40.12	53.50	66.87

Table 2.11. The first five harmonics for the torsion model.

The following table shows, side by side, how the analytical results compare with the results of the simulation. Also for this case the string tension is 15000 N, but this is irrelevant, as tension does not have any contribution in the torsional behavior. This is also clear due to the fact that tension doesn't appear in the wave equation.

Shaft in torsion		
Harmonic	f [Hz] analytical	f [Hz] simulation
1	13.37	17.13
2	26.75	27.22
3	40.12	41.33
4	53.5	54
5	66.87	67

Table 2.12. Comparison between the analytical and simulation results for torsion.

Figure 2.27 shows the deviation of the simulation results from the analytical ones. Except the first natural frequency, all the other ones are quite similar, and the higher the harmonic order, the more approximate they are.

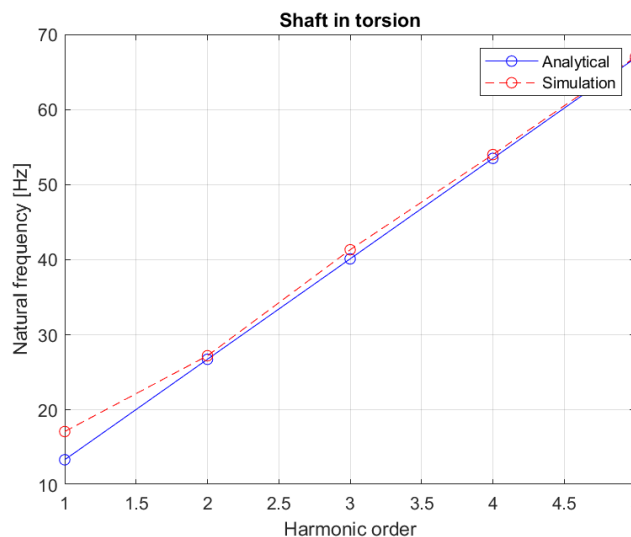


Figure 2.27. Comparison between the analytical and simulation results for chain torsion.

The results obtained above, serve to show that the torsional behavior of the upper part of the track chain can be quite closely approximated with that of a shaft in torsion that is clamped on both sides.

However, it must be noted that this behavior is modeled considering the entire length of the upper part of the chain, namely from the sprocket to the tensioner wheel. The simulations show that the support wheel does not play a role in the torsional behavior and its presence can be neglected. This contrasts the previous case of vertical bending, where the chain had to be divided in two segments that oscillate independently of each other.

2.5 Modeling the track chain lateral bending behavior.

2.5.1 Euler-Bernoulli beam model.

The assumptions made when it comes to modeling the lateral behavior of the chain (bending in the (X-Y) plane) are the following:

- The chain is considered as a Euler-Bernoulli beam.
- Euler-Bernoulli beams display only bending, and not shear forces. This is a strong assumption, as in a realistic scenario, shear actions don't have a negligible contribution.
- The entire length of the chain will be modeled by a single beam, rather than two different beams. This consideration is also quite important, as length appears in the frequency expression, in such a way that increasing it leads to a frequency decrease.

The wave equation for the Euler-Bernoulli beam is given below:

$$\frac{\delta^2 y}{\delta t^2} = - \frac{EJ}{\mu} \frac{\delta^4 y}{\delta x^4}$$

Imposing the boundary conditions for the pinned-pinned beam, a characteristic equation appears (due to the presence of the 4th order partial differential equation). The equation in this case is not complicated, so it can be solved analytically (usually, characteristic equations require a numerical solution). The steps to obtain this equation will not be depicted here, but the results can be summarized as:

$$2\beta^2 \sin(\beta L) \sinh(\beta L) = 0$$

$$\text{Solution: } \sinh(\beta L) = 0 \Rightarrow \beta L = \pi i$$

$$\beta = \frac{\pi}{L} i \Rightarrow \omega_i^2 = \beta^4 \frac{EJ}{\mu}$$

The temporal frequency can be obtained from the spatial frequency in the following way:

$$\omega_i = \frac{\pi^2 i^2}{L^2} \sqrt{\frac{EJ}{\mu}} \Rightarrow f_i = \frac{\pi i^2}{2L^2} \sqrt{\frac{EJ}{\mu}}$$

Seeing that the terms required (in the wave speed) are not readily available by ATV, some correlation should be made between them and the torsional stiffness, which is the quantity that defines the connection between the track elements. In order to do this, we need to perform a linearization of the torsional stiffness, with the aim of obtaining the flexural stiffness.

Figure 2.28 shows the equilibrium performed around point O, which is the ideal inner hinge that connects two consecutive track segments.

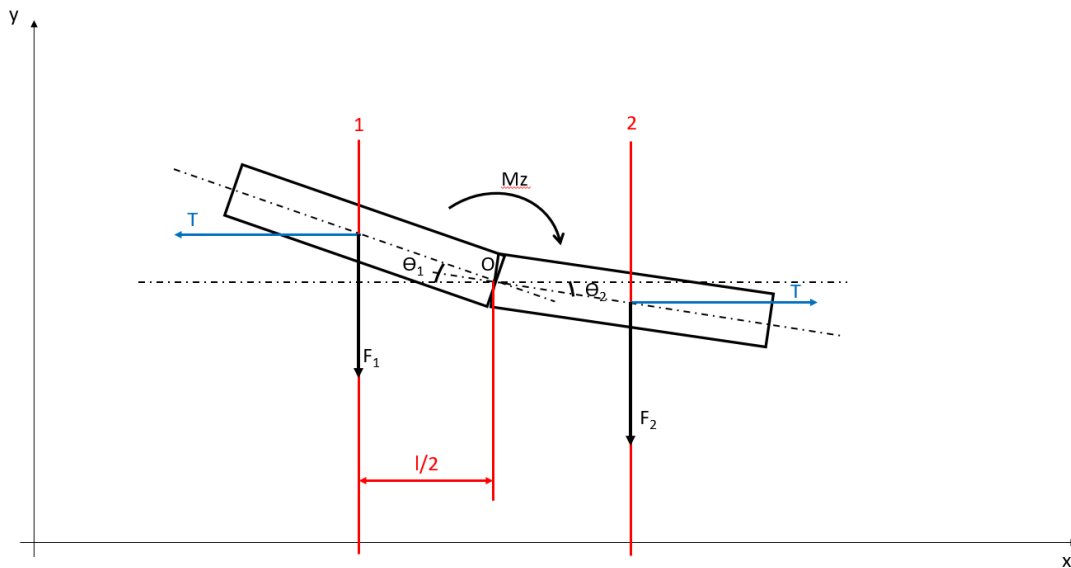


Figure 2.28. Equilibrium around point O in the (X-Y) plane.

The following steps demonstrate how the transverse stiffness k was obtained.

$$M_z = k_T(\theta_2 - \theta_1)$$

$$F_1 = k \cdot \Delta y_1 = k \cdot \frac{l}{2} \cdot \sin \theta_1$$

$$F_2 = k \cdot \Delta y_2 = k \cdot \frac{l}{2} \cdot \sin \theta_2$$

$$O \cup: M_z + F_2 \cdot \frac{l}{2} \cdot \cos \theta_2 - F_1 \cdot \frac{l}{2} \cdot \cos \theta_1 - T \cdot \frac{l}{2} \cdot \sin \theta_1 - T \cdot \frac{l}{2} \cdot \sin \theta_2 = 0$$

$$M_z = F_1 \cdot \frac{l}{2} \cdot \cos \theta_1 - F_2 \cdot \frac{l}{2} \cdot \cos \theta_2 + T \cdot \frac{l}{2} \cdot (\sin \theta_1 + \sin \theta_2)$$

$$M_z = \frac{l}{2} \cdot \left[k \cdot \frac{l}{2} \cdot (\sin \theta_1 \cos \theta_1 - \sin \theta_1 \cos \theta_1) + T \cdot (\sin \theta_1 + \sin \theta_2) \right]$$

$$k_T(\theta_2 - \theta_1) = \frac{l}{2} \cdot \left[k \cdot \frac{l}{2} \cdot (\sin \theta_1 \cos \theta_1 - \sin \theta_1 \cos \theta_1) + T \cdot (\sin \theta_1 + \sin \theta_2) \right]$$

The angles are obtained from the ATV post-processing window:

- $\theta_1 = 0,0039^\circ$
- $\theta_2 = 0,0034^\circ$

Given that the angles are very small the following assumption can be made:

- $\sin \theta_1 \cong \theta_1$
- $\sin \theta_2 \cong \theta_2$
- $\cos \theta_1 \cong 1$
- $\cos \theta_2 \cong 1$

The expression becomes linearized:

$$k_T(\theta_2 - \theta_1) = \frac{l}{2} \cdot \left[k \cdot \frac{l}{2} \cdot (\theta_2 - \theta_1) + T \cdot (\theta_2 + \theta_1) \right]$$

$$k = \frac{4 \cdot k_T(\theta_2 - \theta_1)}{l^2} - \frac{2 \cdot T \cdot (\theta_1 + \theta_2)}{l \cdot (\theta_1 - \theta_2)} \quad \left[\frac{N}{m} \right]$$

The terms that appear in this equation are the following:

- $k \left[\frac{N}{m} \right]$: linear stiffness in the connection between two track pads.
- $k_T \left[\frac{Nm}{rad} \right]$: torsional stiffness in the connection between two track pads.
- $l [m]$: length of the track pad.
- $T [N]$: tension on the chain.

Knowing this stiffness, we can link it with the terms that appear in the wave equation:

$$k = \frac{3EJ}{L^3} \Rightarrow EJ = \frac{kL^3}{3}$$

The natural frequency expression becomes:

$$f_i = \frac{\pi i^2}{2L^2} \sqrt{\frac{kL^3}{3\mu}}$$

Table 2.13 shows the results obtained with the formula above, while Table 2.14 compares these results with the ones from the simulation.

f1 [Hz]	f2 [Hz]	f3 [Hz]	f4 [Hz]	f5 [Hz]
3.17	12.68	28.54	50.73	79.27

Table 2.13. The first five analytical natural frequencies for the chain lateral bending.

Euler-Bernoulli beam		
Harmonic	f [Hz] analytical	f [Hz] simulation
1	3.17	6.31
2	12.68	12.22
3	28.54	19.6
4	50.73	33.3
5	79.27	40.6

Table 2.14. Comparison between the analytical and simulation results for chain lateral bending.

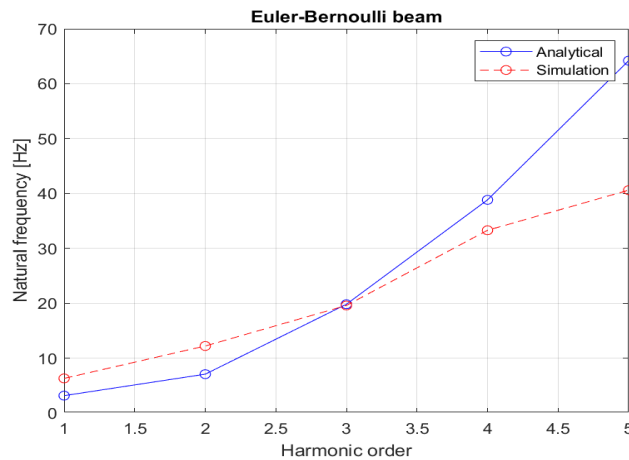


Figure 2.29. Graphical comparison between the analytical and simulation results for chain lateral bending.

Looking at the graph of Figure 2.29, it becomes obvious that the Euler-Bernoulli beam approximation is not accurate at all. Moreover, the simulation results tend to follow an almost linear trend, whereas the Euler-Bernoulli model, being dependent on the square of the harmonic, follows a parabolic trend. In this way, the difference at higher harmonics will be very large. This issue requires a different method to model the chain lateral bending.

2.5.2 Discrete modeling of the chain lateral bending.

To solve the issues that arise when using a Euler-Bernoulli beam model, a discrete model can be implemented, in a manner similar to the one used for the longitudinal bending. The scheme of this model is shown in Figure 2.30, where “i” denotes the generic track pad, that is connected to its left and right with pads “i-1” and “i+1”. The connection is modeled as consisting of linear and torsional springs, because this is the way in which ATV gives its properties (for each connection ATV gives a translational and rotational stiffness). In this analysis, the inner damping of the connection is neglected.

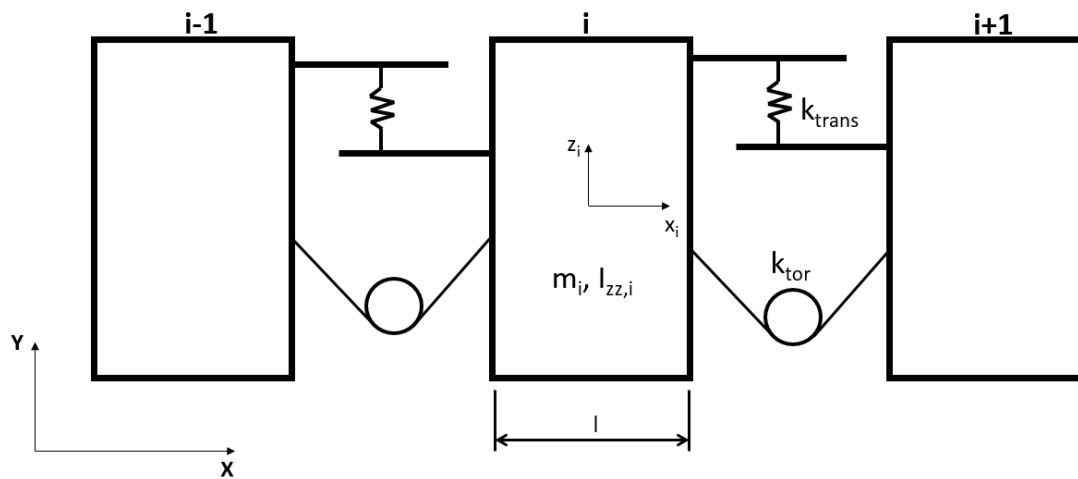


Figure 2.30. Schematic representation of MDOF model for lateral bending.

In this case, the support roll cannot be considered as rigid. In fact, the contact stiffness of the support roll in this direction is much lower than that of the connection. For this reason, the support roll will be modeled as a lumped spring that is connected to the ground. (In reality, the support roll is connected to the hull, which for this static simulation can be considered as the ground). The support roll acts on track pad number 14, and the scheme of the track portion where the support is present is shown in Figure 2.31.

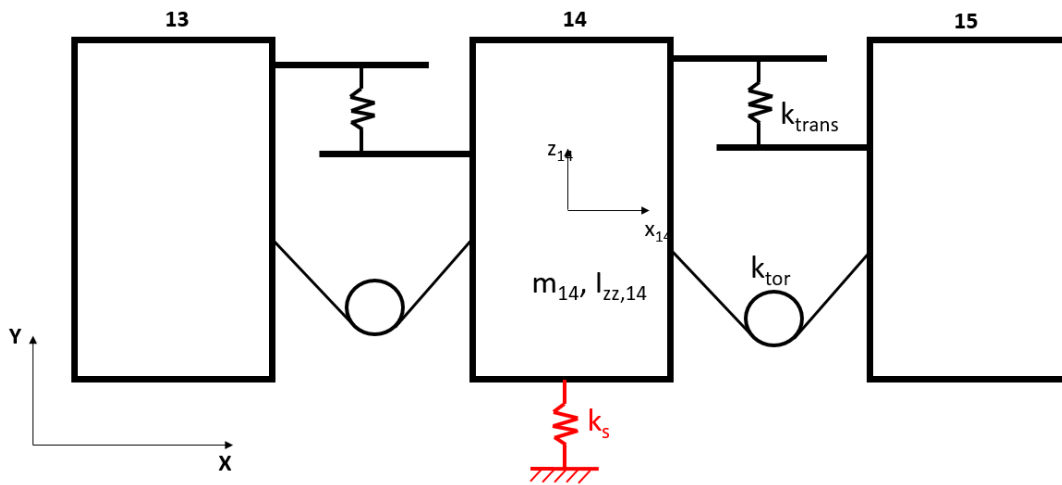


Figure 2.31. Schematic representation of the equivalent lumped spring.

The following images show the free body diagrams required to obtain the mass and stiffness matrices of the multi DOF system.

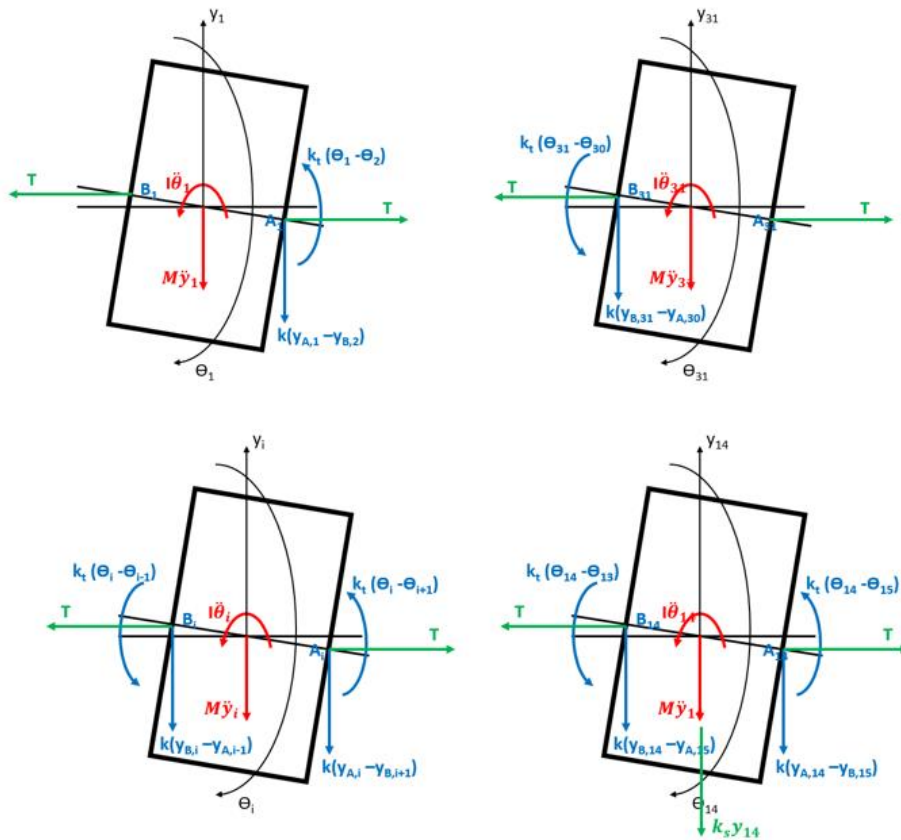


Figure 2.32. Free body diagrams of the track pads.

The images above show respectively:

- Top left: FBD of the first pad "1".
- Top right: FBD of the last pad "31".
- Bottom left: FBD of the generic pad "i".
- Bottom right: FBD of the pad connected to the support roll "14".

The generalized displacement coordinate is the following:

$$\{q\} = \begin{Bmatrix} \{y_{i-1}\} \\ \{\theta_{i-1}\} \\ \{y_i\} \\ \{\theta_i\} \\ \{y_{i+1}\} \\ \{\theta_{i+1}\} \end{Bmatrix}$$

The equations of motion for each body are shown below:

EOM 1:

$$\begin{aligned} \uparrow) M\ddot{y}_1 + ky_1 - k\frac{l}{2}\theta_1 - ky_2 - k\frac{l}{2}\theta_2 &= 0 \\ \curvearrowright) I\ddot{\theta}_1 - k\frac{l}{2}y_1 + (k_t + \frac{kl^2}{4} + Tl)\theta_1 + k\frac{l}{2}y_2 - (k_t + \frac{kl^2}{4})\theta_2 &= 0 \end{aligned}$$

EOM 31:

$$\begin{aligned} \uparrow) M\ddot{y}_{31} + ky_{31} + k\frac{l}{2}\theta_{31} - ky_{30} + k\frac{l}{2}\theta_{30} &= 0 \\ \curvearrowright) I\ddot{\theta}_{31} - k\frac{l}{2}y_{30} - (k_t + \frac{kl^2}{4})\theta_{30} + k\frac{l}{2}y_{31} + (k_t + \frac{kl^2}{4} + Tl)\theta_{31} &= 0 \end{aligned}$$

EOM i:

$$\begin{aligned} \uparrow) M\ddot{y}_i - ky_{i-1} + 2ky_i - ky_{i+1} + k\frac{l}{2}\theta_{i-1} - k\frac{l}{2}\theta_{i+1} &= 0 \\ \curvearrowright) I\ddot{\theta}_i - k\frac{l}{2}y_{i-1} - (k_t + \frac{kl^2}{4})\theta_{i-1} + (2k_t + \frac{kl^2}{2} + Tl)\theta_i + k\frac{l}{2}y_{i+1} - (k_t + \frac{kl^2}{4})\theta_{i+1} &= 0 \end{aligned}$$

EOM 14:

$$\begin{aligned} \uparrow) M\ddot{y}_{14} - ky_{13} + (2k + k_s)y_{14} - ky_{15} + k\frac{l}{2}\theta_{13} - k\frac{l}{2}\theta_{15} &= 0 \\ \curvearrowright) I\ddot{\theta}_{14} - k\frac{l}{2}y_{13} - (k_t + \frac{kl^2}{4})\theta_{13} + (2k_t + \frac{kl^2}{2} + Tl)\theta_{14} + k\frac{l}{2}y_{15} - (k_t + \frac{kl^2}{4})\theta_{15} &= 0 \end{aligned}$$

The terms on the equations above are arranged in the mass and stiffness matrices as follows:

$$[M] = \begin{bmatrix} \begin{bmatrix} M_{i-1} & 0 \\ 0 & I_{i-1} \end{bmatrix} & 0 & 0 \\ 0 & \begin{bmatrix} M_i & 0 \\ 0 & I_i \end{bmatrix} & 0 \\ 0 & 0 & \begin{bmatrix} M_{i+1} & 0 \\ 0 & I_{i+1} \end{bmatrix} \end{bmatrix}$$

$$[K_i] = \begin{bmatrix} 2k & 0 \\ 0 & 2k_t + \frac{kl^2}{2} + Tl \end{bmatrix}$$

$$[K_{i-1}] = \begin{bmatrix} -k & \frac{kl}{2} \\ -\frac{kl}{2} & -k_t + \frac{kl^2}{4} \end{bmatrix}$$

$$[K_{i+1}] = \begin{bmatrix} -k & -\frac{kl}{2} \\ \frac{kl}{2} & -k_t + \frac{kl^2}{4} \end{bmatrix}$$

$$[K_1] = \begin{bmatrix} k & 0 \\ 0 & k_t + \frac{kl^2}{4} + Tl \end{bmatrix}$$

$$[K_{31}] = \begin{bmatrix} k & 0 \\ 0 & k_t + \frac{kl^2}{4} + Tl \end{bmatrix}$$

$$[K] = \begin{bmatrix} [K_1] & [K_{i+1}] & 0 & 0 & 0 \\ 0 & \ddots & 0 & 0 & 0 \\ 0 & [K_{i-1}] & [K_i] & [K_{i+1}] & 0 \\ 0 & 0 & 0 & \ddots & 0 \\ 0 & 0 & 0 & [K_{i-1}] & [K_{31}] \end{bmatrix}$$

The mass and stiffness matrices are implemented in MATLAB and the eigenvalue problem is solved. In this way, the eigenvalues and the natural frequencies are obtained. The results obtained are summarized in the following table, where alongside them are also the results of the Euler-Bernoulli model and of the simulation. The first 20 harmonics are considered to have a thorough comparison between the models.

Harmonic	Euler-Bernoulli	Discrete	Simulation
1	3.17	4.07	
2	12.68	5.84	6.31
3	28.54	11.75	12.20
4	50.73	19.22	19.60
5	79.27	28.51	33.30
6	114.14	39.54	40.60
7	155.33	51.31	57.20
8	202.88	64.16	69.84
9	256.77	77.30	82.63
10	317.00	90.84	99.92
11	383.57	104.37	110.83
12	456.48	117.83	126.26
13	535.73	131.06	140.74
14	621.32	143.92	150.79
15	713.25	156.40	165.69
16	811.52	168.36	175.90
17	916.13	179.82	187.18
18	1027.08	190.69	201.18
19	1144.37	200.96	206.43
20	1268.00	210.58	218.93

Table 2.15. Summary of the results obtained for the two models and simulation.

The following plots show graphically the results summarized in the table above. The second one shows only the comparison between the simulation and the discrete model, so that the differences between them can be highlighted better.

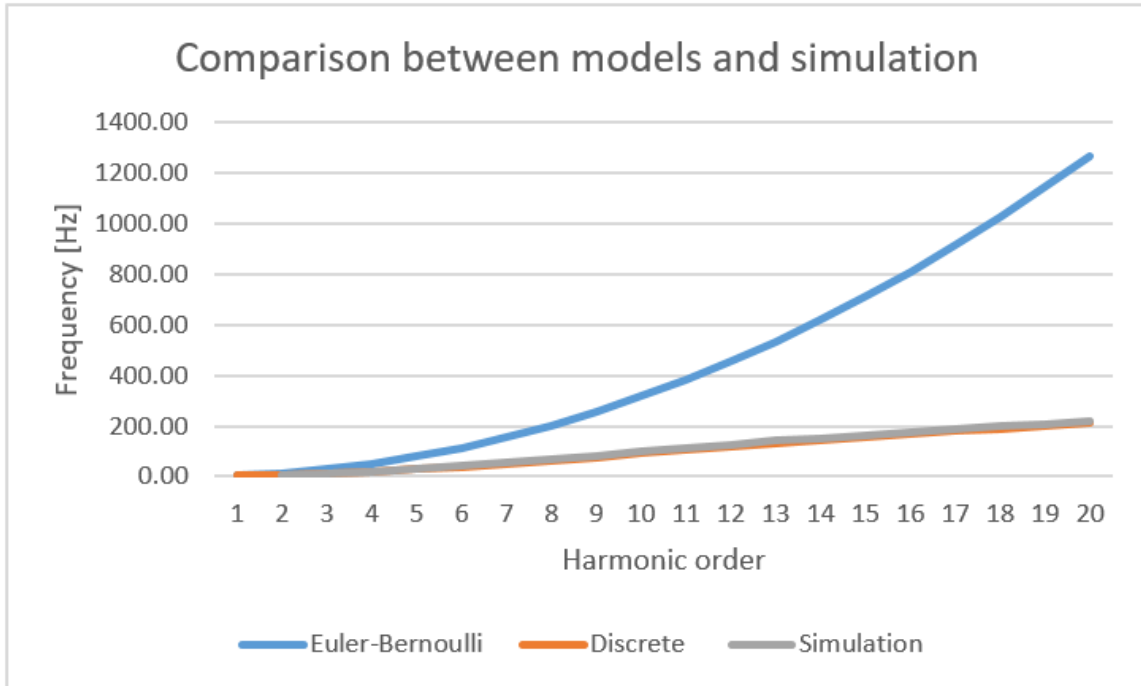


Figure 2.33. Graphical comparison between the models and simulation.

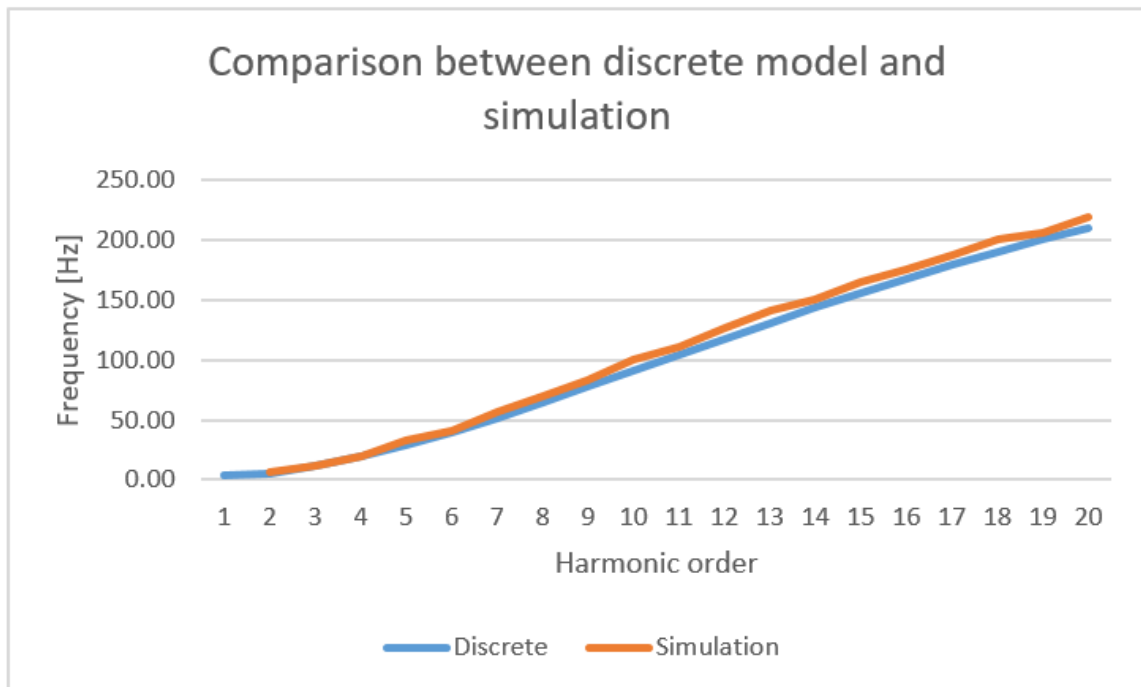


Figure 2.34. Graphical representation between the discrete model and simulation.

Figure 2.35 shows the similarity between the lateral bending second mode shape and the second eigenvector of the discrete model. It is interesting to see how the eigenvector correctly describes the behavior shown in the simulation and how the support roll, which was modeled as a lumped spring, modifies the system's behavior to correctly predict the result.

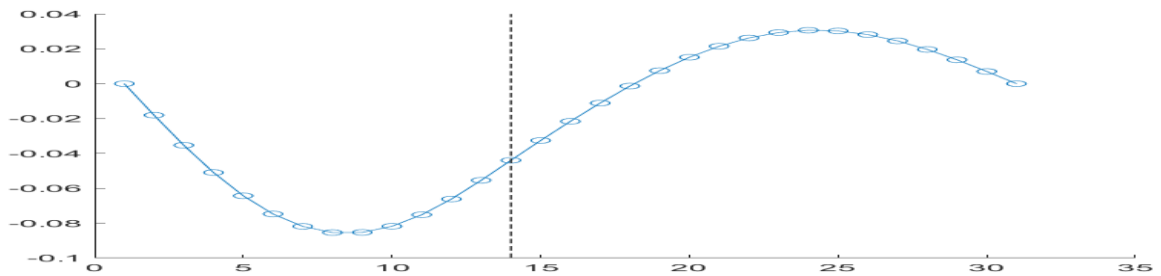
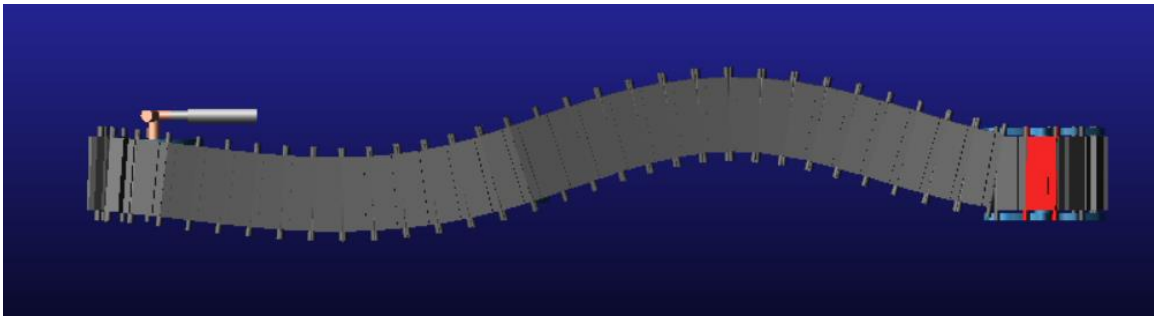


Figure 2.35. Comparison between simulation mode shape and discrete model eigenvector.

2.6 Summarizing the modeling results.

The results obtained so far will be summarized in tables and the best analytical model for each chain behavior will be highlighted based on the error between the analytical and simulation results. The error will be defined as:

- Δf : absolute error, calculated as the difference between the simulation and analytical results.
- $\Delta f/f$: relative error, calculated as the ratio of the difference between the simulation and analytical results and analytical result.

Table 2.16 and Table 2.17 show the error in approximation for each of the three methods used to model the longitudinal bending modes ((X-Z) plane).

Segment 1						
Harmonic	Continuous 1		Continuous 2		Discrete	
	Δf	$\Delta f/f$	Δf	$\Delta f/f$	Δf	$\Delta f/f$
1	0.88	35%	0.51	20%	0.34	14%
2	0.97	23%	0.23	5%	0.12	3%
3	1.63	25%	0.52	8%	0.06	1%
4	2.15	25%	0.67	8%	0.21	2%
5	2.86	26%	1.01	9%	0.26	2%
6	3.68	27%	1.45	11%	0.32	2%
7	4.65	29%	2.05	13%	0.36	2%
8	5.70	30%	2.73	14%	0.47	2%
9	6.96	32%	3.62	17%	0.53	2%
10	8.40	34%	4.69	19%	0.58	2%
11	9.86	35%	5.78	21%	0.73	3%
12	11.68	37%	7.23	23%	0.58	2%
13	13.35	38%	8.53	25%	0.51	1%
14	14.73	39%	9.54	25%	0.44	1%
15	15.79	39%	10.23	25%	0.16	0%
16	15.88	38%	9.95	24%	0.02	0%

Table 2.16. Segment 1 results for vertical bending ((X-Z) plane).

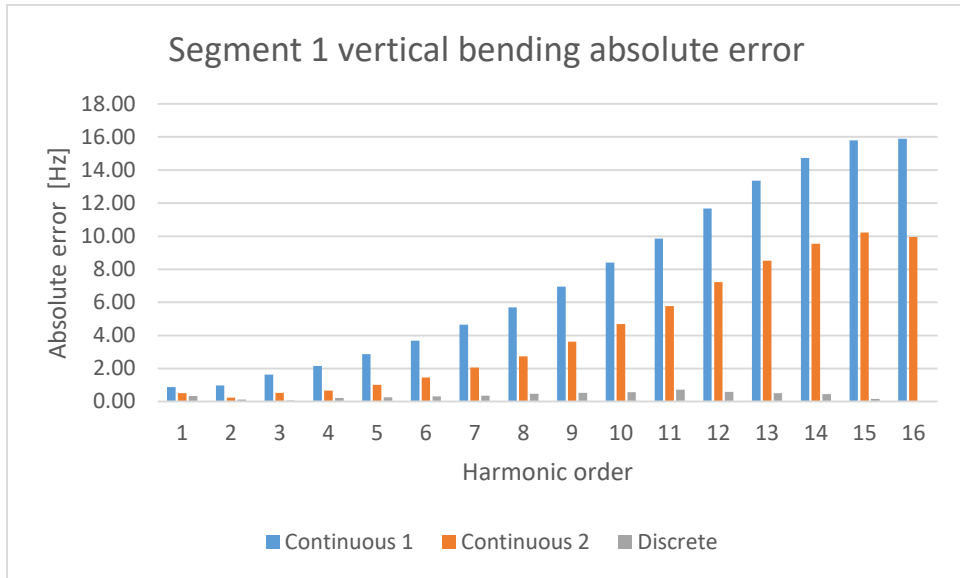


Figure 2.36. Segment 1 vertical bending absolute error.

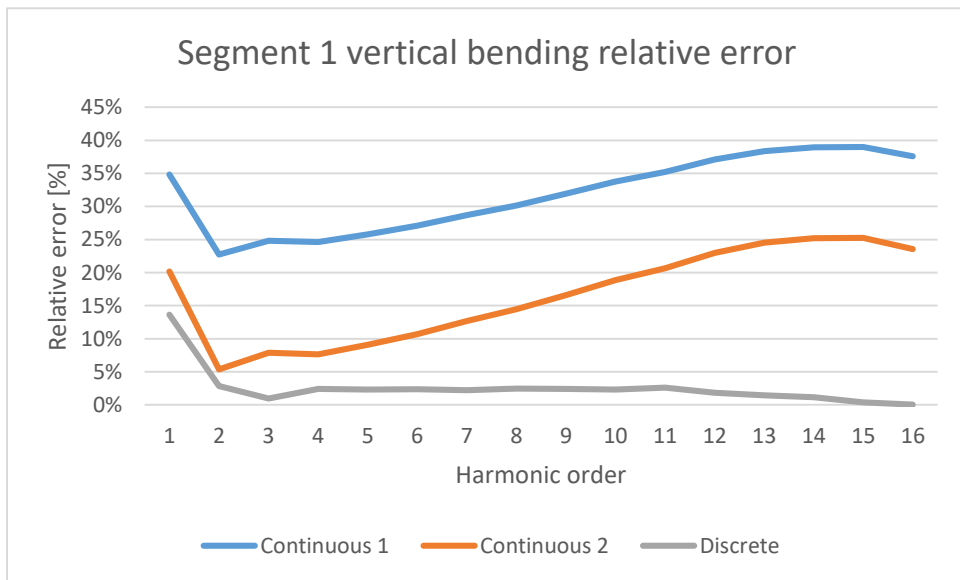


Figure 2.37. Segment 1 vertical bending relative error

Segment 2						
Harmonic	Continuous 1		Continuous 2		Discrete	
	Δf	$\Delta f/f$	Δf	$\Delta f/f$	Δf	$\Delta f/f$
1	1.06	31%	0.57	17%	0.23	7%
2	1.7	27%	0.72	11%	0.03	0%
3	2.83	29%	1.36	14%	0.08	1%
4	4.29	32%	2.33	17%	0.32	2%
5	5.95	34%	3.5	20%	0.51	3%
6	8.21	37%	5.27	24%	0.99	4%
7	10.71	40%	7.28	27%	1.39	5%
8	13.68	43%	9.76	30%	2.03	6%
9	16.51	44%	12.1	32%	2.55	7%
10	18.07	44%	13.17	32%	2.31	6%

Table 2.17. Segment 2 results for vertical bending ((X-Z) plane).

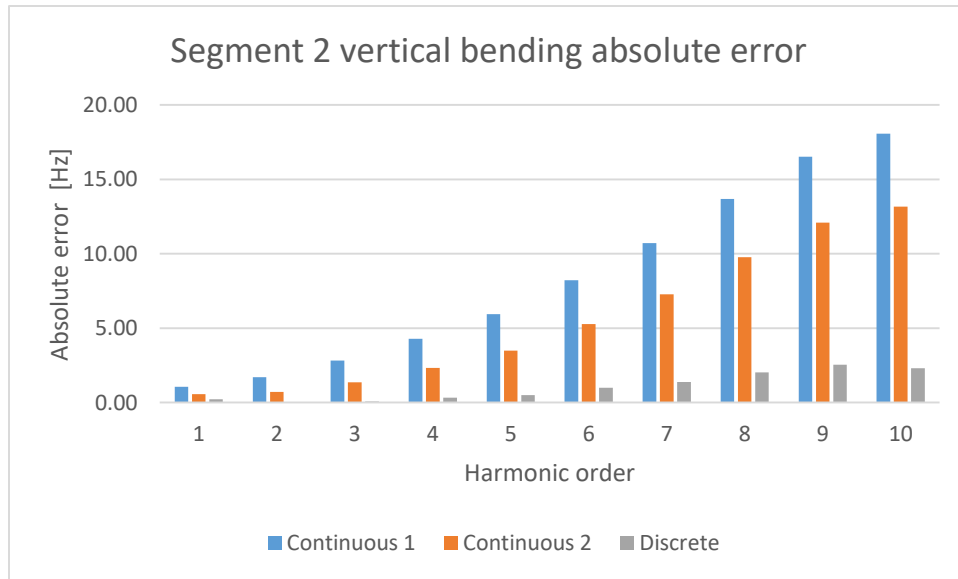


Figure 2.38. Segment 2 vertical bending absolute error.

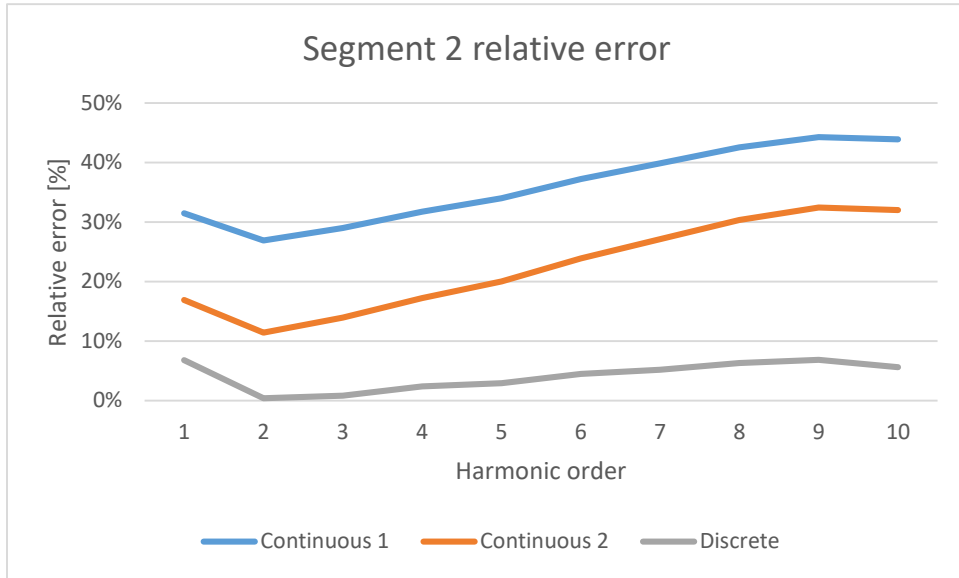


Figure 2.39. Segment 2 vertical bending relative error.

Table 2.18 summarizes the results obtained for the chain torsion. In the case of torsion, only one model was proposed.

Harmonic	Shaft model	Simulation	Δf	$\Delta f/f$
1	13.37	17.13	3.76	22%
2	26.74	27.22	0.48	2%
3	40.11	41.33	1.22	3%
4	53.48	54	0.52	1%
5	66.85	67	0.15	0%
6	80.22	80	0.22	0%
7	93.59	92.45	1.14	1%
8	106.96	104.25	2.71	3%
9	120.33	119.8	0.53	0%
10	133.7	130.72	2.98	2%

Table 2.18. Chain torsional oscillations results.

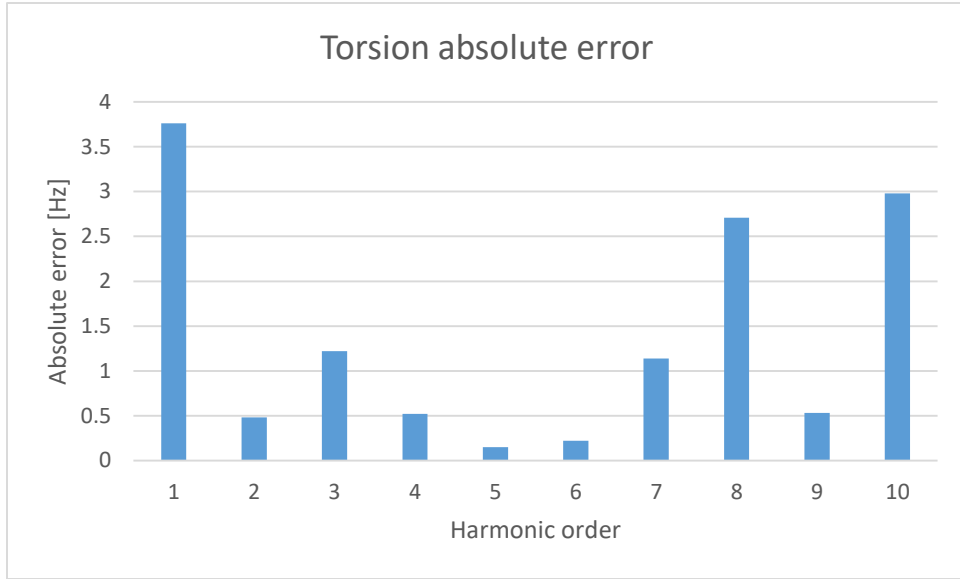


Figure 2.40. Chain torsion absolute error.

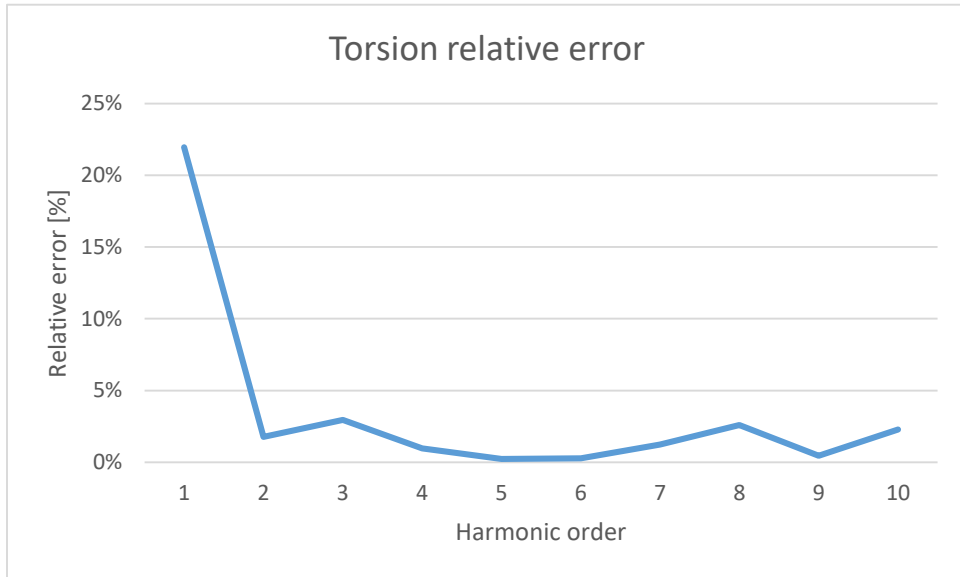


Figure 2.41. Chain torsion relative error.

Table 2.19 summarizes the results for each of the two methods used to model the chain lateral bending.

Chain lateral bending				
	Continuous		Discrete	
Harmonic	Δf	$\Delta f/f$	Δf	$\Delta f/f$
2	6.37	101%	0.47	7%
3	16.34	134%	0.45	4%
4	31.13	159%	0.38	2%
5	45.97	138%	4.79	14%
6	73.54	181%	1.06	3%
7	98.13	172%	5.89	10%
8	133.04	190%	5.68	8%
9	174.14	211%	5.33	6%
10	217.08	217%	9.08	9%
11	272.74	246%	6.46	6%
12	330.22	262%	8.43	7%
13	394.99	281%	9.68	7%
14	470.53	312%	6.87	5%
15	547.56	330%	9.29	6%
16	635.62	361%	7.54	4%
17	728.95	389%	7.36	4%
18	825.9	411%	10.49	5%
19	937.94	454%	5.47	3%
20	1049.07	479%	8.35	4%

Table 2.19. Chain lateral bending results.

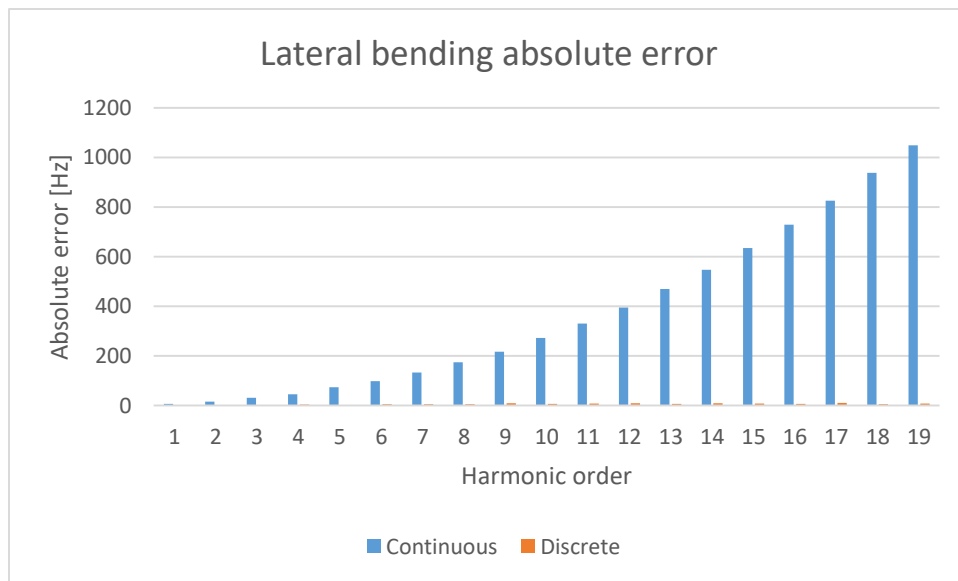


Figure 2.42. Chain lateral bending absolute error.

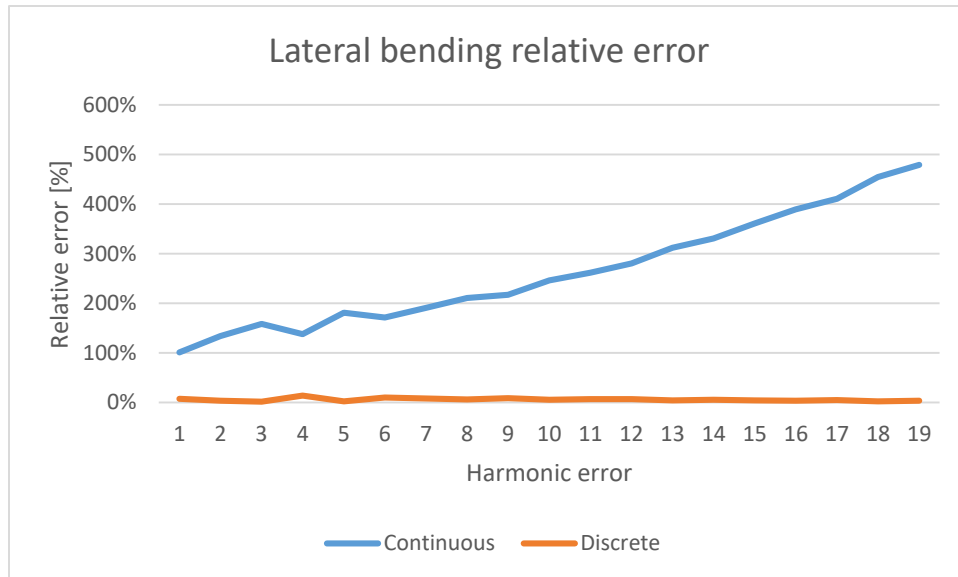


Figure 2.43. Chain lateral bending relative error.

Some remarks can be made about the results shown in the tables above:

- The analytical results obtained for the equivalent string (strings 1 and 2) are quite close to the ones of the simulation. The error between the first modes is quite large, but it gets smaller at the consecutive modes. It is interesting to note that the error between the simulation and analytical results is considerably less for string 1, compared to string 2. This could imply that the string hypotheses are more approximate for segment 1. This is actually reasonable, because due to string 1 being longer, the mass is better distributed along its length.
- Even though the continuous string model manages to approximate well the chain modes, the discrete model is far superior and it introduces a very small error compared to the continuous model.
- In the case of torsional behavior, except for the first mode, which shows considerable differences between the analytical solution and the simulation, all the others are very closely approximated, and it can be noticed that the difference becomes very small for higher harmonic orders.
- The Euler-Bernoulli beam model shows significant differences with the lateral bending behavior depicted by the simulation. This can be interpreted as being due to reasons that are related to the boundary conditions, as well as the

assumptions made. The difference becomes very significant at higher harmonics, and for this reason the beam model is not a reliable way of modeling the chain.

- Similar to the discrete model used in longitudinal bending, the discrete model used for the lateral bending gives very good results, that differ very slightly from those of the simulation.
- As a general remark, the discrete model gives the best overall approximation, but the continuous system model is more easy to implement.

3 Sensitivity analysis

This chapter consists of a sensitivity analysis, performed by changing parameters of the default model. The results obtained with the changes will be compared to the ones of the original.

3.1 Rotational stiffness modification.

The rotational stiffness in the Y-direction is the term that ATV uses to refer to the torsional stiffness of the connection between two consecutive track segments. ATV, being a multi-body software, considers the parts as rigid, while the connection between them is such that it takes into account not only the properties of the link itself, but also the elastic properties that the parts it connects would otherwise have.

ATV models the connection as having very large stiffness in two of the directions and very low stiffness in the other, realizing an element that is a revolute joint (hinge). An ideal hinge has infinite stiffness in two directions, and a zero stiffness in the third. The default values are reported below, as referred to the local reference frame, depicted in Figure 3.1:

- Rotational stiffness in the x-direction: $3000000 \frac{Nmm}{\circ}$
- Rotational stiffness in the y-direction: $3000000 \frac{Nmm}{\circ}$
- Rotational stiffness in the z-direction: $30 \frac{Nmm}{\circ}$

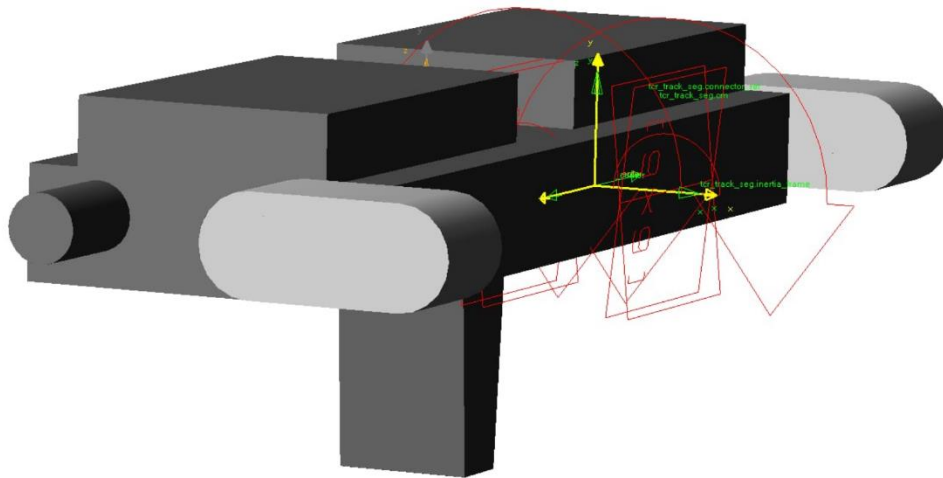


Figure 3.1. Local reference frame for the track segment.

As can be seen, contrary to the global reference frame, the part reference frame has the y-axis pointing upwards in the vertical direction and the z-axis in the lateral direction. This will be specified in every section where the reference frame definition is required, as this difference between the part and global references might lead to confusion.

The parameters of the simulation with the modified stiffness (increased by two orders of magnitude) are summarized below (parameters referred to the part reference frame):

- Rotational stiffness in the x-direction: $3000000 \frac{Nmm}{\circ}$
- Rotational stiffness in the y-direction: $3000000 \frac{Nmm}{\circ}$
- Rotational stiffness in the z-direction: $3000 \frac{Nmm}{\circ}$
- Tensioner force: $15000 N$

The results of the simulation with the modified stiffness are reported in Table 3.1, which gives a comparison for all the behaviors that were studied in the previous sections

String 1	f [Hz]	ζ [%]	String 1	f [Hz]	ζ [%]
1	2.53	5.26	1	2.49	5.84
2	4.27	1.56	2	4.29	1.78
3	6.58	3.12	3	6.49	2.35
4	8.74	2.78	4	9.01	2.57
5	11.1	3.18	5	11.6	2.51
String 2	f [Hz]	ζ [%]	String 2	f [Hz]	ζ [%]
1	3.37	10.73	1	3.23	12.15
2	6.32	1.51	2	6.25	0.21
3	9.76	1.49	3	9.68	0.52
4	13.53	1.25	4	13.42	1.13
5	17.51	0.69	5	17.59	1.65
Bending	f [Hz]	ζ [%]	Bending	f [Hz]	ζ [%]
1	6.31	12.17	1	6.24	12.07
2	12.22	19.35	2	12	19.37
3	19.6	14.42	3	19.4	14.04
4	33.3	12.41	4	32.95	12.43
5	40.6	16.45	5	40	16.12
Torsion	f [Hz]	ζ [%]	Torsion	f [Hz]	ζ [%]
1	17.13	6.45	1	16.9	6.34
2	27.22	2.61	2	26.97	2.65
3	41.33	4.65	3	40.88	4.43
4	54	4.19	4	53.49	4.16
5	67	4.39	5	66.25	4.21

Table 3.1. The left side shows the results of the original simulation, while the right side shows the results with the modified stiffness ($3000 Nmm/\circ$).

As can be seen from the table, the differences between the two sets of results are very minor, and they can be attributed to the fact that each simulation yields different results, even if run with the exact same settings. The minor differences can be appreciated in the graphs of Figure 3.2.

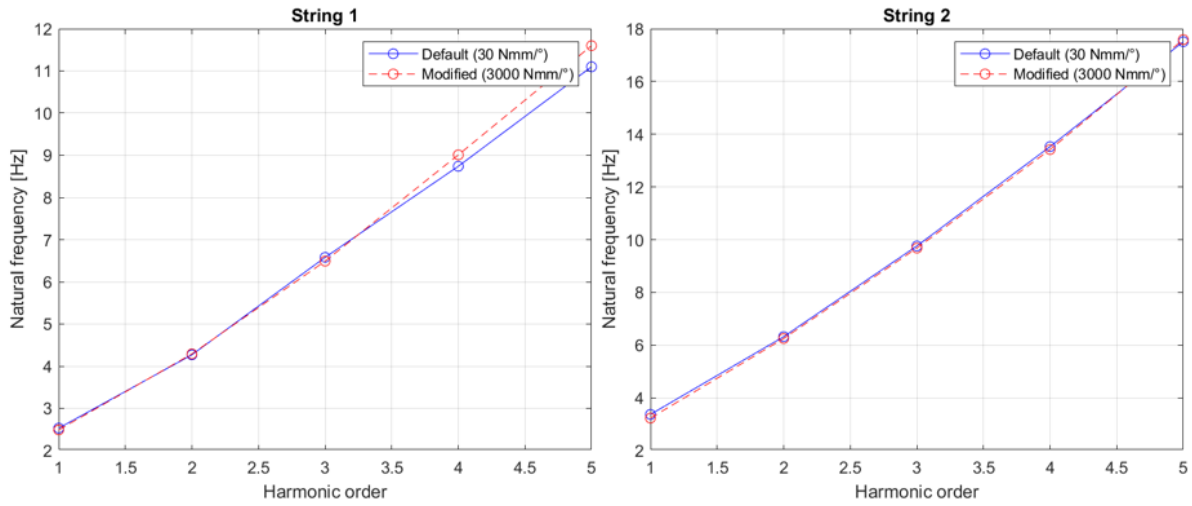


Figure 3.2. Deviation between the original and modified results for an increase of two orders of magnitude.

However, the fact is that the increase of stiffness is quite insignificant compared to the stiffness in the other two directions, allowing the connection to retain its properties as a hinge.

An additional increase with three orders of magnitude, yields considerable differences compared to the default model. The results of the simulation with a rotational stiffness of 30000 Nmm/° are summarized in Table 19, while Figure 24 highlights the deviation of the results of the modified model compared to the original.

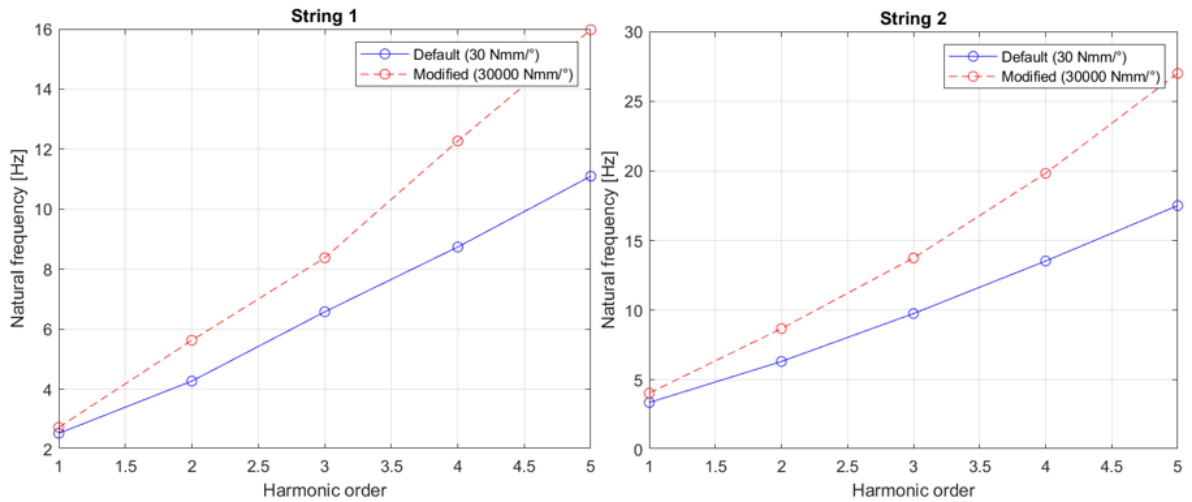


Figure 3.3. Deviation between the original and modified results for an increase of three orders of magnitude.

String 1	f [Hz]	ζ [%]	String 1	f [Hz]	ζ [%]
1	2.53	5.26	1	2.73	2.33
2	4.27	1.56	2	5.63	1.54
3	6.58	3.12	3	8.38	0.68
4	8.74	2.78	4	12.27	2.74
5	11.1	3.18	5	15.98	1.17
String 2	f [Hz]	ζ [%]	String 2	f [Hz]	ζ [%]
1	3.37	10.73	1	4.05	2.08
2	6.32	1.51	2	8.68	0.3
3	9.76	1.49	3	13.75	0.27
4	13.53	1.25	4	19.83	0.57
5	17.51	0.69	5	27	2.94
Bending	f [Hz]	ζ [%]	Bending	f [Hz]	ζ [%]
1	6.31	12.17	1	6.57	12.33
2	12.22	19.35	2	12.08	16.89
3	19.6	14.42	3	19.98	12.41
4	33.3	12.41	4	32.16	9.76
5	40.6	16.45	5	40.04	12.56
Torsion	f [Hz]	ζ [%]	Torsion	f [Hz]	ζ [%]
1	17.13	6.45	1	16.17	5.67
2	27.22	2.61	2	26.49	2.36
3	41.33	4.65	3	40.1	3.71
4	54	4.19	4	52.53	3.76
5	67	4.39	5	65.08	3.37

Table 3.2. The left side shows the results of the original simulation, while the right side shows the results with the modified stiffness (30000 Nmm/°).

Regarding the results of Table 3.2, the following remarks can be made:

- The frequencies of segment 1 and 2 are increased considerably, especially for the higher harmonics. This is to be expected, since an increased stiffness would move the behavior closer to that of a beam, rather than a string.
- The increased stiffness implies an increase of the flexural rigidity of the chain, once again deviating from the string-like behavior. This is obvious due to the fact that the chain does not fully wrap around the wheels, as it did in the previous simulations. This is highlighted in Figure 3.4.
- This lack of compliance from the chain changes the boundary conditions, as rotation around the point of constraint is not allowed anymore.
- The behaviors of the two segments, which with the original stiffness could be considered independent, are now coupled, and in a few modes, excitation of one segment is accompanied by a subsequent excitation on the other segment.
- As a general remark, the stiffness of 30000 Nmm/°, yields a situation that can be considered as intermediate between a string and a beam.

- It is also interesting to notice that the lateral bending and the torsion behavior are not influenced at all by the stiffness increase. This is because torsion and lateral bending occur in other planes (lateral bending in the (x-y) plane and torsion is around the x-axis), so the stiffness modification in the y-direction (referred to the global reference frame), has no effect on them.

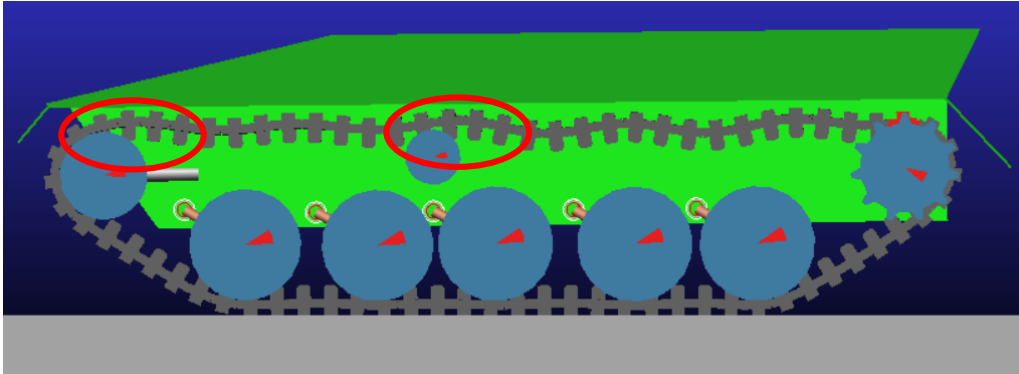


Figure 3.4. Chain does not fully wrap around the wheels.

If the same simulation is performed with an even higher rotational stiffness in the z-direction (referred to the part reference frame), namely $300000 \text{ Nmm}/^\circ$, the track cannot even wrap around the wheels, as shown in Figure 3.5. By bringing the z-direction stiffness to an order of magnitude lower than the other two, the hinge-like properties of the connection are lost, and all the considerations and assumptions we made in the previous sections, when modeling of the track as a continuous system, will no longer hold.

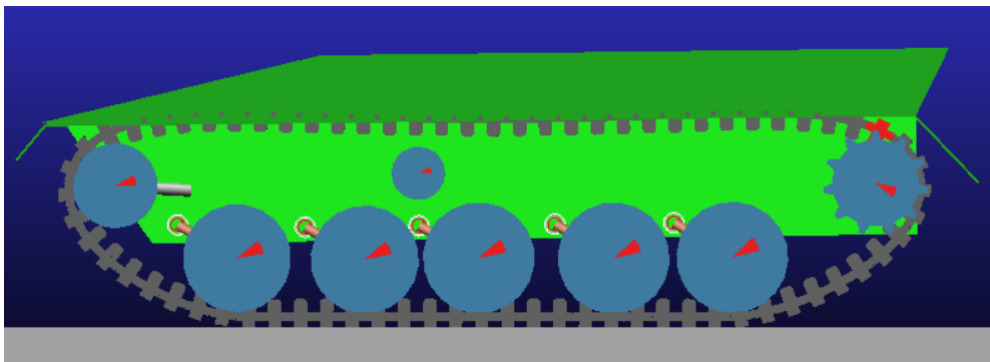


Figure 3.5. Track deformation for the z-direction stiffness of $300000 \text{ Nmm}/^\circ$.

3.2 Rotational damping modification.

The rotational damping refers to the damping assigned to the connection between two consecutive track segments. It is a property of the connection, that just like the rotational stiffness, takes into account also the properties of the segments it connects, which are considered as rigid, following the multi-body approach. It can be modified, by changing its order of magnitude, in order to highlight the effect this parameter has on the frequency.

The default values of the rotational damping are (referred to the part reference frame):

- Rotational damping in the x-direction: $200 \frac{Nmms}{\circ}$
- Rotational damping in the y-direction: $200 \frac{Nmms}{\circ}$
- Rotational damping in the z-direction: $0,1745 \frac{Nmms}{\circ}$

The sensible parameter to vary is the damping in the z-direction, as it is the direction that enables what was previously called the “hinge-like” behavior. The first modification increases the damping by two orders of magnitude:

- Rotational damping in the z-direction: $17,45 \frac{Nmms}{\circ}$

The comparison between the results obtained with the default model and the modified model are shown in Table 3.3, while the following figures represent graphically the results of Table 3.3.

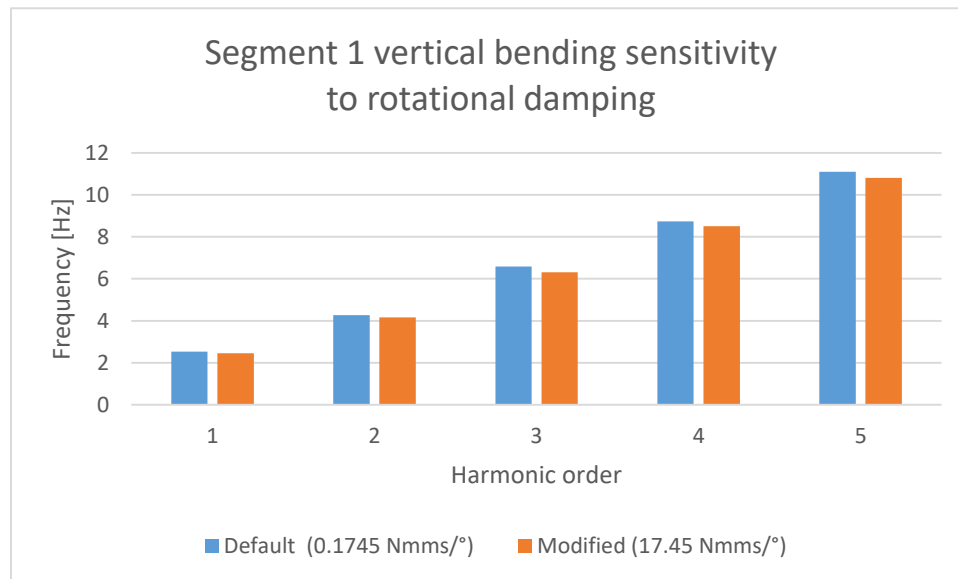


Figure 3.6. Segment 1 vertical bending sensitivity to rotational bending.

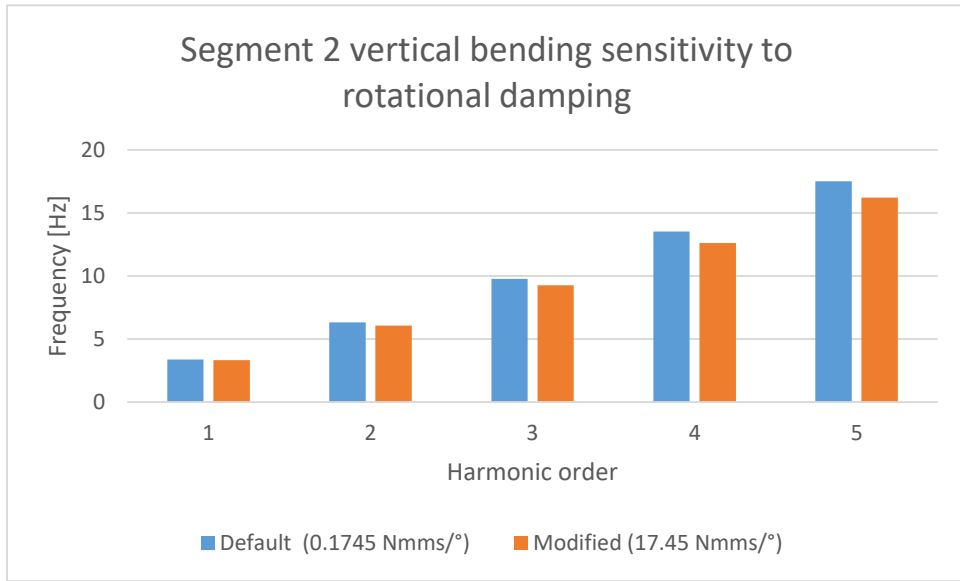


Figure 3.7. Segment 2 vertical bending sensitivity to rotational bending.

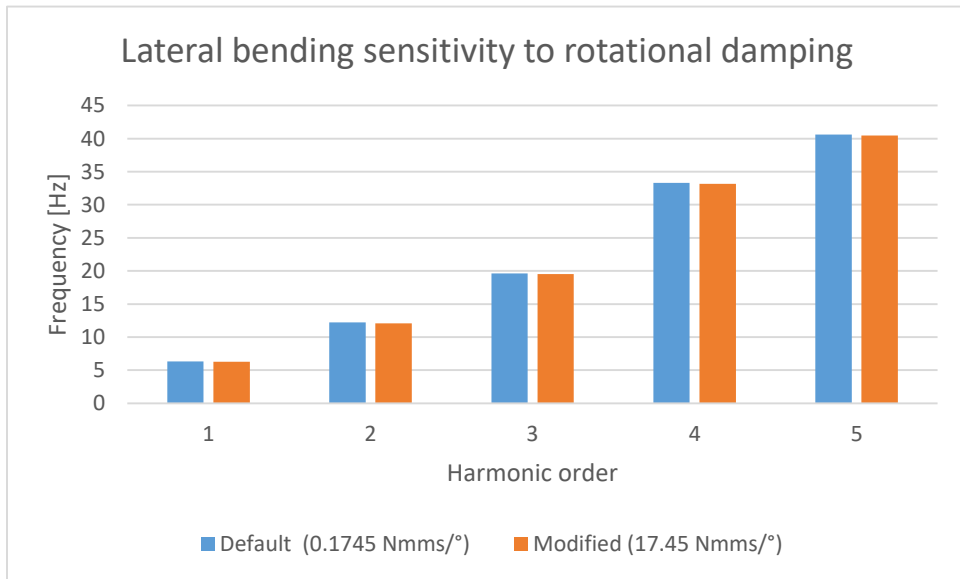


Figure 3.8. Lateral bending sensitivity to rotational bending.

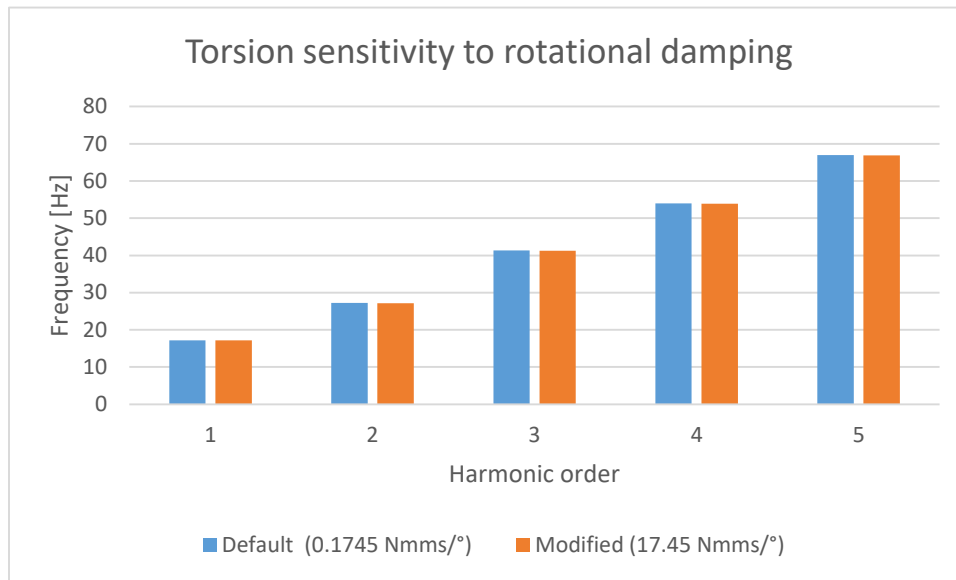


Figure 3.9. Torsion sensitivity to rotational damping.

String 1	f [Hz]	ζ [%]
1	2.53	5.26
2	4.27	1.56
3	6.58	3.12
4	8.74	2.78
5	11.1	3.18

String 1	f [Hz]	ζ [%]
1	2.46	4.92
2	4.17	0.54
3	6.31	2.41
4	8.51	1.41
5	10.8	2.32

String 2	f [Hz]	ζ [%]
1	3.37	10.73
2	6.32	1.51
3	9.76	1.49
4	13.53	1.25
5	17.51	0.69

String 2	f [Hz]	ζ [%]
1	3.32	13.29
2	6.05	1.05
3	9.26	2.07
4	12.61	3.4
5	16.21	5.74

Bending	f [Hz]	ζ [%]
1	6.31	12.17
2	12.22	19.35
3	19.6	14.42
4	33.3	12.41
5	40.6	16.45

Bending	f [Hz]	ζ [%]
1	6.27	12.21
2	12.1	19.61
3	19.54	14.54
4	33.19	12.67
5	40.45	16.52

Torsion	f [Hz]	ζ [%]
1	17.13	6.45
2	27.22	2.61
3	41.33	4.65
4	54	4.19
5	67	4.39

Torsion	f [Hz]	ζ [%]
1	17.13	6.48
2	27.15	2.63
3	41.26	4.72
4	53.9	4.17
5	66.88	4.45

Table 3.3. The left side shows the results of the default model, while the right side shows the results obtained with the modified damping (17.45 Nmms/°).

The first remark is that the damping modification in the z-direction (part reference frame) impacts only the string-like behavior in the (X-Y) plane (global reference frame). Since the properties referred to the z-direction do not influence the lateral bending and torsion, the frequencies of these modes are not sensitive to changes in this damping. Additionally, a decrease of frequency for the modified model, especially visible for higher harmonics, can be noticed between equivalent modes. This is exactly what one would expect by increasing the damping.

The next modification increases the damping by three orders of magnitude, bringing it to a value that is close to the damping in the other two directions.

- Rotational damping in the z-direction: $174,5 \frac{Nmms}{\circ}$

String 1	f [Hz]	ζ [%]
1	2.53	5.26
2	4.27	1.56
3	6.58	3.12
4	8.74	2.78
5	11.1	3.18

String 1	f [Hz]	ζ [%]
1	2.44	5.92
2	4.1	2.76
3	6.21	7.67
4	8.41	10.65
5	10.67	18.86

String 2	f [Hz]	ζ [%]
1	3.37	10.73
2	6.32	1.51
3	9.76	1.49
4	13.53	1.25
5	17.51	0.69

String 2	f [Hz]	ζ [%]
1	3.32	18.83
2	5.98	5.6
3	9.15	13.92
4	12.47	27.07
5	16.14	50.07

Bending	f [Hz]	ζ [%]
1	6.31	12.17
2	12.22	19.35
3	19.6	14.42
4	33.3	12.41
5	40.6	16.45

Bending	f [Hz]	ζ [%]
1	6.26	12.26
2	12.05	19.54
3	19.51	14.62
4	33.12	12.76
5	40.4	16.55

Torsion	f [Hz]	ζ [%]
1	17.13	6.45
2	27.22	2.61
3	41.33	4.65
4	54	4.19
5	67	4.39

Torsion	f [Hz]	ζ [%]
1	17.14	6.43
2	27.15	2.65
3	41.26	4.72
4	53.88	4.16
5	66.86	4.43

Table 3.4. The left side shows the results of the default model, while the right side shows the results obtained with the modified damping ($174.45 Nmms/\circ$).

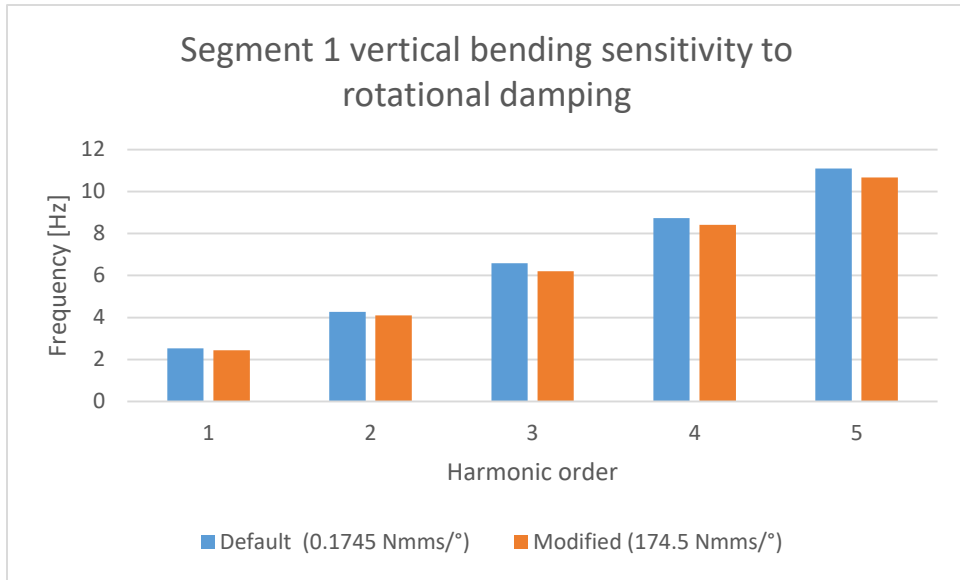


Figure 3.10. Segment 1 vertical bending sensitivity to rotational damping.

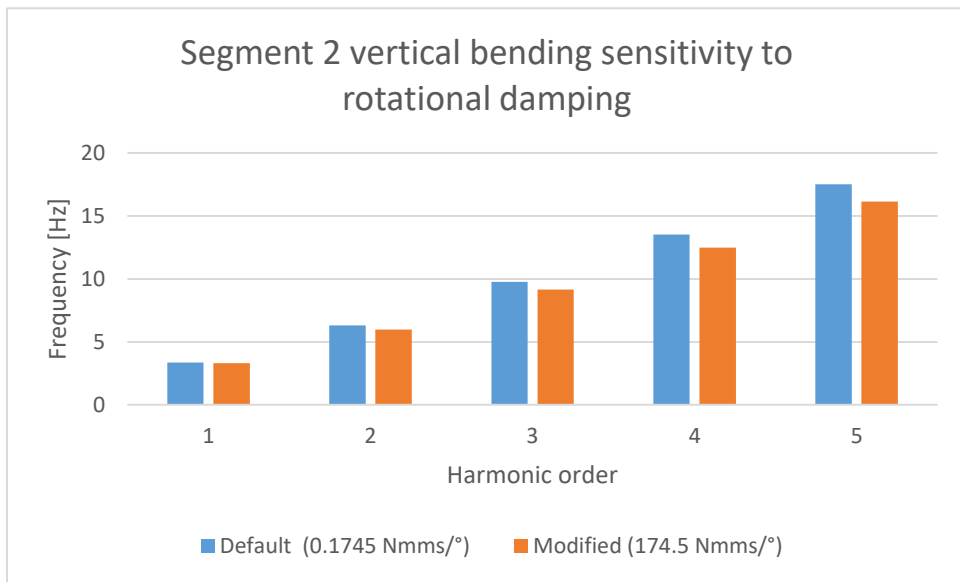


Figure 3.11. Segment 2 vertical bending sensitivity to rotational damping.

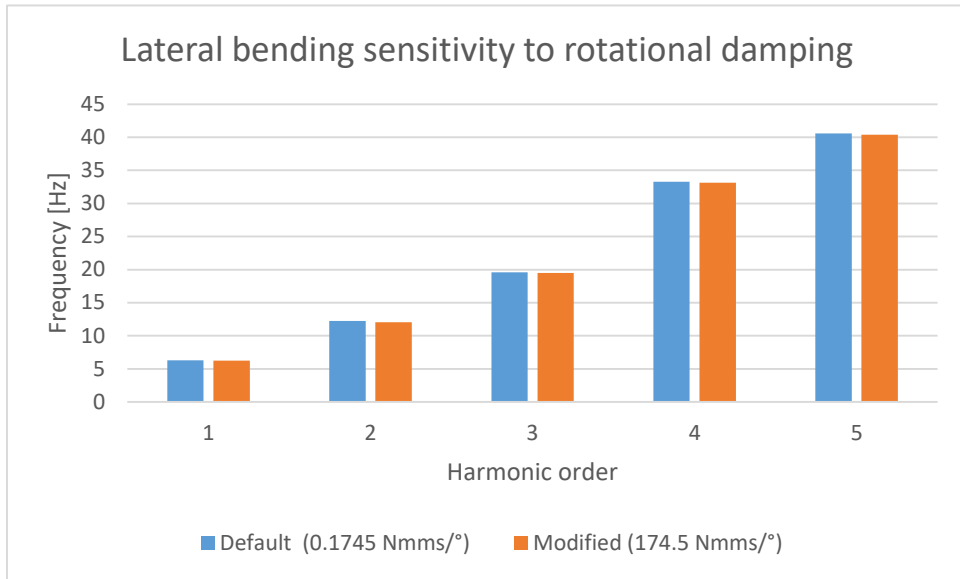


Figure 3.12. Lateral bending sensitivity to rotational damping.

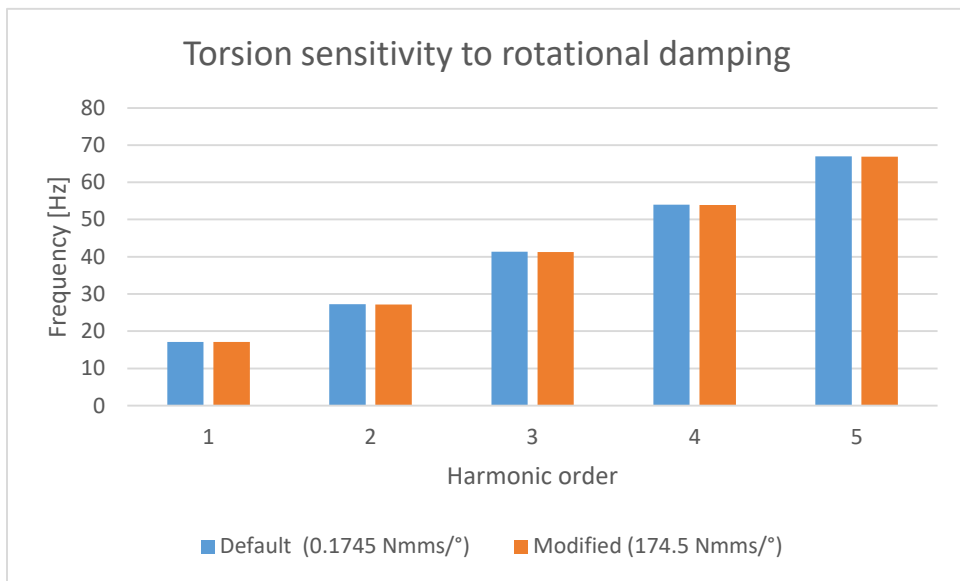


Figure 3.13. Torsion sensitivity to rotational damping.

Once again, there are virtually no differences for the lateral bending and torsion, as the modification does not play any role in their corresponding directions.

Notice however, that the frequencies are even lower than the first modification, even though only slightly. In this case, a big difference can be noticed in the damping ratio, which increases considerably. This was not true for the first modification, where in some instances they were even lower than the ones of the default model.

3.3 Unload angle modification.

The unload angle is the angle between two consecutive tracks, when zero torque is applied in their connection. The default ATV tank model has an unload angle of 12° . The modification brings this values to 0° , to see if the elimination of this angel has any influence in the behavior of the chain. The results, summarized in Table 3.5, show that there is virtually no distinction between the original and modified case.

String 1	f [Hz]	ζ [%]	String 1	f [Hz]	ζ [%]
1	2.53	5.26	1	2.51	5.87
2	4.27	1.56	2	4.22	1.23
3	6.58	3.12	3	6.51	2.53
4	8.74	2.78	4	8.66	1.98
5	11.1	3.18	5	11.01	2.15
String 2	f [Hz]	ζ [%]	String 2	f [Hz]	ζ [%]
1	3.37	10.73	1	3.41	13.59
2	6.32	1.51	2	6.22	1.45
3	9.76	1.49	3	9.59	1.7
4	13.53	1.25	4	13.3	1.92
5	17.51	0.69	5	17.27	1.41
Bending	f [Hz]	ζ [%]	Bending	f [Hz]	ζ [%]
1	6.31	12.17	1	6.29	12.16
2	12.22	19.35	2	12.11	19.37
3	19.6	14.42	3	19.55	14.43
4	33.3	12.41	4	33.17	12.59
5	40.6	16.45	5	40.44	16.42
Torsion	f [Hz]	ζ [%]	Torsion	f [Hz]	ζ [%]
1	17.13	6.45	1	17.12	6.48
2	27.22	2.61	2	27.14	2.61
3	41.33	4.65	3	41.24	4.69
4	54	4.19	4	53.88	4.14
5	67	4.39	5	66.84	4.41

Table 3.5. The left table shows the results of the original simulation (12°), whereas the right table shows the results with the modification (0°).

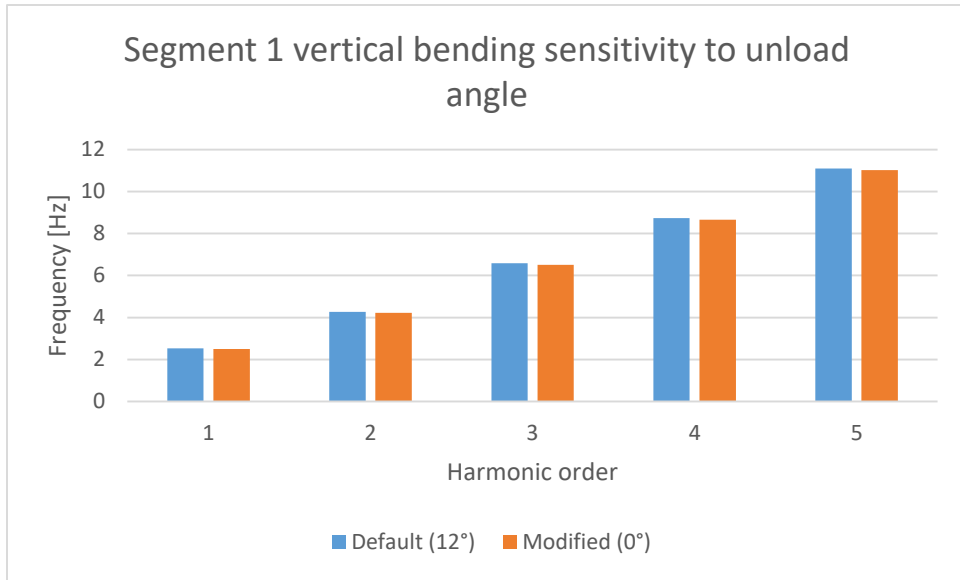


Figure 3.14. Segment 1 vertical bending sensitivity to unload angle.

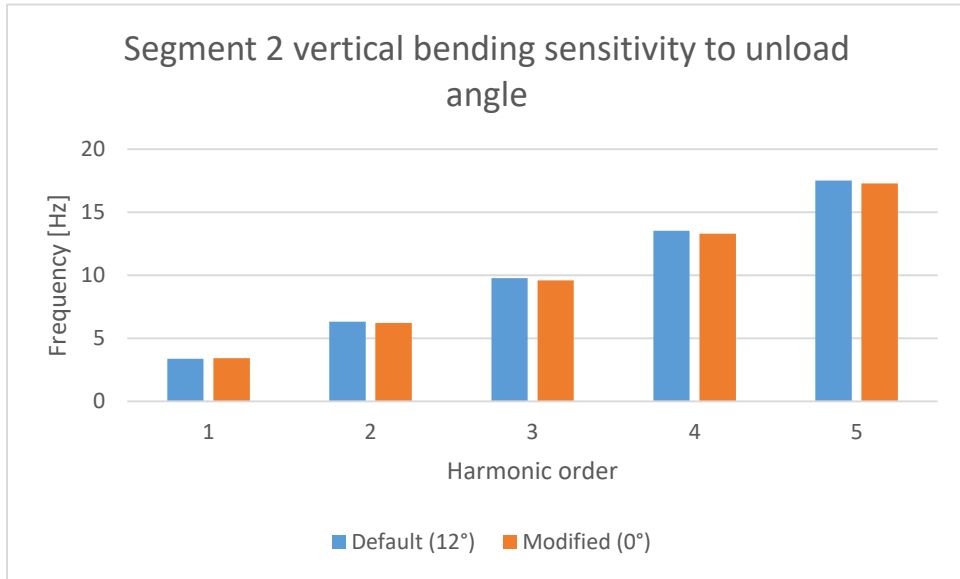


Figure 3.15. Segment 2 vertical bending sensitivity to unload angle.

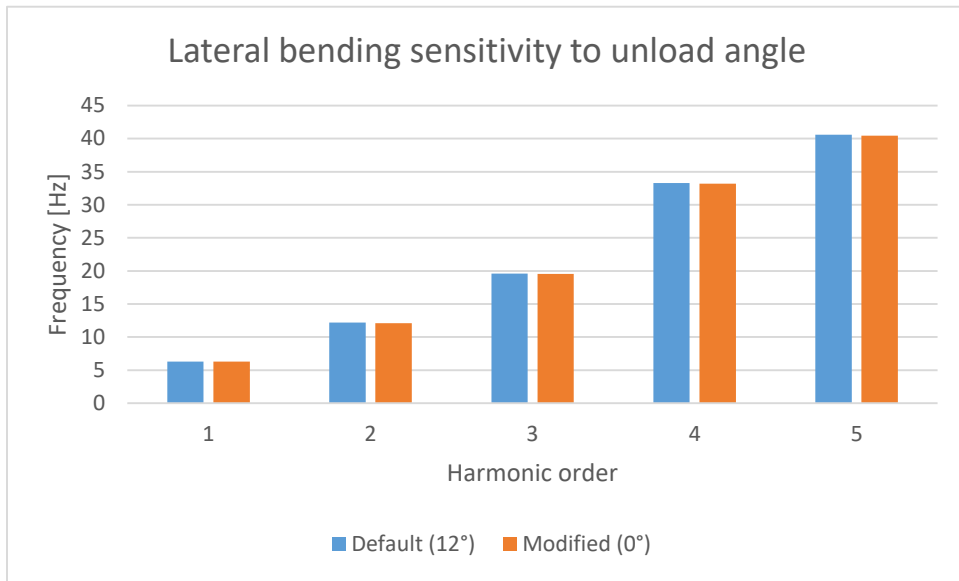


Figure 3.16. Lateral bending sensitivity to unload angle.

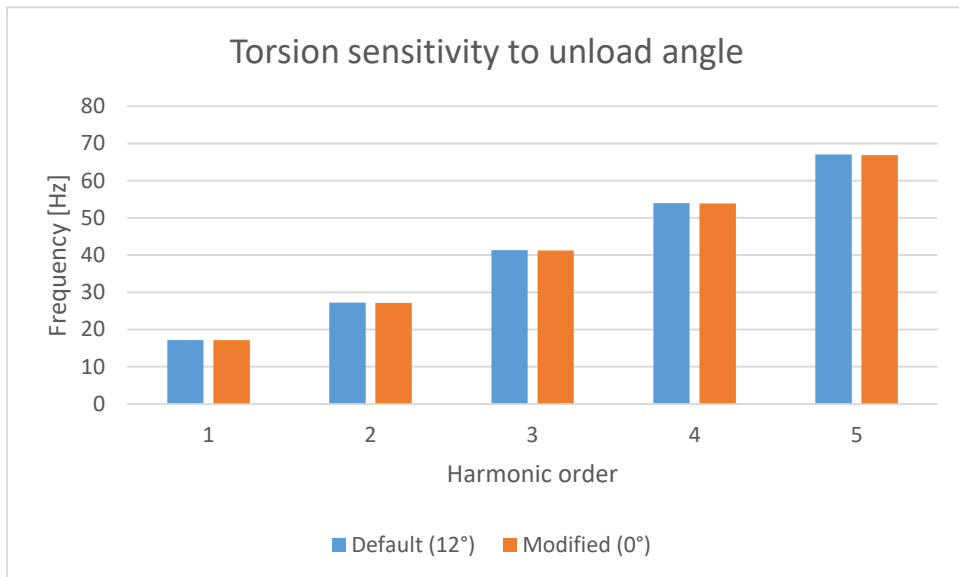


Figure 3.17. Torsion sensitivity to unload angle.

As can be seen from the table and graphs, decreasing the unload angle to 0°, has a very minor effect on the frequency, across the entire harmonics and the three different behaviors.

A similar modification can be made, but this time increasing the unload angle from 12°, which is the default value, to 24°.

String 1	f [Hz]	ζ [%]	String 1	f [Hz]	ζ [%]
1	2.53	5.26	1	2.55	6.62
2	4.27	1.56	2	4.27	1.58
3	6.58	3.12	3	6.56	3.27
4	8.74	2.78	4	8.75	2.77
5	11.1	3.18	5	11.11	3.17
String 2	f [Hz]	ζ [%]	String 2	f [Hz]	ζ [%]
1	3.37	10.73	1	3.41	15.33
2	6.32	1.51	2	6.32	9.65
3	9.76	1.49	3	9.76	14.86
4	13.53	1.25	4	13.53	17.31
5	17.51	0.69	5	17.5	12.69
Bending	f [Hz]	ζ [%]	Bending	f [Hz]	ζ [%]
1	6.31	12.17	1	6.31	12.13
2	12.22	19.35	2	12.14	19.36
3	19.6	14.42	3	19.58	14.36
4	33.3	12.41	4	33.21	12.55
5	40.6	16.45	5	40.47	16.38
Torsion	f [Hz]	ζ [%]	Torsion	f [Hz]	ζ [%]
1	17.13	6.45	1	17.11	6.49
2	27.22	2.61	2	27.15	2.59
3	41.33	4.65	3	41.25	4.67
4	54	4.19	4	53.89	4.12
5	67	4.39	5	66.85	4.39

Table 3.6. The left table shows the results of the original simulation (12°), whereas the right table shows the results with the modification (24°).

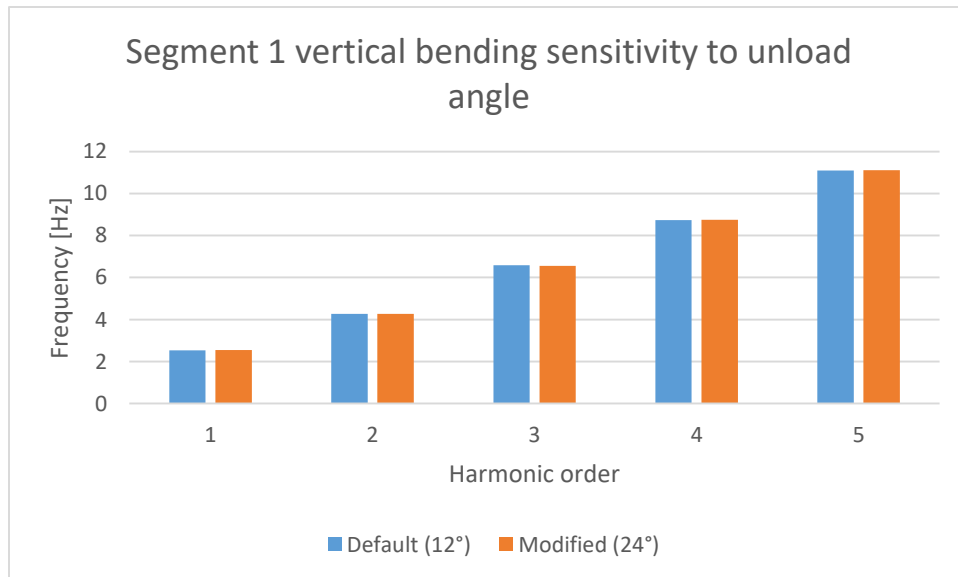


Figure 3.18. Segment 1 vertical bending sensitivity to unload angle.

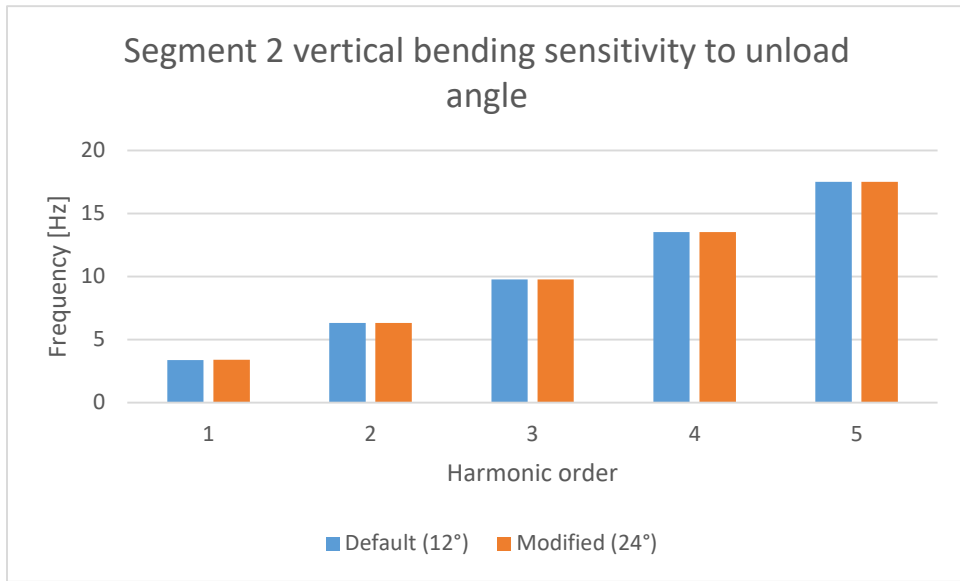


Figure 3.19. Segment 2 vertical bending sensitivity to unload angle.

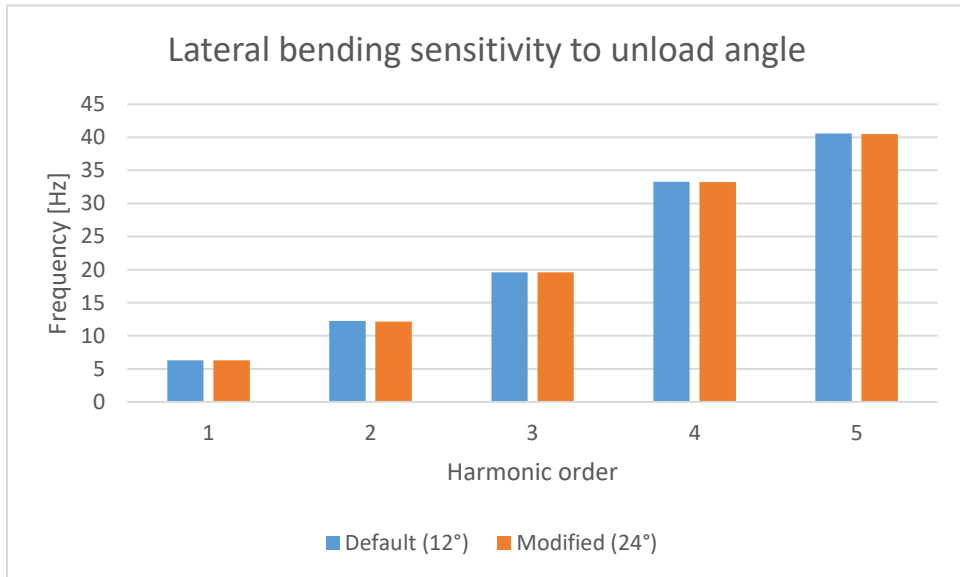


Figure 3.20. Lateral bending sensitivity to unload angle.

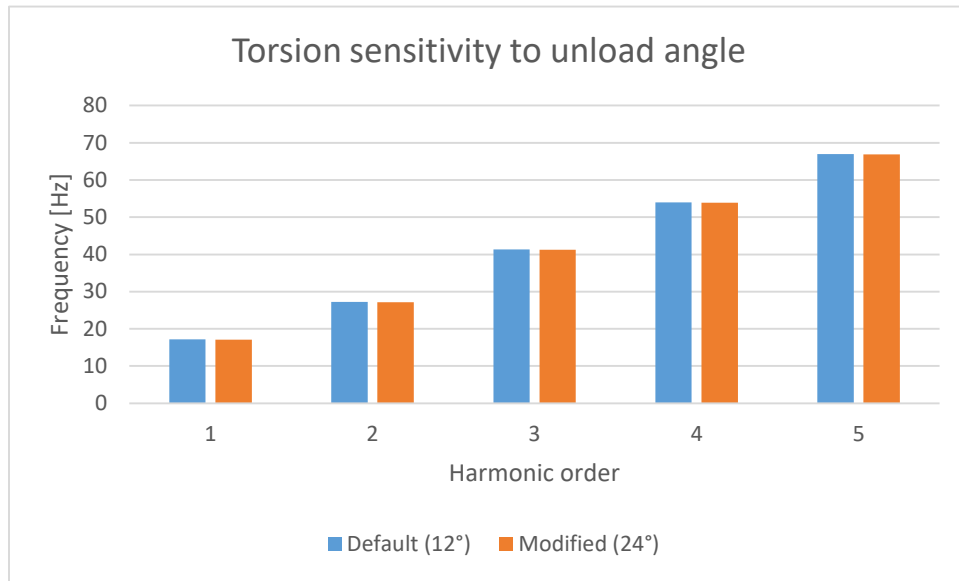


Figure 3.21. Torsion sensitivity to unload angle.

Once again, the modification of the unload angle does not appear to have a significant effect on the values of frequencies. The differences in frequency throughout the harmonics are not big enough to attribute them to the unload angle modification.

4 Modified tank model

In this section, a substantial modification is performed on the default tank model. This modification includes the addition of a second support roll, so as to have two supports on the upper part of the track chain, between the sprocket and the idle wheel, as depicted in Figure 4.1. Such modification is performed with the goal of verifying the analytical procedure developed for the default model and extending it to a more complex, but realistic situation.

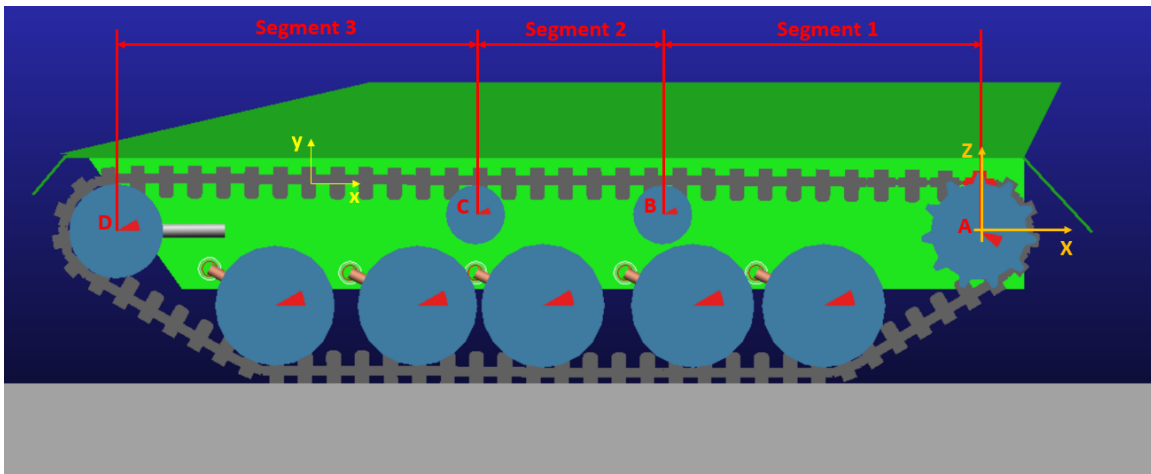


Figure 4.1. Modified tank model.

The following is a summary of the procedure adopted and results acquired for the default tank model, still valid also for the modified model:

- The upper part of the track chain can be considered as either a single segment (spanning from the sprocket to the idle wheel), or two independent segments (one spanning from the sprocket to the support roll and the other from the support roll to the idle wheel), depending on the behavior under study.
- Three types of behaviors were studied:
 - Bending in the longitudinal plane ((X-Z) plane). This behavior was modeled considering the chain as made of two segments, where each of them was modeled as either a string in tension or a multi DOF discrete system.
 - Bending in the lateral plane ((X-Y) plane). For this behavior, the chain was considered as a single segment, and it was modeled as a Euler-Bernoulli beam.
 - Torsion around the X-axis. The element used to describe this behavior was a shaft under torsional loading.

- By imposing the right boundary conditions, the natural frequencies were analytically obtained. These were then compared to the ones that were obtained from the ATV simulations with the goal of validating the analytical modeling.

The changes introduced by the addition of the new support roll are the following:

- A third segment has to be considered when modeling the upper part of the track chain.
- This third segment will definitely have an impact on the bending in the (X-Z) plane.
- The influence the new support roll will have on the other two behaviors has to be investigated, because its effect might be different than for the default model.

4.1 Geometrical data of the modified model.

Similar to what was done for the default model, some data related to the position of the components of interest are required, so as to obtain some parameters that will be later used in the calculation of natural frequencies. Table 4.1 contains the position of the different wheels and some properties for each of them. These will be useful in the subsequent calculations.

Part	x-position [mm]	y-position [mm]	z-position [mm]	Mass [kg]	Radius [mm]	Width [mm]
Sprocket wheel	0	-1270	0	50	255	480
Support wheel 1	1690	-1270	89	30	158	300
Support wheel 2	2690	-1270	89	30	158	300
Idle wheel	4610	-1270	1	50	250	355
Road wheel 1	3761	-1270	-396	35	320	355

Table 4.1. Geometrical data of the modified tank model.

In particular, the upper track chain, for the purposes of this analysis, will be considered as composed of three segments, as shown above in Figure 4.1. Table 4.2 summarizes some parameters for each of these segments.

Segment	Nr. segments [-]	Segment mass [-]	Length [mm]	Mass [kg]
Segment 1	11	15	1690	165
Segment 2	7	15	1000	105
Segment 3	13	15	1920	195

Table 4.2. Data for each of the three segment of the upper chain.

The linear density of the track can be calculated as for the default model:

$$\mu = \frac{m_{segment,1} + m_{segment,2} + m_{segment,3}}{l_{segment,1} + l_{segment,2} + l_{segment,3}} = \frac{n_1 \cdot m_{pad} + n_2 \cdot m_{pad} + n_3 \cdot m_{pad}}{l_{segment,1} + l_{segment,2} + l_{segment,3}}$$

- n_i : number of track pads on the i^{th} segment.
- $l_{segment,i}$: length of the i^{th} segment.

4.2 ATV simulation results.

The ATV allows visualizing the results of the static simulation through a window dedicated to the animation of the mode shapes. Mode shapes relevant for the upper part of the track chain can be categorized as follows:

- Vertical bending oscillations in the (X-Z) plane.
- Torsional oscillation around the X-axis.
- Lateral bending oscillations in the (X-Y) plane.

The mode shapes for the modified tank model are shown in the following figures. Note how the main difference compared to the default model is in the (X-Z) plane due to the addition of a third segment. The other two cases (lateral bending and torsion), at least visually, seem to be quite similar to the ones of the default model.

The naming of the modes will be done following the same approach as for the default tank model.

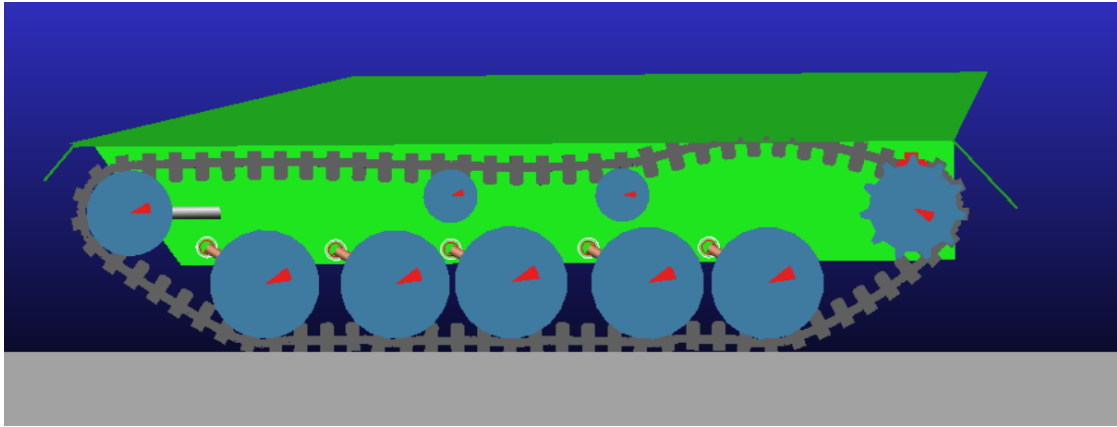


Figure 4.2. Segment 1 vertical bending first mode shape (3.76 Hz).

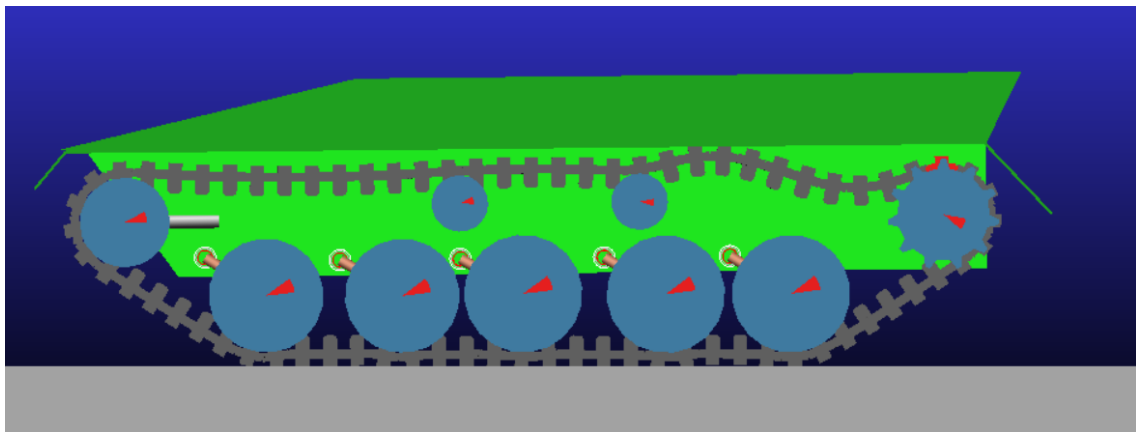


Figure 4.3. Segment 1 vertical bending second mode shape (7.07 Hz).

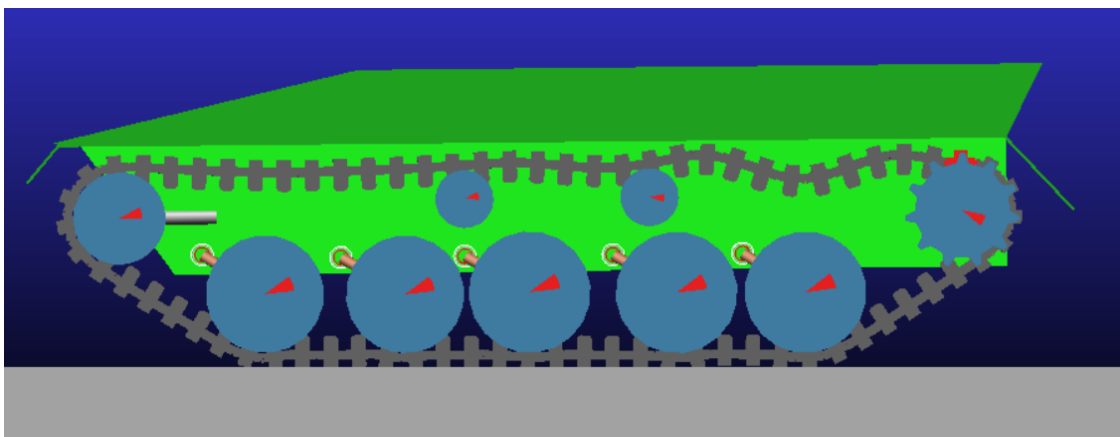


Figure 4.4. Segment 1 vertical bending third mode shape (10.82 Hz).

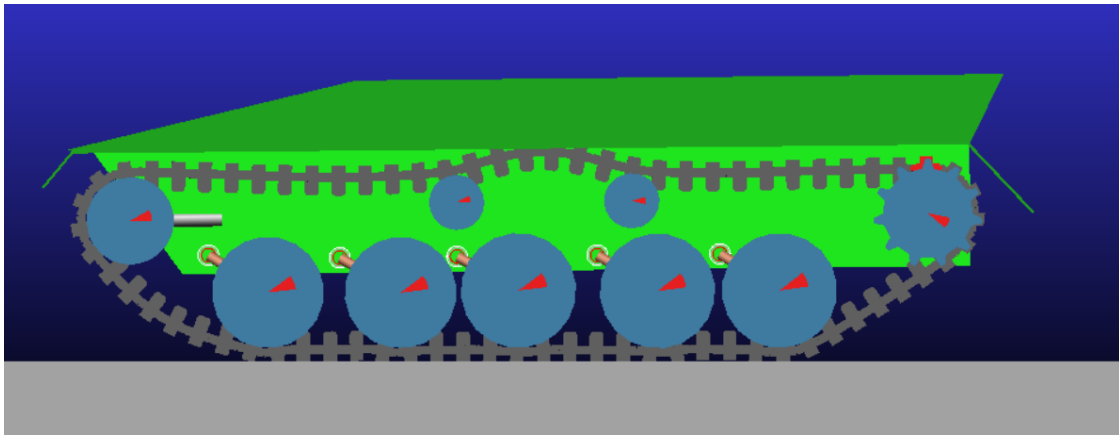


Figure 4.5. Segment 2 vertical bending first mode shape (5.69 Hz).

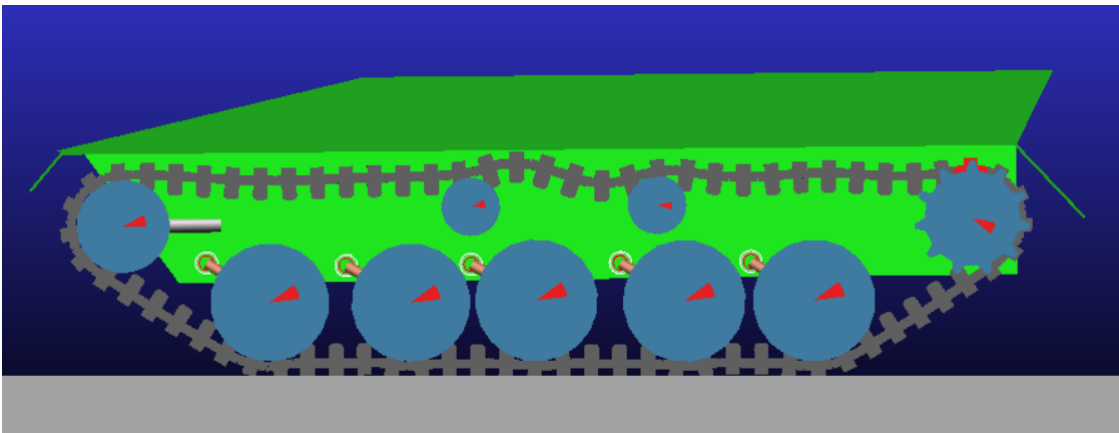


Figure 4.6. Segment 2 vertical bending second mode shape (11.84 Hz).

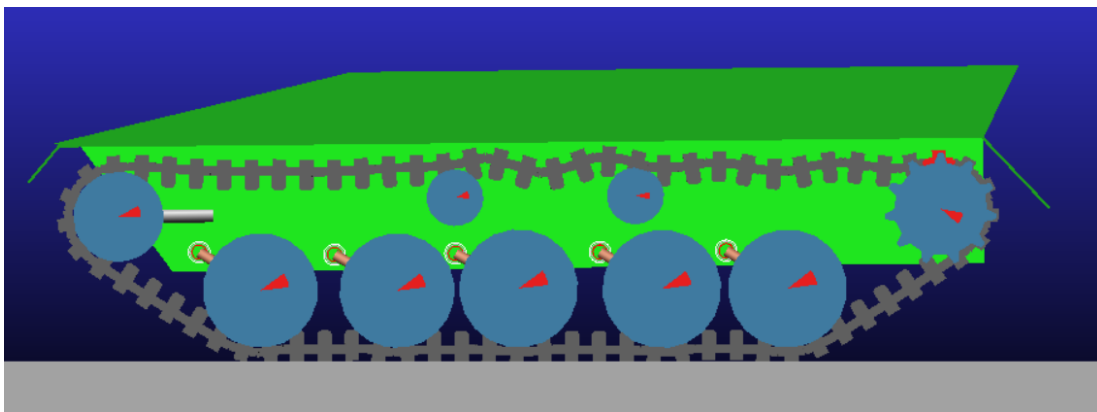


Figure 4.7. Segment 2 vertical bending third mode shape (18.42 Hz).

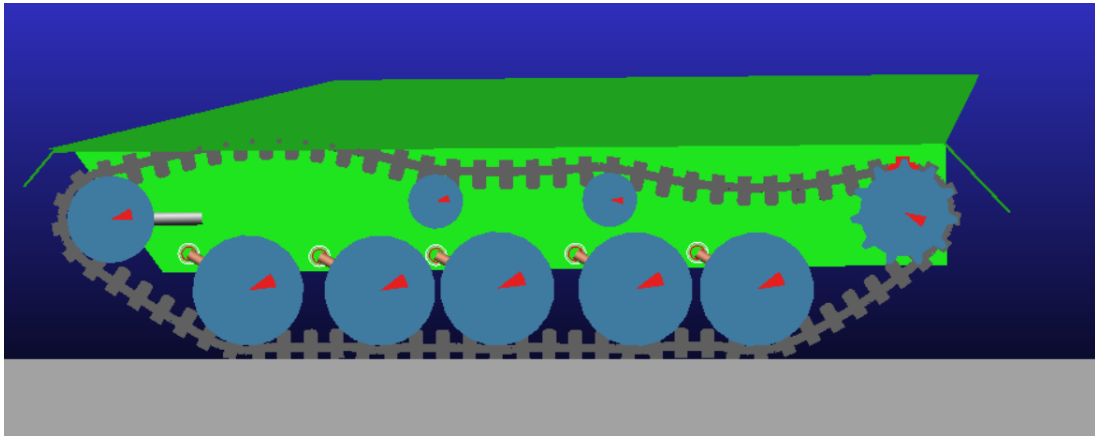


Figure 4.8. Segment 3 vertical bending first mode shape (3.19 Hz).

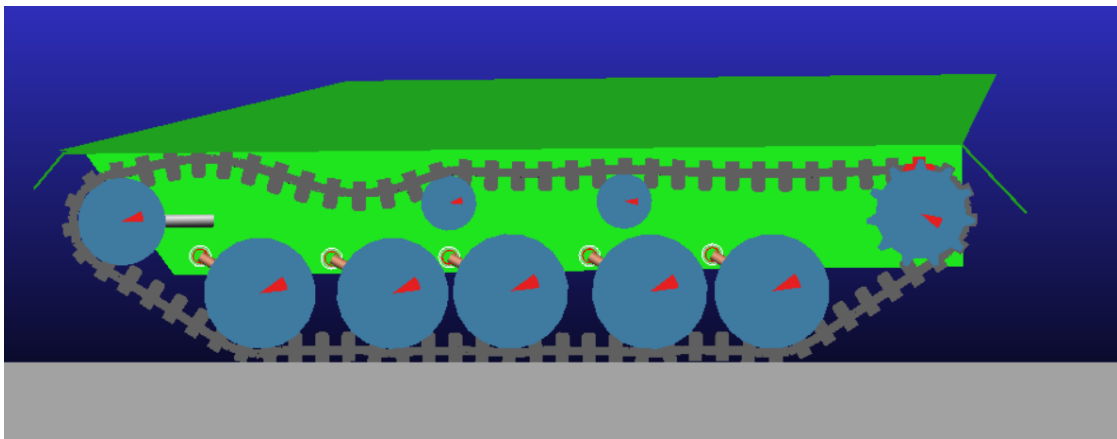


Figure 4.9. Segment 3 vertical bending second mode shape (6.13 Hz).

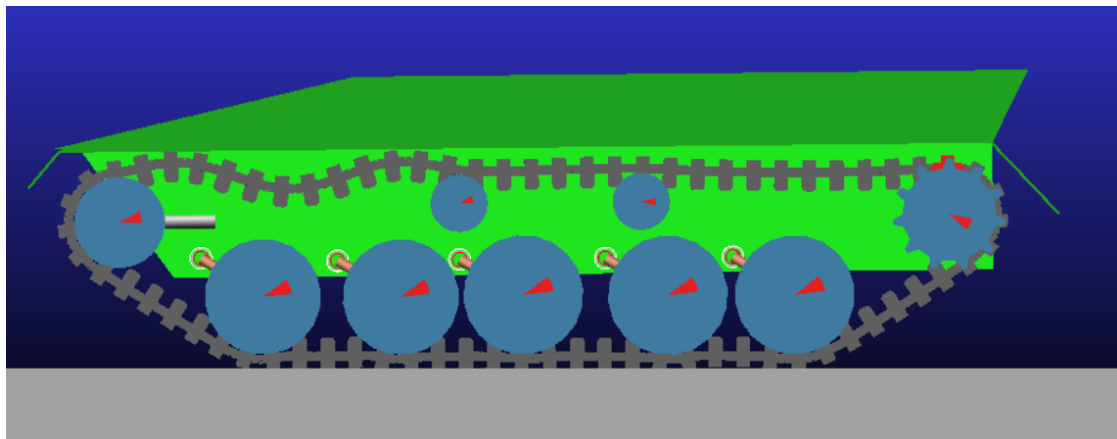


Figure 4.10. Segment 3 vertical bending third mode shape (9.39 Hz).

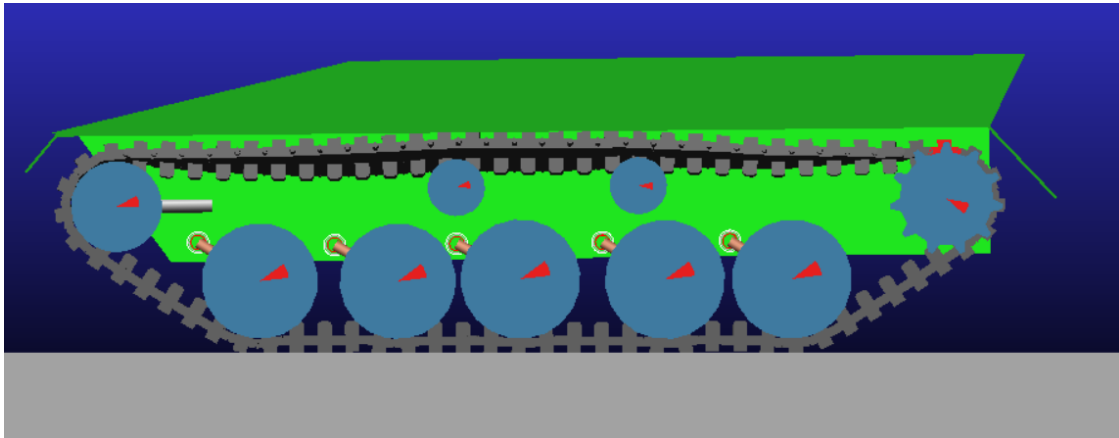


Figure 4.11. Chain torsion first mode shape (18.13 Hz).

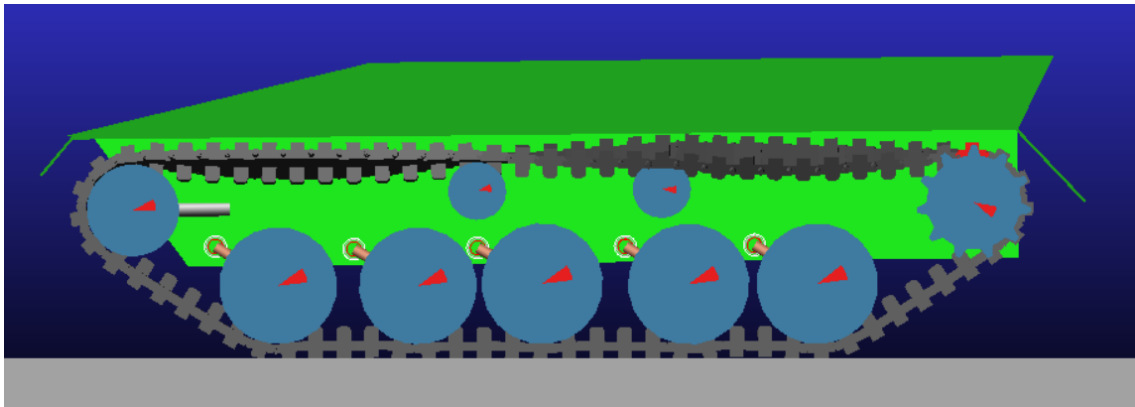


Figure 4.12. Chain torsion second mode shape (27.93 Hz).

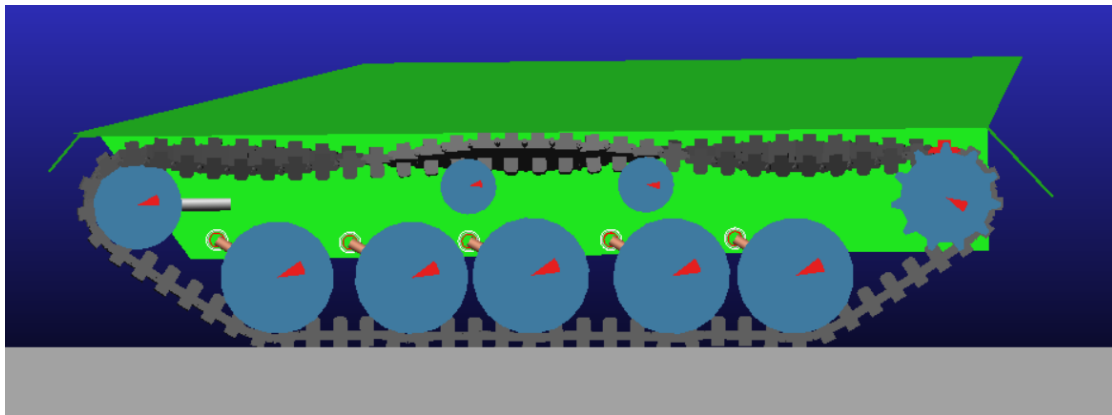


Figure 4.13. Chain torsion third mode shape (40.61 Hz).

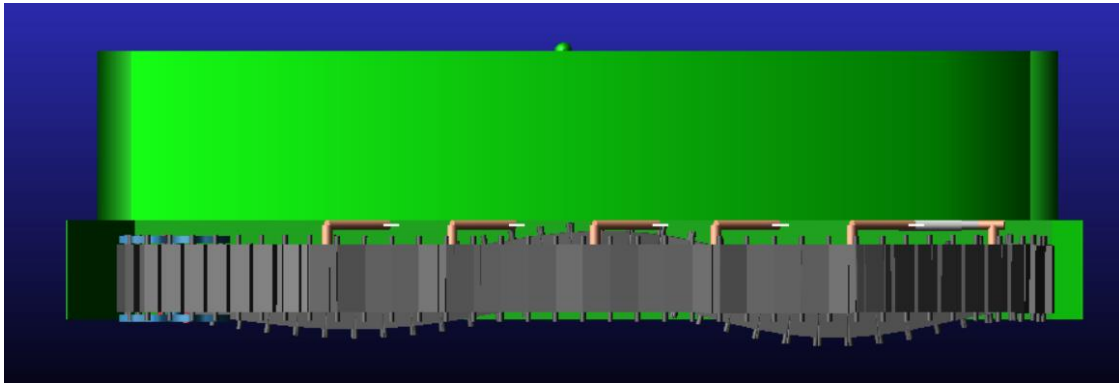


Figure 4.14. Chain lateral bending third mode shape (12.6 Hz).

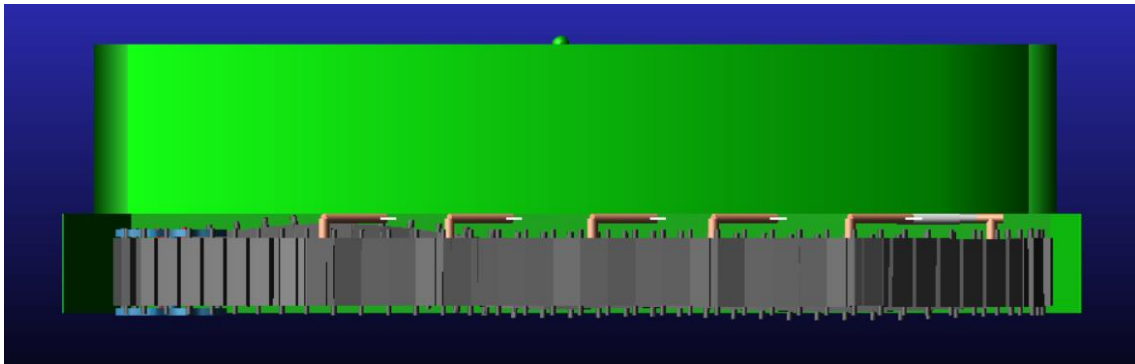


Figure 4.15. Chain lateral bending fourth mode shape (16.5 Hz).

The following tables show the results obtained for the three segments in vertical bending, the torsional oscillations of the chain and the lateral bending oscillations of the chain.

Segment 1		
Harmonic	f [Hz]	ζ [%]
1	3.76	6.61
2	7.07	1.06
3	10.82	1.14
4	15.01	2.35
5	19.8	1.31

Table 4.3. Simulation results for segment 1 vertical bending.

Segment 2		
Harmonic	f [Hz]	ζ [-]
1	5.69	0.45
2	11.84	0.71
3	18.42	0.27
4	26.5	1.07
5	36.33	0.29

Table 4.4. Simulation results for segment 2 vertical bending.

Segment 3		
Harmonic	f [Hz]	ζ [-]
1	3.19	3.35
2	6.13	0.41
3	9.39	0.61
4	12.77	0.53
5	16.42	0.54

Table 4.5. Simulation results for segment 3 vertical bending.

Bending		
Harmonic	f [Hz]	ζ [-]
3	12.6	22.96
4	16.5	32.41
5	31.53	14.9
6	42.61	17.84
7	55.48	16.13

Table 4.6. Chain lateral bending simulation results.

Torsion		
Harmonic	f [Hz]	ζ [-]
1	18.13	7.97
2	27.93	4.16
3	40.61	3.48
4	54.13	5.03
5	66.45	4.6

Table 4.7. Chain torsion simulation results.

4.3 Modeling the track chain vertical bending behavior.

This first analysis aims at modeling the vertical bending of the chain. The methods proposed here consider the chain as:

1. Two continuous strings in tension, separated by the support roll, and where the tension on the chain is calculated analytically.
2. Two continuous strings in tension, separated by the support roll, and where the tension on the chain is obtained from the ATV post-processing window.
3. Discretized system where each track pad is a rigid body connected to the others by means of elastic element (consistent with the multi-body approach).

4.3.1 Continuous string with analytically evaluated tension.

The analytical approach is based on the frequency calculation starting from the chain tension. The tension on the upper chain is not the one imposed by the idle wheel. Instead, this force is shared between the upper and the lower chain, so performing a force balance around the idle wheel, the analytical expression of the tension of the upper chain can be obtained. However, it is important to note that this tension does not take into account the gravity, friction in the idle wheel hub and other actions, so the value obtained from it can be quite different from reality.

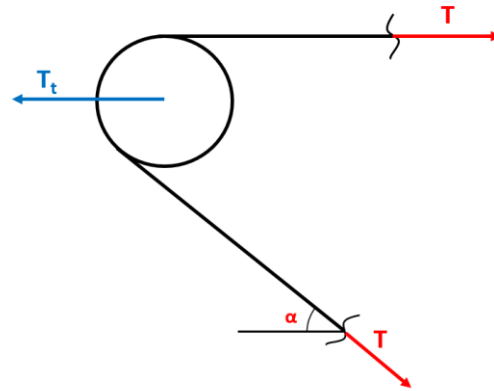


Figure 4.16. Force balance around the idle wheel.

Performing the horizontal equilibrium, the tension T on the upper chain is given by the following expression:

$$T = \frac{T_t}{1 + \cos \alpha}$$

The value of the angle α is calculated by using some geometrical relations between the tensioner and the first road wheel. Knowing it, we can evaluate the real (but theoretical) tension on the chain.

The simulations for the modified model will be performed at a tensioner value of 15000 N. Simulations at other tensioner values will not be reported here, as all the necessary remarks can be obtained from this simulation.

The wave equation for a continuous string in tension is as follows:

$$\frac{\partial^2 y}{\partial t^2} = \frac{T}{\mu} \frac{\partial^2 y}{\partial x^2}$$

Imposing the boundary conditions for a fixed-fixed string, allows obtaining the expression for the natural frequency:

$$f_i = \frac{i}{2L} \sqrt{\frac{T}{\mu}}$$

- f [Hz]: frequency of the i^{th} order harmonic.
- L [m]: length of the string of interest.
- T [N]: tension on the string.
- μ [kg/m]: linear density of the string.

Table 4.8 shows the results obtained by using the expression above for the natural frequency, where the tension is calculated starting from the idle wheel tension. The first five harmonics are reported for the three strings, as their frequency is in the relevant frequency range for tracked vehicles.

String	T_{idle}	T_{upper}	f1 [Hz]	f2 [Hz]	f3 [Hz]	f4 [Hz]	f5 [Hz]
String 1	15000	7936.51	2.62	5.25	7.87	10.50	13.12
String 2	15000	7936.51	4.44	8.87	13.31	17.74	22.18
String 3	15000	7936.51	2.31	4.62	6.93	9.24	11.55

Table 4.8. The first five harmonics for the three strings in tension (analytically evaluated tension).

4.3.2 Continuous string with ATV provided tension.

Creating track segment requests, allows obtaining the value of the horizontal force (force in the X-direction) that is exchanged between consecutive track segment links. This force can be considered as the tension on the equivalent string. An interesting observation is that each of the three segments (or strings) shows a different value of such force. Furthermore, this force is the same for all the track segment links that belong to the same string, meaning that the tension in each string is constant, but not equal among the strings.

Given that the boundary conditions are the same as the previous case, since the situation is exactly the same and only the value of the tension changes, we can use the same frequency expression. Table 4.9 shows the results obtained with the ATV tension for the first five simulations.

String	Tension idle [N]	Tension track [N]	f1 [Hz]	f2 [Hz]	f3 [Hz]	f4 [Hz]	f5 [Hz]
String 1	15000	11663	1.17	2.33	3.50	4.67	5.83
String 2	15000	11680	1.17	2.33	3.50	4.67	5.84
String 3	15000	11605	1.16	2.33	3.49	4.65	5.82

Table 4.9. The first five harmonics for the three segments, calculated with ATV tension values.

The graphs above point to a clear result. The analytical results are closer to the simulation results for greater lengths of string. This is clear due to the approximation being best for string 3, which is the longest, and worst for string 2, which is the shortest.

Furthermore, it can be said that the shorter the segment is, the more inaccurate would be to consider it as a string. Hence, string 2 demonstrates a behavior that indeed resembles the string, but for higher harmonics shows characteristics of a Timoshenko beam as well. This is due to the fact that, especially from the third harmonic, the trend is not exactly linear, but is something between a linear and parabolic trend.

This last remark shows a limitation of the string modeling procedure suggested in this thesis. Namely, the string approximation yields better results when the length is greater, due to the chain portion resembling a string more than a beam.

That said, the two sets of results are close enough so as for the analytical approach to be used as a means of calculating the frequencies for the preliminary design. This is especially true for the lower harmonics, which are the ones that are predominant in tracked vehicles.

4.4 Modeling the track chain torsional behavior.

The assumptions made to model the track chain torsional behavior are the same ones made when the default model was studied.

The equation that describes the wave equation of a shaft that undergoes torsional loading is the following:

$$\frac{\delta^2 \theta}{\delta t^2} = \frac{GJ}{I_l} \frac{\delta^2 \theta}{\delta x^2}$$

Starting from this expression, it is possible to identify the term that represents the wave propagation speed. Knowing the speed that the wave travels with and the length of the shaft through which this wave travels, we can calculate the ratio of this length with the speed, in order to get the expression of the natural frequency. Obviously, this is only partly correct and it serves only as a logical guide, because to get a precise value of the natural frequency, the boundary conditions of the shaft have to be imposed, allowing for the shape function to be defined.

$$c = \frac{GJ}{I_l} \left[\frac{\frac{N}{m^2} * m^4}{\frac{Nkg^2}{m}} = \frac{m}{s} \right]$$

The same modification as in the default model analysis is performed, with the goal of establishing a link between the chain, which is a lumped system and the shaft, which is a continuous system.

The following transformation is performed to get a different expression for the wave speed:

$$c^2 = \frac{GJ_p}{I_l} = \left[\frac{Pa * m^4}{kf * \frac{m^2}{m}} \right] = \left[m^2 \frac{\frac{Nm}{rad}}{kg * m^2} \right] = L^2 \frac{k_T}{I}$$

$$\Rightarrow c = L \sqrt{\frac{k_T}{nI}}$$

- G [MPa]: shear modulus of the material.
- J_p [m⁴]: polar moment of inertia of the cross-section.
- I_l [kg * m]: mass moment of inertia per unit length.
- L [m]: length of the chain portion under study.
- k_T [Nm/rad]: torsional stiffness.
- I [kg * m²]: mass moment of inertia.
- n : number of track segments.

The wave equation for a shaft in torsion can then be updated with the suggested modification.

$$\frac{\delta^2 \theta}{\delta t^2} = c^2 \frac{\delta^2 \theta}{\delta x^2} = \frac{GJ_p}{I_l} \frac{\delta^2 \theta}{\delta x^2} = L^2 \frac{k_T}{I} \frac{\delta^2 \theta}{\delta x^2}$$

Imposing the boundary conditions (clamped-clamped), allows obtaining the expression of natural frequency.

$$f_i = \frac{i}{2L} \sqrt{\frac{GJ_p}{I_l}} = \frac{i}{2} \sqrt{\frac{k_t}{nI}}$$

The formula for the natural frequency gives the following results for the first five torsional harmonics, as depicted in Table 4.10.

f1 [Hz]	f2 [Hz]	f3 [Hz]	f4 [Hz]	f5 [Hz]
13.37	26.75	40.12	53.50	66.87

Table 4.10. The first five harmonics for the shaft in torsion model.

Figure 4.17 shows a comparison between the results obtained analytically and those of the simulation.

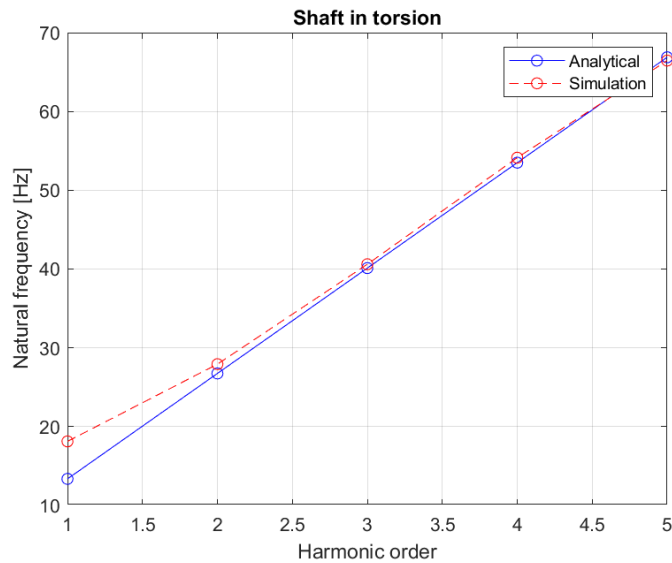


Figure 4.17. Graphical comparison of the analytical and simulation results for the torsional behavior.

As can be seen from the graph, the approximation for the torsion is so good, that for the higher harmonics the difference becomes nearly negligible. The results were the same also for the default model. This consistency in results for the torsional oscillations is due to the fact that the support wheel does not influence the torsional behavior, so adding one or more support wheels will not change the results.

4.5 Modeling the track chain lateral bending behavior.

The chain lateral bending is better approximated with a discrete multi DOF model, that considers each track pad as rigid and connected to the others by one linear and one torsional spring. The analysis on the default tank model already showed that this model is superior, so the Euler-Bernoulli beam model will not be included in what follows.

The procedure adopted for this model is identical to the one shown for the default tank model, with the only difference being the addition of a second lumped spring on track pad number 20, where the second support roll is located. For the schematic representation and FBD related to this case, refer to Figure 2.30 and Figure 2.32. In this case the equations of motion become:

EOM 1:

$$\begin{aligned}\uparrow) M\ddot{y}_1 + ky_1 - k\frac{l}{2}\theta_1 - ky_2 - k\frac{l}{2}\theta_2 &= 0 \\ \cup) I\ddot{\theta}_1 - k\frac{l}{2}y_1 + (k_t + \frac{kl^2}{4} + Tl)\theta_1 + k\frac{l}{2}y_2 - (k_t + \frac{kl^2}{4})\theta_2 &= 0\end{aligned}$$

EOM 31:

$$\begin{aligned}\uparrow) M\ddot{y}_{31} + ky_{31} + k\frac{l}{2}\theta_{31} - ky_{30} + k\frac{l}{2}\theta_{30} &= 0 \\ \cup) I\ddot{\theta}_{31} - k\frac{l}{2}y_{30} - (k_t + \frac{kl^2}{4})\theta_{30} + k\frac{l}{2}y_{31} + (k_t + \frac{kl^2}{4} + Tl)\theta_{31} &= 0\end{aligned}$$

EOM i:

$$\begin{aligned}\uparrow) M\ddot{y}_i - ky_{i-1} + 2ky_i - ky_{i+1} + k\frac{l}{2}\theta_{i-1} - k\frac{l}{2}\theta_{i+1} &= 0 \\ \cup) I\ddot{\theta}_i - k\frac{l}{2}y_{i-1} - (k_t + \frac{kl^2}{4})\theta_{i-1} + (2k_t + \frac{kl^2}{2} + Tl)\theta_i + k\frac{l}{2}y_{i+1} - (k_t + \frac{kl^2}{4})\theta_{i+1} &= 0\end{aligned}$$

EOM 14:

$$\begin{aligned}\uparrow) M\ddot{y}_{14} - ky_{13} + (2k + k_s)y_{14} - ky_{15} + k\frac{l}{2}\theta_{13} - k\frac{l}{2}\theta_{15} &= 0 \\ \cup) I\ddot{\theta}_{14} - k\frac{l}{2}y_{13} - (k_t + \frac{kl^2}{4})\theta_{13} + (2k_t + \frac{kl^2}{2} + Tl)\theta_{14} + k\frac{l}{2}y_{15} - (k_t + \frac{kl^2}{4})\theta_{15} &= 0\end{aligned}$$

EOM 20:

$$\begin{aligned}\uparrow) M\ddot{y}_{20} - ky_{19} + (2k + k_s)y_{20} - ky_{21} + k\frac{l}{2}\theta_{19} - k\frac{l}{2}\theta_{21} &= 0 \\ \cup) I\ddot{\theta}_{20} - k\frac{l}{2}y_{19} - (k_t + \frac{kl^2}{4})\theta_{19} + (2k_t + \frac{kl^2}{2} + Tl)\theta_{20} + k\frac{l}{2}y_{21} - (k_t + \frac{kl^2}{4})\theta_{21} &= 0\end{aligned}$$

The terms on these equations are collected in the mass and stiffness matrices as follows:

$$[M] = \begin{bmatrix} \begin{bmatrix} M_{i-1} & 0 \\ 0 & I_{i-1} \end{bmatrix} & 0 & 0 \\ 0 & \begin{bmatrix} M_i & 0 \\ 0 & I_i \end{bmatrix} & 0 \\ 0 & 0 & \begin{bmatrix} M_{i+1} & 0 \\ 0 & I_{i+1} \end{bmatrix} \end{bmatrix}$$

$$[K_i] = \begin{bmatrix} 2k & 0 \\ 0 & 2k_t + \frac{kl^2}{2} + Tl \end{bmatrix}$$

$$[K_{i-1}] = \begin{bmatrix} -k & \frac{kl}{2} \\ -\frac{kl}{2} & -k_t + \frac{kl^2}{4} \end{bmatrix}$$

$$[K_{i+1}] = \begin{bmatrix} -k & -\frac{kl}{2} \\ \frac{kl}{2} & -k_t + \frac{kl^2}{4} \end{bmatrix}$$

$$[K_1] = \begin{bmatrix} k & 0 \\ 0 & k_t + \frac{kl^2}{4} + Tl \end{bmatrix}$$

$$[K_{31}] = \begin{bmatrix} k & 0 \\ 0 & k_t + \frac{kl^2}{4} + Tl \end{bmatrix}$$

$$[K] = \begin{bmatrix} [K_1] & [K_{i+1}] & 0 & 0 & 0 \\ 0 & \ddots & 0 & 0 & 0 \\ 0 & [K_{i-1}] & [K_i] & [K_{i+1}] & 0 \\ 0 & 0 & 0 & \ddots & 0 \\ 0 & 0 & 0 & [K_{i-1}] & [K_{31}] \end{bmatrix}$$

These matrices are then implemented in MATLAB and the eigenvalue problem is solved, providing the eigenvalues and natural frequencies. Table 4.11 summarizes the results obtained from the discrete model, the continuous Euler-Bernoulli model which was not depicted here and the simulation.

Modified model lateral bending				
Continuous			Discrete	
Harmonic	Δf	$\Delta f/f$	Δf	$\Delta f/f$
3	15.48	123%	0.64	5%
4	33.42	203%	3.19	19%
5	46.47	147%	2.93	9%
6	69.71	164%	2.99	7%
7	97.4	176%	4.02	7%
8	129.46	184%	6.05	9%
9	169.15	202%	6.21	7%
10	214.01	218%	7.10	7%
11	264.78	235%	8.36	7%
12	323.15	256%	8.27	7%
13	387.02	276%	9.19	7%
14	458.65	300%	8.94	6%
15	536.9	325%	8.68	5%
16	621.63	351%	8.73	5%
17	714.56	382%	7.29	4%
18	813.29	412%	6.89	3%
19	918.4	442%	6.96	3%
20	1030.02	473%	7.40	3%

Table 4.11. Results summary for the modified tank model lateral bending.

Figure 4.18 shows a graphical comparison between the modeling approaches, where the quality of approximation offered by the discrete model can be appreciated.

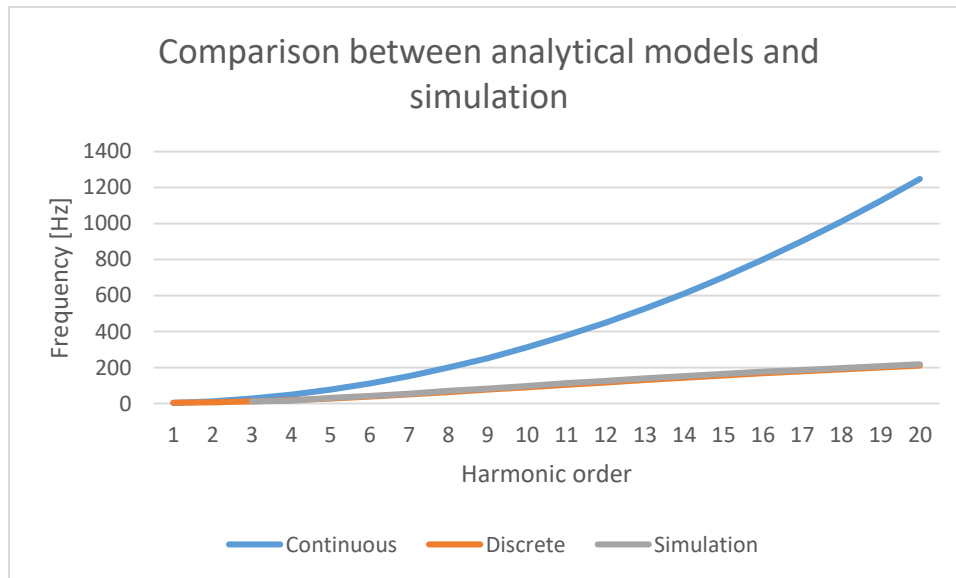


Figure 4.18. Graphical representation of the comparison between the analytical model results and simulation for chain lateral bending.

Another way to better appreciate the differences between the different analytical models proposed for the chain lateral bending is by comparing the error (both absolute and relative) that each model yields.

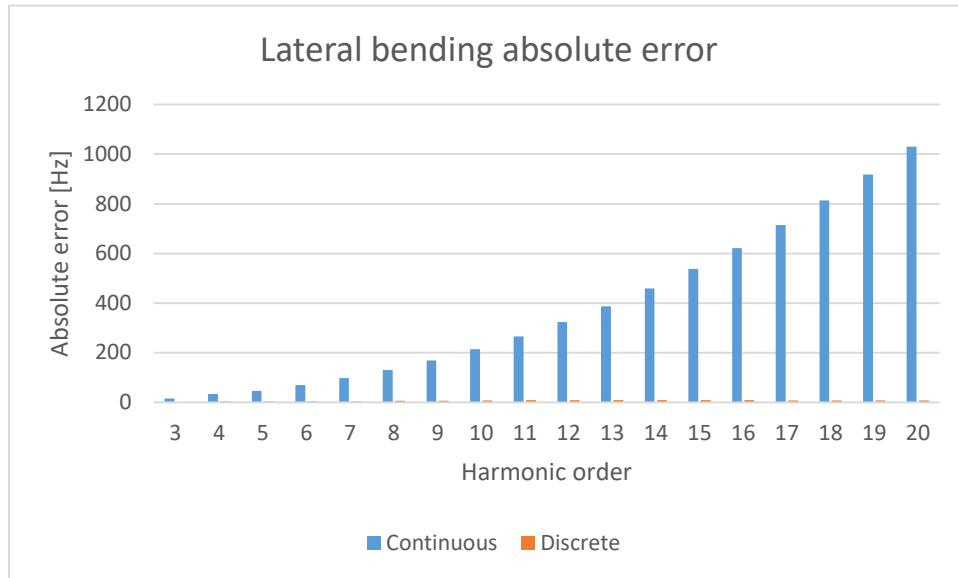


Figure 4.19. Lateral bending absolute error for the modified tank model.

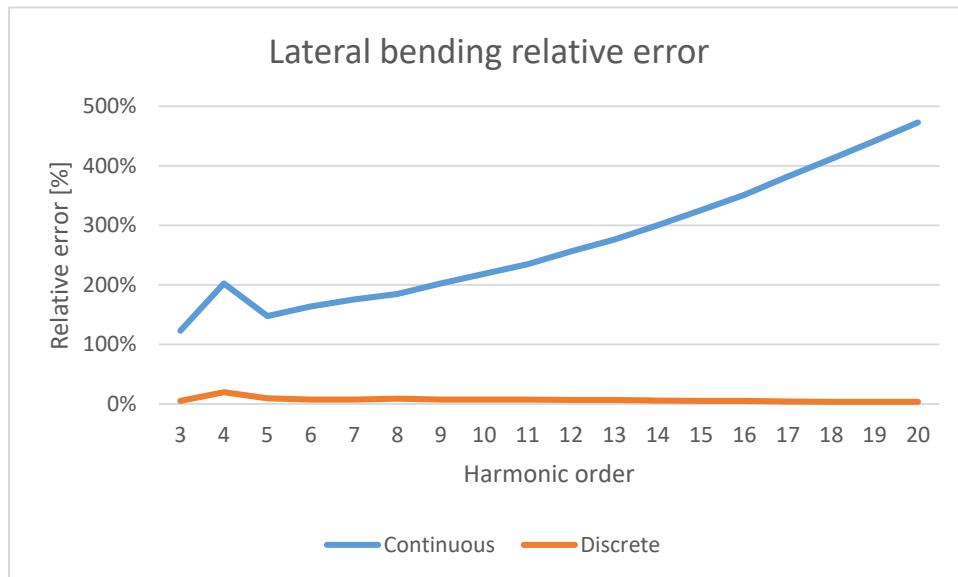


Figure 4.20. Lateral bending relative error for the modified tank model.

4.6 Summarizing the results for the modified tank model.

As was demonstrated on the analyses performed in these last sections, the results are consistent with those obtained for the default model. They can be summarized as:

- The vertical bending can be modeled considering the three segments as strings in tension. The important remark regarding this is that the real behavior lies between a string and a beam, in such a way that longer sections are better approximated as strings, whereas as the segment gets shorter, the behavior shifts more towards the beam. In this analysis, the behavior even for the shortest segment remains closer to the string, but as an empirical rule, the length of the segment should be at least five times that of the single track segment in order for the string hypothesis to hold.
- The torsional behavior is characterized by an independence on the presence of the support roll. This was observed on the analysis of the default model, and was confirmed by the modified model, because the results for the default and modified model are nearly identical. Once again, the torsional behavior was confirmed as the most suitable one to be approximated by a continuous element.
- The lateral bending ((X-Y) plane), as for the default model, can be successfully modeled considering a discretized multi DOF system, in a manner similar to the multi-body approach. The main difficulty when using this approach is in defining the mass and stiffness matrices, so some proficiency from the user in terms of dynamics of systems is required. Otherwise, this method is pretty straightforward to be implemented.

The discussion above serves to validate the modeling approach proposed in this thesis. The method proposed here can be implemented even in more complex tank models, making sure that the assumptions fit the situation and keeping in mind that the results of these models show a certain deviation from the real ones.

5 Vertical dynamics of the tracked vehicle

Vehicle vertical dynamics has the objective of tuning the vehicle's parameters, so as to improve the comfort or road holding of the vehicle. As a general rule, improving comfort requires limiting the vertical acceleration fluctuations of the sprung mass, while improving road holding requires limiting the vertical force fluctuations that rise as a consequence of the uneven road profile. These two aspects often contradict each other, so when tuning the parameters of the vehicle, one of the two should be sacrificed in favor of the other.

For conventional wheeled vehicles, vertical dynamics is studied by considering a half car model (which is known as a 4 DOF model), where the sprung and unsprung masses are modeled according to their inertial, elastic and damping properties. Such model is represented in the figure below (taken from the lecture on Vertical Dynamics of the Motor Vehicle Mechanics[6] course, held at Politecnico di Torino for the Mechanical Engineering MSc).

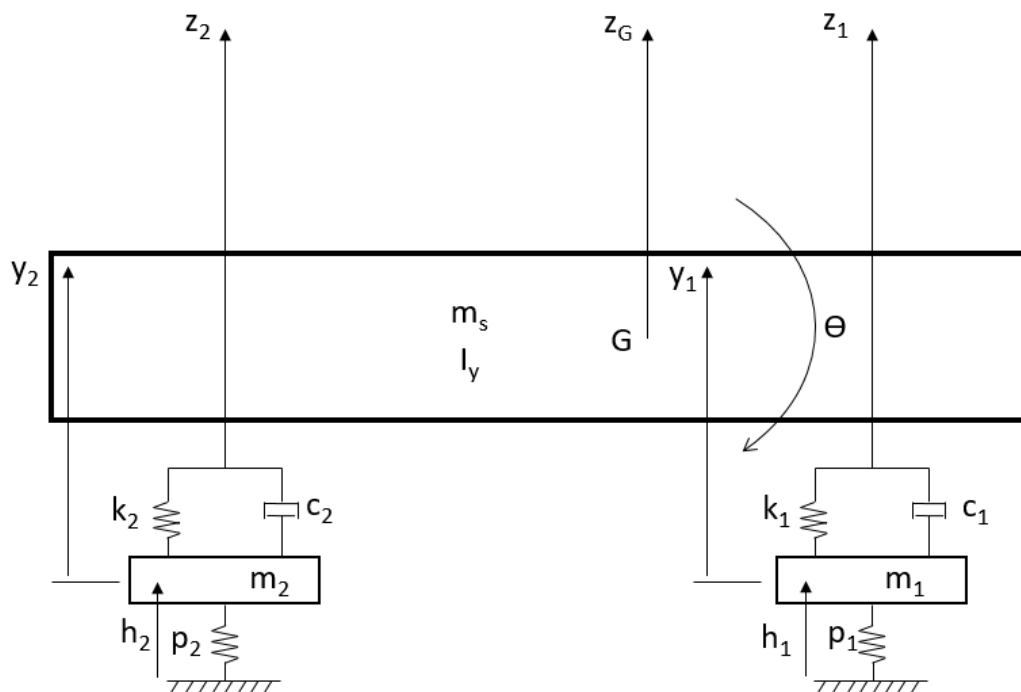


Figure 5.1. Schematic representation of the 4 DOF car model.

The system parameters that appear on half car model are the following:

- z_G : vertical translation of the center of gravity.
- θ : rotation of the sprung mass around the center of gravity.
- y_1, y_2 : vertical translation of the un-sprung masses.
- z_1, z_2 : vertical translation at the front and rear axles respectively.
- h_1, h_2 : input excitation from the road profile.
- m_s : sprung mass of the vehicle.
- I_y : sprung mass inertia.
- m_1, m_2 : front and rear un-sprung masses respectively.
- k_1, k_2 : front and rear suspension stiffness.
- c_1, c_2 : front and rear damping.
- p_1, p_2 : front and rear tires stiffness, expressed as equivalent springs having stiffness of one order of magnitude higher than the suspension springs.

The following figure represents a schematic of the default tank model with five road wheels, an idle wheel, a support roll and a sprocket. The red and blue arrows represent the restoring effects of the torsional springs and dampers. Note that the vertical translation of the road wheels is linked with the angle on the torsional springs and dampers through the connecting arm, so they do not represent two different coordinates, as one can be expressed through the other by some kinematic relationship.

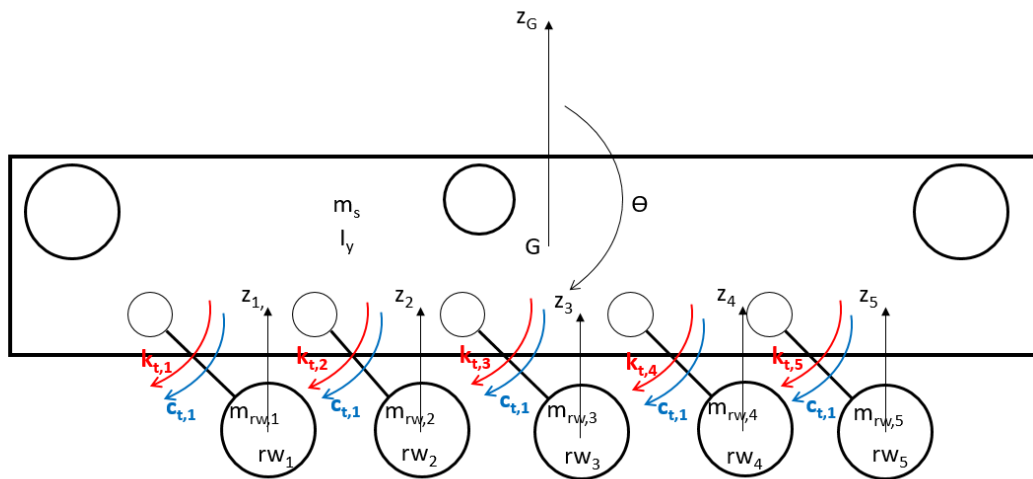


Figure 5.2. Default tank model schematic representation.

The parameters that appear in the half tank model are the following:

- z_G : vertical translation of the center of gravity.
- θ : rotation of the sprung mass around the center of gravity.
- z_i : road wheel's vertical translation.
- m_S : sprung mass of the tank.
- I_y : sprung mass inertia.
- m_{rW} : mass of the road wheel.
- $k_{t,i}$: torsional spring restoring effect.
- $c_{t,i}$: torsional damper restoring effect.

However, studying the vertical dynamics of the tracked vehicle using this model would not give accurate results, because the chain of the real tracked vehicle plays a major role. This is due to two reasons. The first one is that the chain has a certain stiffness, which is not represented and accounted for in the equivalent model. The second is related to the additional excitation that the chain imposes on the system due to the contact of the sprocket and chain, which is not regular and depends on the angular velocity of the sprocket, as well as the chain harmonics that were modeled in the previous sections. Furthermore, studying the model with this analytical approach poses many complexities from a computational point of view.

For this reason, the dynamics of the tracked vehicle will be studied using ATV to set the simulation and MATLAB to post-process the results. The steps that will be followed to do this include the setup of a dynamic simulation where the tank model will move along a certain road profile with a constant velocity. A general roadmap of the procedure is as follows:

- Setting the ATV simulation, where the default tank model will travel along a certain road profile, with a constant velocity.
- Analyzing this road profile in MATLAB, by generating its PSD.
- Analyzing the vertical acceleration of the tank's center of mass, by generating its PSD.
- Knowing the PSD of the road profile and of the vertical acceleration, the FRF of the tank's vertical acceleration can be computed.
- Parameters of the tank (tensioner force, rotational spring stiffness, rotational damping coefficient) can be modified and the response of the system under different conditions can be compared.

5.1 Generating the road profile.

The first step of the analysis consists of the choice of the road profile where the vehicle model will be studied. ATV provides a number of road profiles. The default tank model will be tested on the road profile called “ride_quality_3inch_measured”. The total length of the road is around 317.5 meters and the elevation changes from 0 to -2.34 meters. The maneuver will last for 40 seconds at a constant velocity of 2.5 m/s, so the vehicle is supposed to cover more or less 1/3 of the road profile. The slope of the road can be defined as:

$$i = \tan \alpha = \frac{\Delta \text{elevation}}{\text{length}} * 100\% = \frac{-2.34 - 0}{317.5} * 100\% \approx -0.74\%$$

- i : slope of the road profile.
- α : inclination of the road profile.
- $\Delta \text{elevation}$: change in elevation of the road profile.
- length : total length of the road profile.

The road files that are provided by ATV give a deterministic description of the road profile, namely they provide the elevation as a function of the mesh ($z(x, y)$). In this case, the road is symmetric with respect to the x-axis, so that the right and left tracks of the vehicle follow the same profile. The road file is implemented in MATLAB to generate and plot the mesh of the road. The following figure shows the road mesh as plotted in MATLAB.

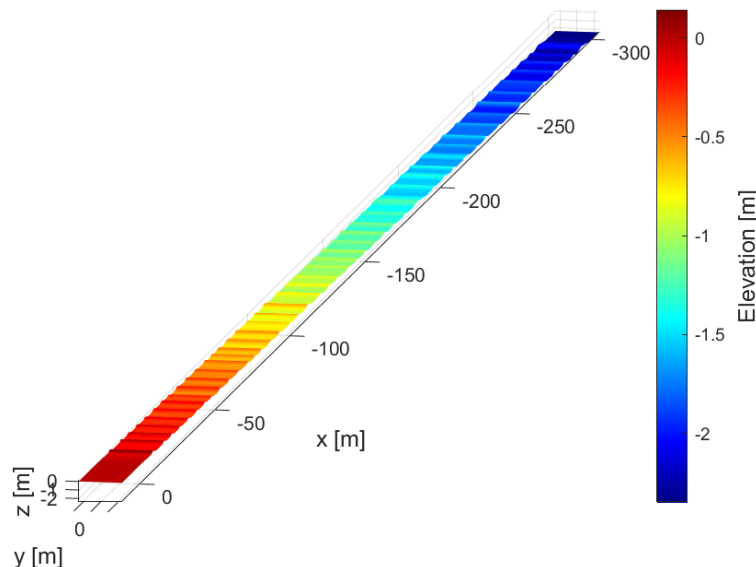


Figure 5.3. “ride_quality_3inch_measured” road profile.

The Power Spectral Density (PSD) of the road describes the frequency content of the road signal. To compute the PSD of the road profile, the Discrete Fourier Transform (DFT) of the elevation has to be computed. In MATLAB, this is done through the FFT (Fast Fourier Transform) function and the result is the amplitude spectrum of the road profile. The square of this amplitude is then divided by the length of the road to obtain its PSD. These steps are represented through the expressions below.

$$z = z(x, y)$$

$$Z(n) = FFT(z(x, y))$$

$$PSD(n) = \frac{|Z(n)|^2}{dn} \quad [m^3]$$

- $z = z(x, y)$ [m]: road profile.
- FFT : Fast Fourier Transform.
- $Z(n)$ [m]: amplitude spectrum of the road profile.
- $n \left[\frac{\text{cycles}}{m} \right]$: spatial frequency of the road profile.
- $dn \left[\frac{\text{cycles}}{m} \right]$: spatial frequency resolution.
- $PSD(n)$ [m^3]: spatial PSD of the road profile.

The PSD of the road profile in space domain is represented as in the following graph in logarithmic scale.

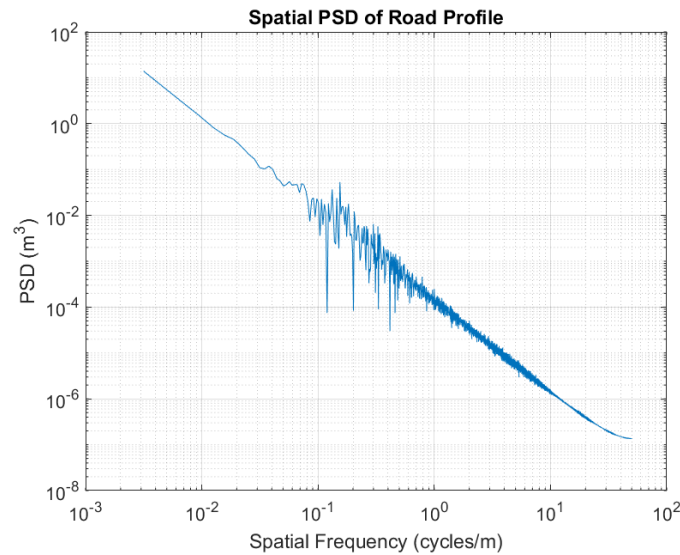


Figure 5.4. PSD of the road profile in space domain.

Having the spatial PSD of the road profile, it would be interesting to compare it with the reference road profiles defined in international standards by ISO 8608 [7].

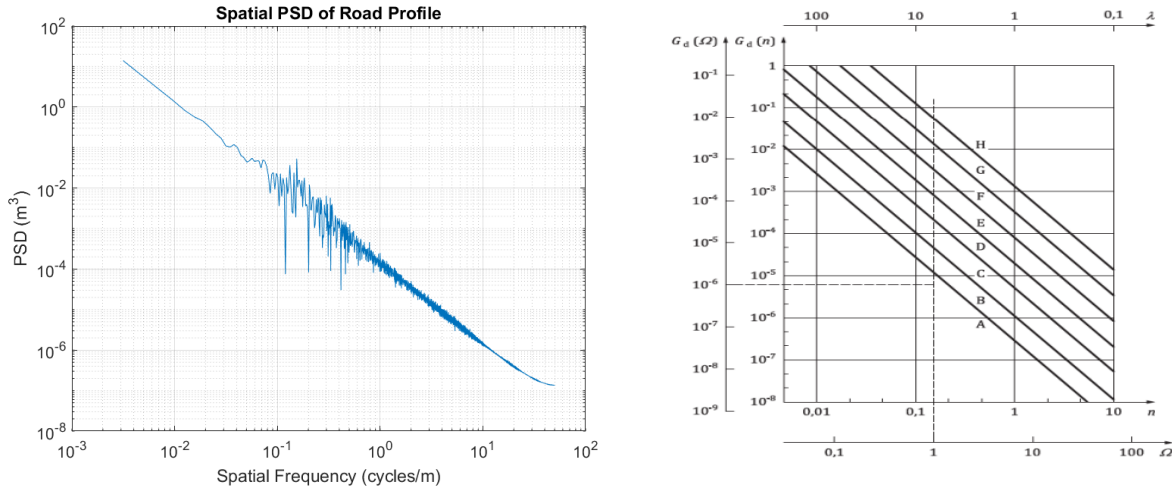


Figure 5.5. Left: spatial PSD of the road profile. Right: standard ISO road profiles [7].

By considering the following reference points in the plots, we can identify which standard line corresponds to our road profile:

- $10^0 \frac{\text{cycles}}{\text{m}} \rightarrow 10^{-4} \text{ m}^3$
- $10^1 \frac{\text{cycles}}{\text{m}} \rightarrow 10^{-6} \text{ m}^3$
- $10^{-2} \frac{\text{cycles}}{\text{m}} \rightarrow 10^0 \text{ m}^3$

Highlighting these points, it can be seen that the road profile that will be used corresponds to the standard road profile E, which is a very rough road (standards refer to it as “poor”) that would suit well the mission profile of such vehicle.

Once the PSD of the road profile in space domain has been computed, the PSD in time domain can be computed by dividing the spatial PSD and the vehicle speed. The result will be in $[\text{m}^2/\text{Hz}]$.

$$PSD(f) = \frac{PSD(n)}{V} \left[\frac{\text{m}^2}{\text{Hz}} \right]$$

Throughout the simulations the vehicle speed will be kept constant and equal to 2,5 m/s, as it suits better the road profile (the roughness of the road is such that higher speeds would induce loss of contact between the vehicle and ground). The temporal PSD of the road profile is shown in the figure below.

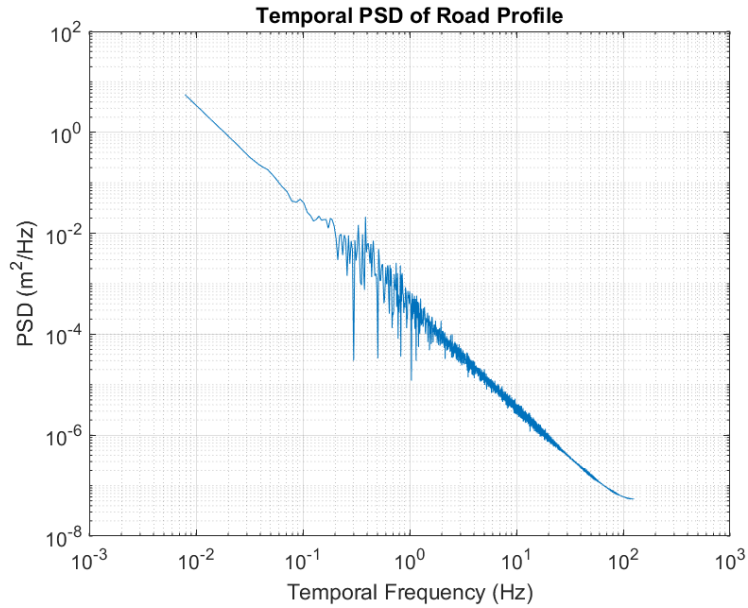


Figure 5.6. PSD of the road profile in time domain.

There is also an alternative method of obtaining the PSD, through a dedicated MATLAB function called “pwelch”, that uses the Welch’s method. The time domain PSD obtained with this method is shown in Figure 5.7.

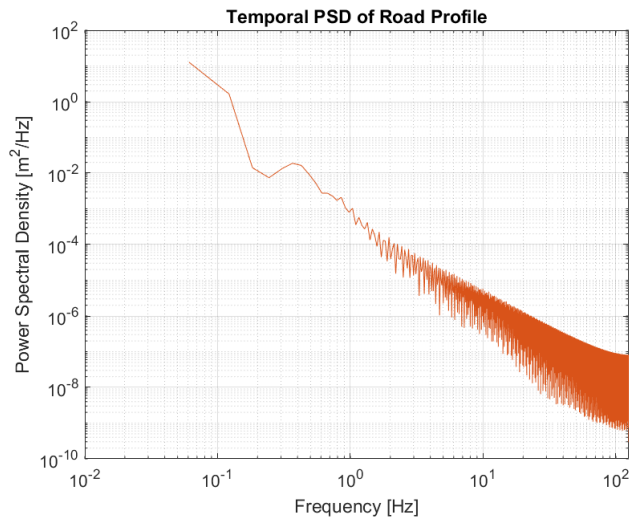


Figure 5.7. Temporal PSD of the road profile obtained with Welch's method.

Another method of understanding the frequency content of the road profile is the spectrogram, which in addition to the information already present in the PSD, provides also the frequency content evolution in space (normally the frequency evolution in time is given, but in this case the spatial frequency evolution in space is shown instead). The spectrogram of the road profile is shown in Figure 5.8.

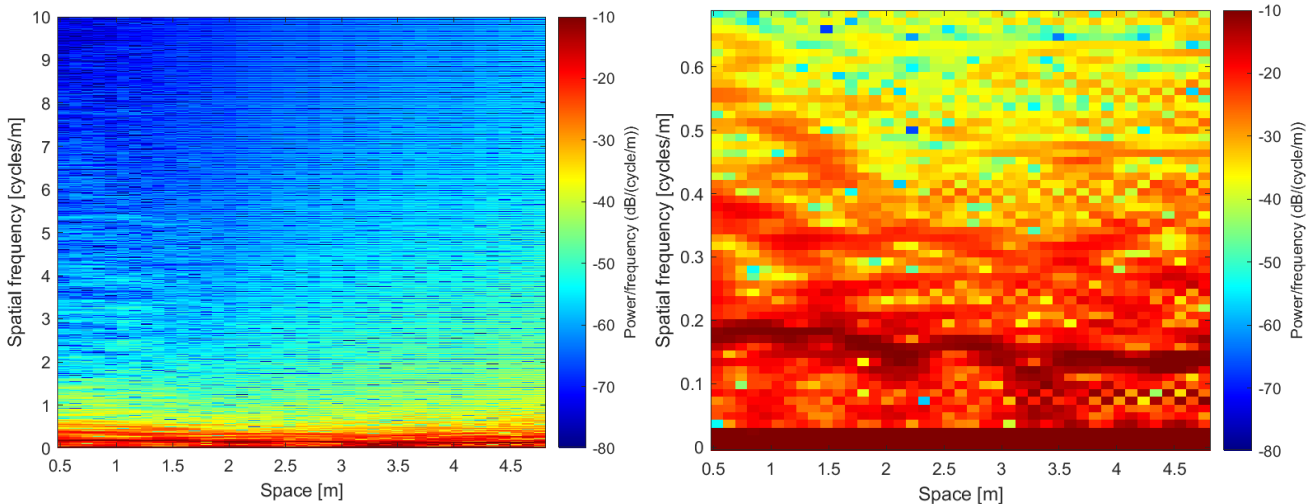


Figure 5.8. Left: spectrogram of the road profile in space domain. Right: Magnification of the low frequency range.

The spectrogram shows that the frequency has a peak at around 0,2 cycles/m. However, there is also a very strong frequency content at the lowest frequency range, that is shown in brown color at the bottom of the right image of Figure 5.8. A guess is that this low frequency is due to the linear downward trend of the road signal. In order to correctly estimate the frequency content of the road, this linear trend of the road should be removed. In MATLAB, this can be done through the “detrend” function. The original signal and the one where the trend is removed are shown in Figure 5.9.

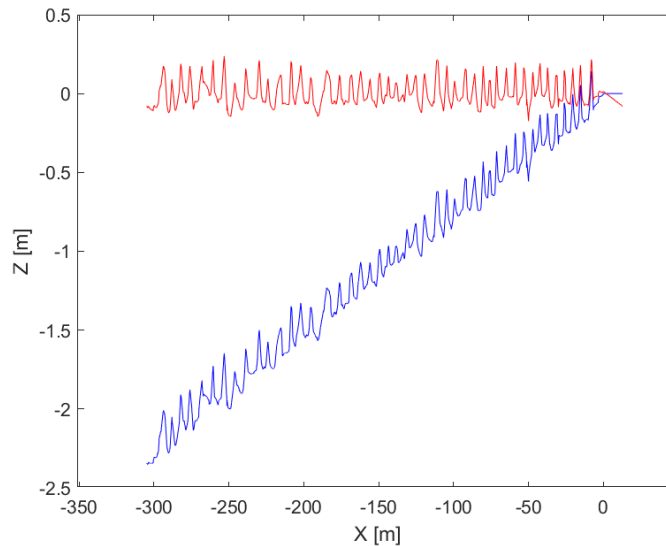


Figure 5.9. The blue line shows the original road signal. The red line shows the road signal with the trend removed.

Removing the linear trend from the signal, removes the low frequency and this can be clearly noted in the following figure, that show a magnification on the spectrogram.

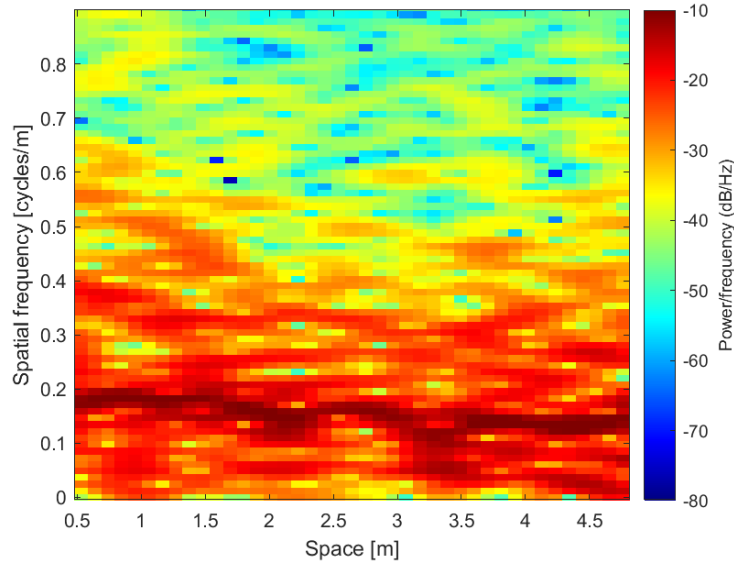


Figure 5.10. Spectrogram of the "detrended" signal.

Additionally, with the linear trend removed, there is an almost perfect match between the spatial PSD and the spectrogram, that is highlighted in Figure 5.11.

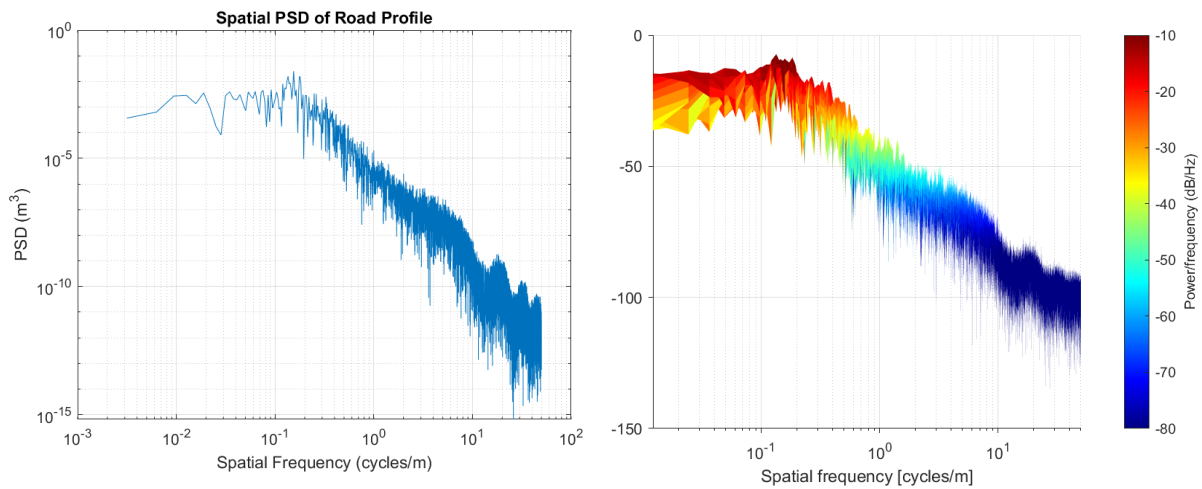


Figure 5.11. Matching between the road PSD and spectrogram.

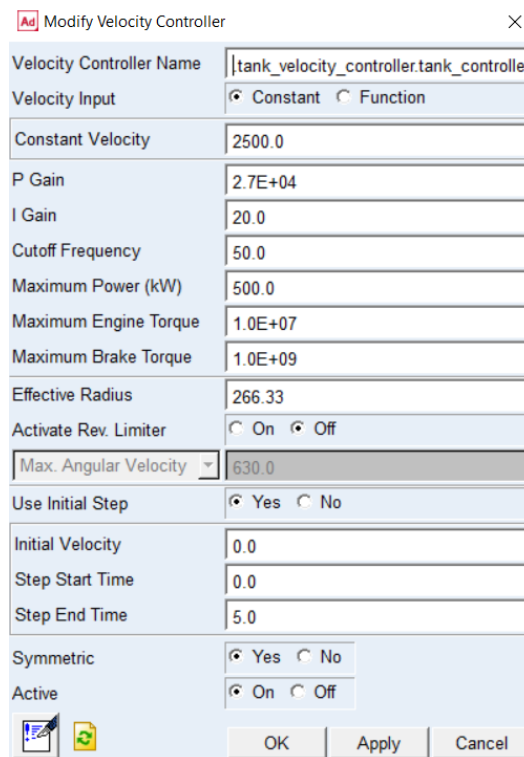
A possible explanation for this low frequency content might be that the road profile under study is in fact a portion of a greater sinusoidal profile, that has a high amplitude and a very long wavelength compared to the length of the road profile. For this reason, the road appears to be linear.

Having obtained the PSD of the road profile, the next step is obtaining the PSD of the vehicle. This will be done in the following section, where the vehicle parameters will be tuned to study how their change influences the response of the vehicle.

5.2 Setting the simulation.

Simulations will be performed using the ATV default tank model, in which the “tank_controller_powertrain” subsystem has been added. This subsystem includes a PID controller, which ensures that the desired speed is maintained throughout the maneuver.

It was decided that the simulations will be performed at a forward velocity of 2.5 m/s, which allows the track chain to maintain contact with the ground at all times. If contact is lost between the tracks and the ground, the simulation fails (this was the case with higher tank velocities). The following figure shows the parameters that the velocity controller requires.



Parameter	Value
Velocity Controller Name	tank_velocity_controller.tank_controller
Velocity Input	<input checked="" type="radio"/> Constant <input type="radio"/> Function
Constant Velocity	2500.0
P Gain	2.7E+04
I Gain	20.0
Cutoff Frequency	50.0
Maximum Power (kW)	500.0
Maximum Engine Torque	1.0E+07
Maximum Brake Torque	1.0E+09
Effective Radius	266.33
Activate Rev. Limiter	<input type="radio"/> On <input checked="" type="radio"/> Off
Max. Angular Velocity	630.0
Use Initial Step	<input checked="" type="radio"/> Yes <input type="radio"/> No
Initial Velocity	0.0
Step Start Time	0.0
Step End Time	5.0
Symmetric	<input checked="" type="radio"/> Yes <input type="radio"/> No
Active	<input checked="" type="radio"/> On <input type="radio"/> Off

Figure 5.12. Velocity controller dialog window.

The parameters that should be imposed are:

- Constant velocity: 2500 mm/s
- Initial velocity: $0.0 \frac{mm}{s}$
- Step start time: 0.0 s
- Step end time: 5.0 s

The other parameters are the default ones. Notice that also the initial velocity is set to zero and the vehicle is accelerated to the constant velocity in 5 seconds.

The “ride_quality_3inch_measured” road profile has to be loaded in the model. It must be taken care to locate the road correctly with respect to the vehicle. The initial section of the road is flat, so the vehicle should be placed in this section. The location of the road is done as shown in Figure 5.13. Furthermore, this way of locating the vehicle in the road enables the constant speed to be obtained before the rough section starts, so there is no acceleration in the section that we are interested in. As for the soil, dry asphalt is chosen.

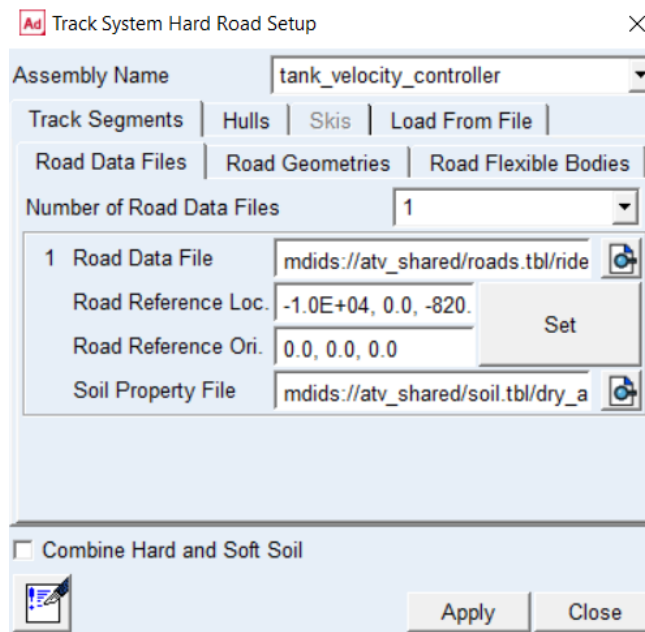


Figure 5.13. Road profile generation.

In addition to the dynamic simulation, modal analyses will be performed. One will take place at the beginning of the maneuver (at 0 seconds), while the other at the end of the maneuver (at 40 seconds). The additional steps required for the modal analyses will be performed in a manner similar to the one used for the track chain modeling, setting 15000 N as tensioner force. We believe the chain excitation has a contribution in the system’s vertical dynamics, and to check this assumption the modal analysis is required.

Having established the road profile that will be used and the velocity with which the test will be carried out, the parameters that will be tuned should be decided. The following is a list of the parameters that will be varied in the next sections:

- Tensioner force.
- Rotational spring stiffness.
- Rotational damper damping coefficient.

5.3 Simulation results.

The results of the simulation will be post-processed in MATLAB, by converting the “.res” files, as saved by ATV, to “.mat” files, using a script that performs the file conversion. This script is able to convert all the results of the simulation. However, it performs an error when converting the vertical acceleration of the center of gravity. This can be noticed when this acceleration, plotted in MATLAB, is compared to the same acceleration visualized in the ATV post-processing window and the two are completely different. For this reason, the acceleration in MATLAB will be obtained by dividing the z-direction component of the velocity of the center of gravity by the time step. The plot of acceleration in time is shown in Figure 5.14.

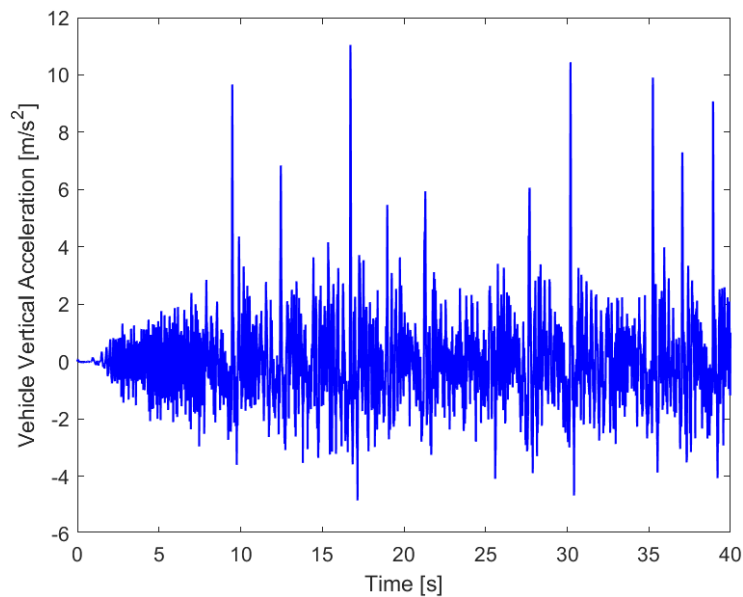


Figure 5.14. Sprung mass vertical acceleration in time.

The frequency content of the acceleration can be visualized by performing a DFT, to obtain the PSD of the acceleration signal. This can be done in MATLAB by either using the “fft” function, or “pwelch”, as was shown for the road profile PSD generation. In this case, “pwelch” was used. The parameters used as input for “pwelch” are shown in the figure below.

```

f_s = 1/(time(6) - time(5)); % Sampling frequency (Hz)
N = length(acc_z_raw); % Number of samples

t_win = 10;
window_size = t_win*f_s; % Number of samples per segment
noverlap = round(window_size*0.9); % Overlapping samples (90% of window size)

figure;
[Pxx_acc,F_acc] = pwelch(acc_z_raw,window_size, noverlap, [],f_s,'onesided');
loglog(F_acc,Pxx_acc);
xlabel('Frequency [Hz]');
grid on;
xlim([-0.1 10])
ylabel('Power Spectral Density ((m/s^2)^2/Hz)');
title('PSD of Vehicle Vertical Acceleration');

```

Figure 5.15. The script used to obtain the acceleration PSD.

The PSD of the vertical acceleration of the center of gravity is shown in Figure 5.16.

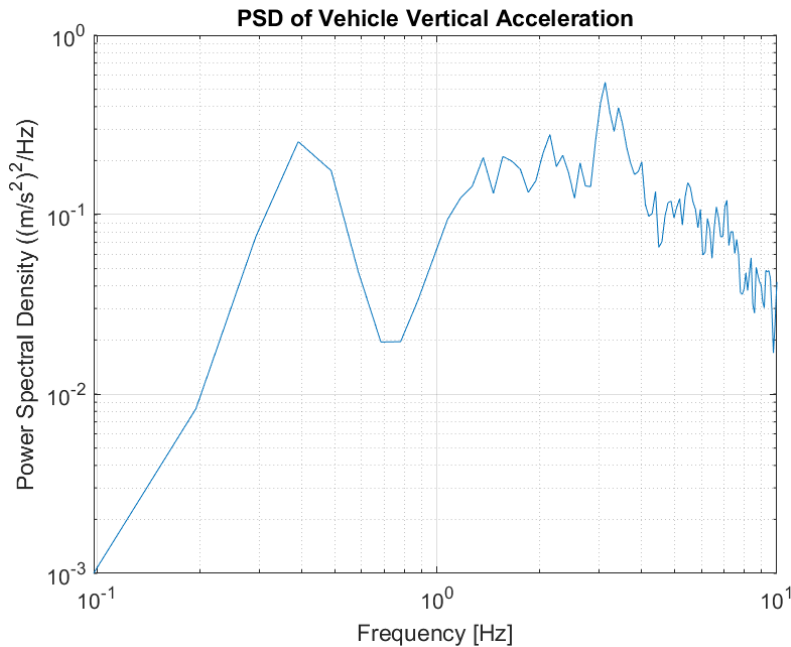


Figure 5.16. Center of gravity's vertical acceleration PSD.

Since the results of different simulations will be compared based on the acceleration, the acceleration root mean square has to be found. This will enable comparing the different acceleration values, as just looking at the plot of acceleration on time does not give a correct comparison.

$$a_{z,rms} = \sqrt{\int_{f_1}^{f_2} PSD_{acc}(f)df}$$

5.3.1 Tensioner force variation.

Tension on the chain is a very important parameter, that has a strong influence on the dynamic behavior of the vehicle. One can imagine that increasing the tension, leads to an increase of the overall stiffness of the system. On the other hand, the lower this tension is, the stiffness of the vehicle will be more characterized by the stiffness of the suspension system of the vehicle. That said, it becomes clear that when studying the vertical dynamics, the parameters that can be tuned are the tension on the chain and the suspension system parameters.

The first parameter that will be tuned is the tensioner force. This can be done from the simulation dialog box, right before the start of the simulation. ATV allows using different methods to impose the tensioner force, but the one used in this work is only the “tensioner force” (look at Appendix A for more details on the simulation setup). A total of five different simulations were performed, with the following tensioner force values:

- 15000 N
- 30000 N
- 45000 N
- 60000 N
- 90000 N

The results of these simulations are analyzed following the same steps as in the previous section. Figure 5.17 shows the comparison between the center of gravity’s vertical acceleration root mean square.

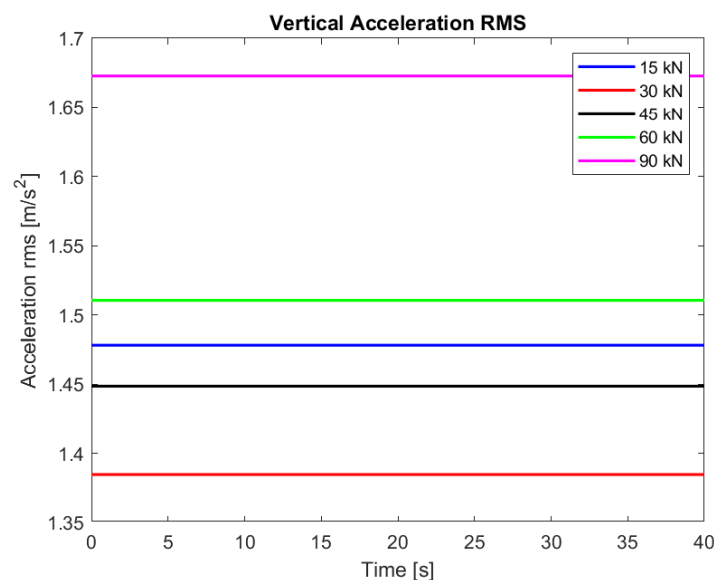


Figure 5.17. RMS acceleration for the different tensioner force values.

As can be seen from Figure 5.17, it is not possible to establish a direct relationship between the tensioner force and the vertical acceleration of the center of mass. A tensioner force of 15000 N yields higher acceleration than tensions of 30000 N and 45000 N. It is only at 60000 N that the higher tensioner force is translated in higher

vertical acceleration. Furthermore, when doing these kinds of analyses, one has to keep in mind that the also the position where the vertical acceleration is measured plays a key role. For instance, if the vertical acceleration was to be measured at the driver's seat, there is no saying that the ordering of the root mean square accelerations would remain the same.

Another way of the comparing the different models is through their PSDs. This comparison can be seen in Figure 5.18.

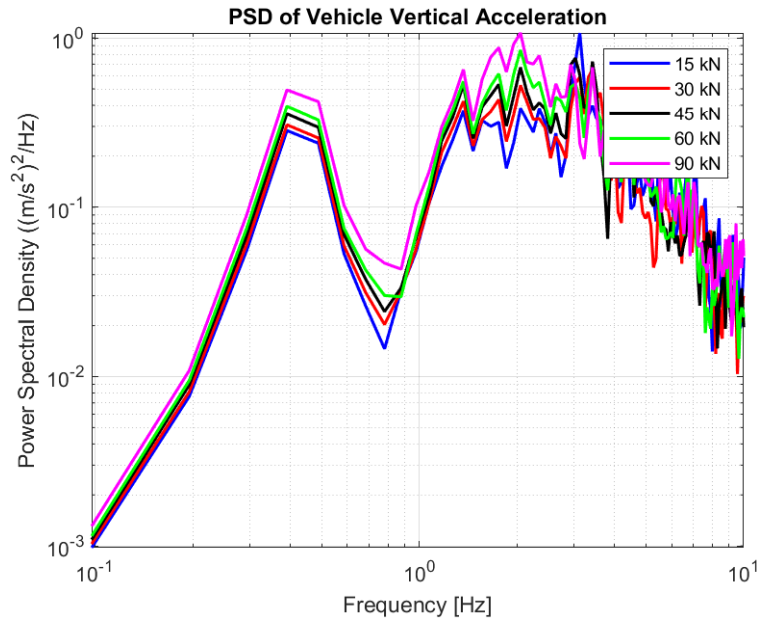


Figure 5.18. PSDs for the different tensioner force values.

Looking at the PSD, we can obtain additional information. First, there is a peak concentrated at a low frequency range (at around 0,4-0,5 Hz), which is classified as "ride", meaning low frequency oscillations, that are responsible for causing motion sickness. Then, the next peaks start at around 15 Hz, which is classified as "shake". Up until around 30 Hz, the PSD is higher for higher values of tensioner force. From this point of view, the lower tensioner force provides better comfort in the frequency range of interest.

5.3.2 Rotational springs stiffness variation.

The road wheels are connected to the hull by means of connecting arms. The suspension system is composed of torsional spring and dampers (in ATV these are called rotational, instead of torsional) that are mounted on the connection point of the connecting arm and hull, as shown in Figure 5.2.

The parameter that will be tuned in this section is the stiffness of the rotational springs. The stiffness values at which the simulation were performed are given below:

- $k_{spring,1} = 4,3 * 10^5 \frac{Nmm}{\circ}$ (default spring stiffness)
- $k_{spring,2} = 4,0 * 10^5 \frac{Nmm}{\circ}$
- $k_{spring,3} = 4,6 * 10^5 \frac{Nmm}{\circ}$
- $k_{spring,4} = 4,9 * 10^5 \frac{Nmm}{\circ}$
- $k_{spring,5} = 5,4 * 10^5 \frac{Nmm}{\circ}$

The root mean square vertical acceleration of the center of gravity and the PSDs for the different stiffness are shown in the following figures.

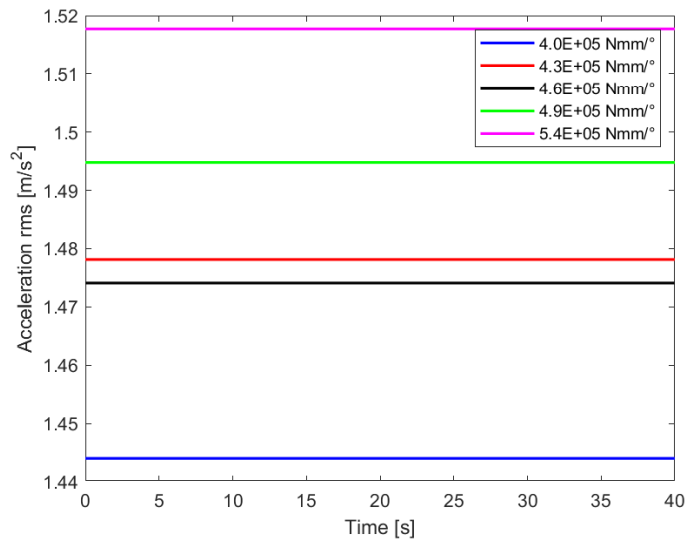


Figure 5.19. RMS acceleration for the different stiffness values.

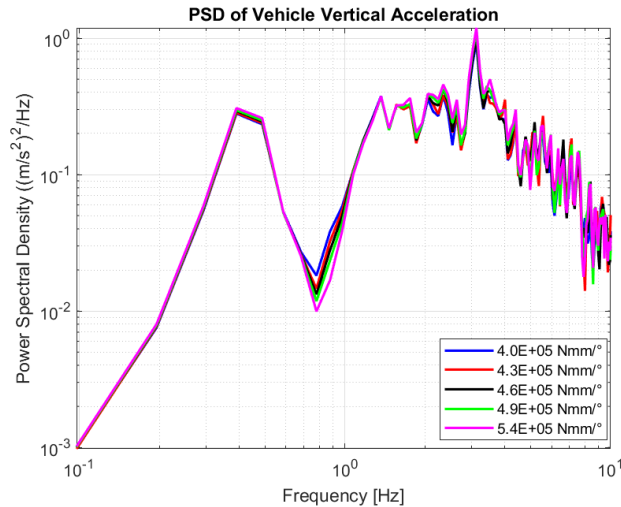


Figure 5.20. PSD for the different stiffness values.

The lowest stiffness shows the smallest RMS acceleration, whereas the highest shows the greatest RMS acceleration. However, the ordering of the acceleration does not strictly follow that of the stiffness, because as can be seen in Figure 5.19, the model with rotational stiffness of $4,3E+05 \text{ Nmm}/^\circ$ has higher RMS acceleration than the one with rotational stiffness of $4,6E+05 \text{ Nmm}/^\circ$. Nevertheless, their difference is quite small, compared to the difference that the other models show between each other.

As for the PSDs shown in Figure 5.20, the peak at 0,4-0,5 Hz remains as in the previous case, while at around 20 Hz there is a very pronounced peak. Up until 10 Hz, the increase of stiffness gives a higher PSD. For higher frequencies, the differences between the different models cannot be appreciated well, because the ordering changes continuously.

5.3.3 Rotational damping coefficient variation.

Similar to the previous two sections, the rotational damping coefficient will be varied and the effect of this variation studied through the RMS acceleration and PSD. The values of the damping coefficient will be modified as below:

- $c_{damper,1} = 90000 \frac{\text{Nmms}}{\circ} \quad (\text{default value})$
- $c_{damper,2} = 80000 \frac{\text{Nmms}}{\circ}$
- $c_{damper,3} = 85000 \frac{\text{Nmms}}{\circ}$
- $c_{damper,4} = 95000 \frac{\text{Nmms}}{\circ}$
- $c_{damper,5} = 100000 \frac{\text{Nmms}}{\circ}$

The following figures will report the PSD of the vertical acceleration and the vertical root mean square acceleration for the different damping coefficient values.

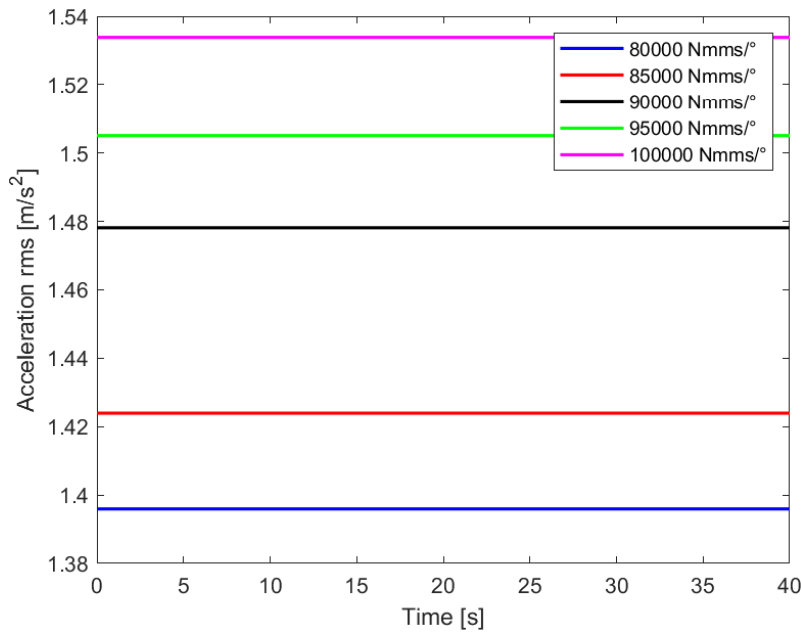


Figure 5.21. . RMS acceleration for the different damping values.

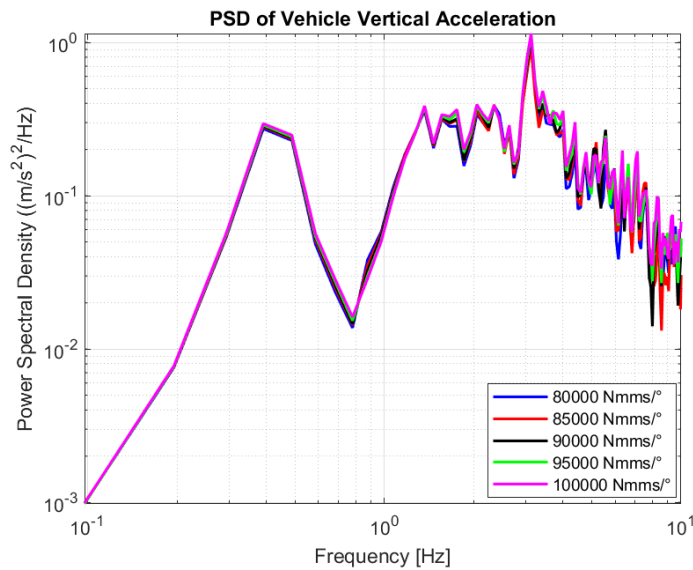


Figure 5.22. PSDs for the different damping values.

As a general rule, damping modification reduces vertical acceleration if the modified damping is closer to the optimal one. This means that both too low or too high damping coefficients lead to a worsening of ride comfort. In this case, the increase of the default damping is associated with an increase of the RMS acceleration, whereas the decrease of damping leads to RMS acceleration decrease. Also looking at the PSD, the same ordering of the acceleration is kept, namely the higher the damping, the higher the

associated energy of the signal. A possible interpretation for this behavior is that the default model is already overdamped, and the damping coefficient should be decreased if the goal is to be closer to the optimal damping. In such a way, it could be argued that if the goal is finding the optimal damping, one could keep on decreasing the actual damping, until the RMS acceleration shows an increase.

5.3.4 Frequency response of the system.

The final step in this vertical dynamics section is the investigation of the model's response to the road excitation. This is done through the FRF (Frequency Response Function), that basically is the ratio between the output, which is the vertical acceleration of the center of gravity, and the input, which is the excitation that comes from the irregularity of the road profile. We already have obtained the PSD of the road profile and of the vertical acceleration of the center of gravity in sections 5.2 and 5.4. They are related through the following expression:

$$PSD(\ddot{z}_G) = FRF_{\ddot{z}_G}^2 * PSD(h)$$

- \ddot{z}_G : vertical acceleration of the center of mass signal.
- h : road excitation signal
- $PSD(\ddot{z}_G)$: PSD of the vertical acceleration of the center of gravity.
- $PSD(h)$: PSD of the road excitation signal.
- $FRF_{\ddot{z}_G}$: Frequency Response Function of the vertical acceleration of the center of gravity.

The PSD of the road and the PSD of the acceleration are contained in different MATLAB scripts. Furthermore, the frequency ranges for which this two different PSD are defined are different. More specifically, the road PSD (in time domain) is defined in the frequency range from 0 to 125 Hz, while the acceleration PSD is defined in the frequency range from 0 to 50 Hz. These issues require loading the variables of interest from the two original scripts for road profile generation and acceleration analysis, in a new script. Additionally, the road PSD has to be evaluated at the frequency sample of the vertical acceleration, in order to end up with a road PSD that is evaluated at exactly the same frequencies as the acceleration PSD and that covers the same frequency range. This is done through the "interp1" function.

Having done these preliminary steps, calculating the FRF is just a matter of performing the square root of the output to input ratio:

$$FRF_{\ddot{z}_G} = \sqrt{\frac{PSD(\ddot{z}_G)}{PSD(h)}}$$

The result is plotted in a double-logarithmic scale, as shown in Figure 5.23.

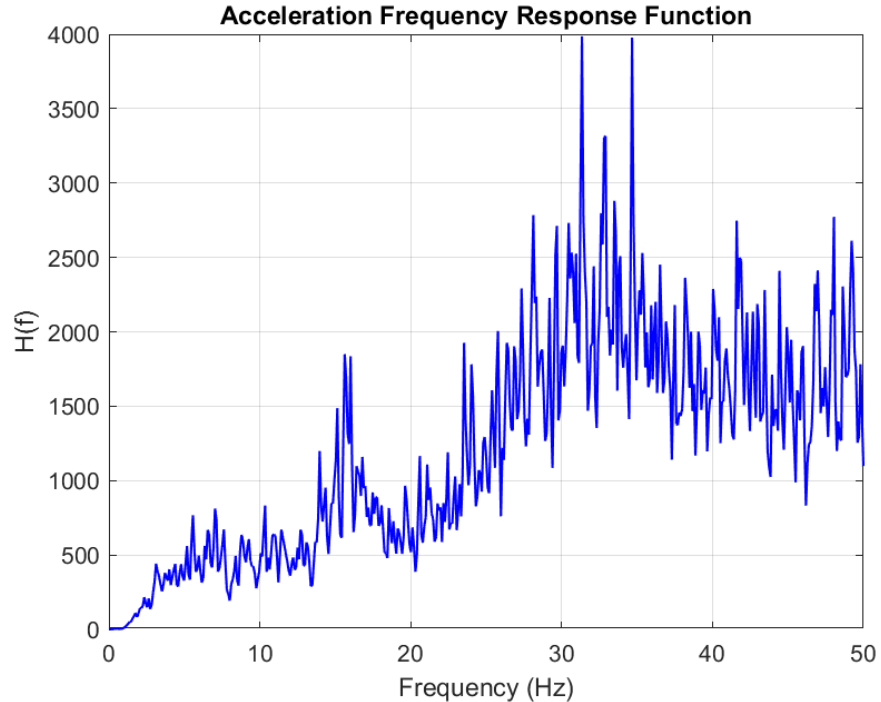


Figure 5.23. FRF of the vertical acceleration of the center of gravity.

What is striking is the presence of many peaks in the FRF. This suggests that there are many additional excitations on the vehicle. In section 5.3, it is mentioned that during the maneuver, also a modal analysis is performed, with the goal of obtaining the pitch, bounce and chain vibration frequencies. These frequencies are summarized in Table 5.1. ATV provides the natural frequencies and the damping ratio, so the damped natural frequencies can be easily calculated with the following formula:

$$f_d = f_n \cdot \sqrt{1 - \zeta^2}$$

The frequencies considered in Table 5.1 are those corresponding to the pitch, bounce and the longitudinal bending of the chain segments 1 and 2, as per their definition established in Chapter 2, where the track chain was modeled.

	fn [Hz]	ζ [-]	fd [Hz]
Pitch	1.03	81.31	0.60
Bounce	4.54	71.74	3.16
Segment 1	2.3	4.37	2.30
	3.8	0.22	3.80
	5.69	1.12	5.69
	7.76	0.28	7.76
	9.89	0.4	9.89
	12.06	0.41	12.06
	14.33	0.42	14.33
	16.78	0.47	16.78
Segment 2	3.47	13.62	3.44
	5.59	0.43	5.59
	8.59	0.51	8.59
	11.67	0.41	11.67
	15.07	0.51	15.07
	18.64	0.56	18.64
	22.64	0.78	22.64
	26.67	0.82	26.67

Table 5.1. Dynamic model frequency collection.

These frequencies will be reported on the FRF shown in Figure 5.23 as vertical lines, to verify any intersection they might have with the FRF.

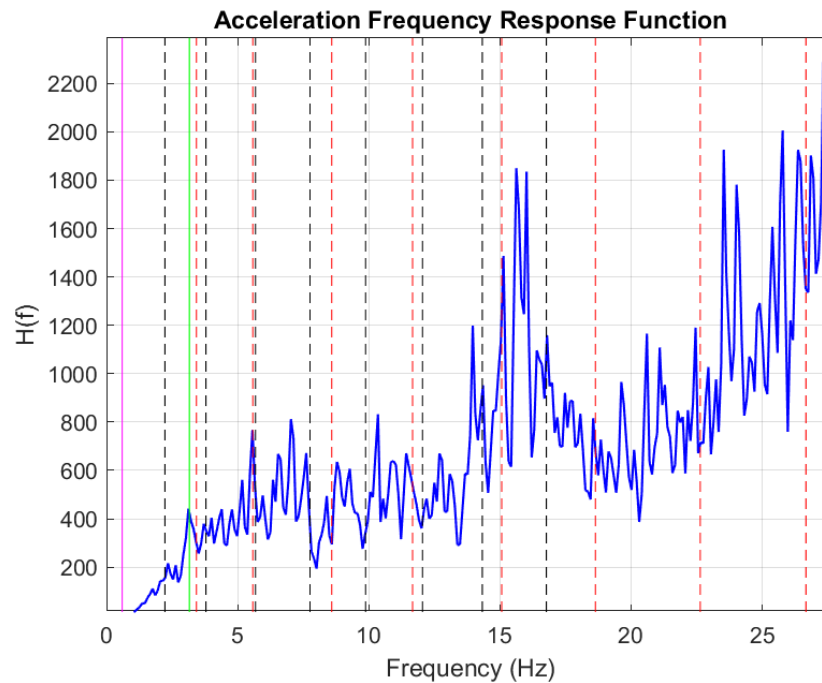


Figure 5.24. FRF intersected with the frequencies.

The lines in the plot above represent:

- Solid magenta line: pitch frequency.
- Solid green line: bounce frequency
- Dashed black line: segment 1 frequencies.
- Dashed red line: segment 2 frequencies.

From the figure, it is clear that many of the vertical frequency lines intersect either peaks or valleys in the FRF. This is a very significant result, because it shows that the global vehicle modes, such as pitch and bounce, as well as the chain dynamics, play a significant role in the dynamics of the vehicle, either by amplifying the response where there are peaks or attenuating it where there are valleys.

The current road setup is quite interesting, because it highlights the behavior of the vehicle under realistic excitation. However, the randomness of the road profile means that it is difficult to understand the contribution that the different excitations have on the vehicle's response, as was seen in Figure 5.24. For this reason, it seems fit to study the vehicle while it travels under a sinusoidal road profile, with well-defined characteristics. Such road profile is not readily available in ATV or Adams Car, so it must be generated in a MATLAB script and then converted in a file format suitable to be read from ATV. Since there are many ways to generate such profile, the script will not be shown. The sinusoidal road parameters will be reported instead:

- *Total length of the road: 300 m*
- *Sinusoidal portion length: 280 m (10 m of initial and final straight run)*
- *Wavelength: 0.1579 m (the choice of this parameter will be justified later)*
- *Amplitude: 0.04 m*
- *Road width: 5 m*

The goal of this part is to provide a combined excitation that is caused by the superposition of the track chain bending, sprocket excitation and road excitation.

To perform this, a simulation where the vehicle is in steady-state is required. In this simulation, a modal analysis is performed and a mode shape with low damping is chosen. More specifically, the mode shape chosen was global, consisting in vertical bending of both segments 1 and 2, with un-damped natural frequency and damping ratio:

- $f_n = 9.74 \text{ Hz}$
- $\zeta = 1.03\%$

This frequency serves as the sprocket meshing frequency (meshing contact between the sprocket wheel and chain) that will be imposed on the following simulation. This simulation will be performed on a perfectly flat road, and the excitation we expect to see comes from the sprocket wheel. By imposing this frequency on the sprocket wheel, the velocity at which the simulation will be performed is the following:

$$f_{excitation} = n_{teeth,sprocket} \cdot \frac{V_{vehicle}}{2 \cdot \pi \cdot r_{sprocket}} = 9.74 \text{ Hz}$$

$$\Rightarrow V_{vehicle} = \frac{f_{excitation} \cdot 2 \cdot \pi \cdot r_{sprocket}}{n_{teeth,sprocket}} = 1.478 \text{ m/s}$$

However, tracked vehicle, especially when traveling on asphalt, always show some slip, so this will not be the actual velocity and actual sprocket frequency that the tank is traveling with. Looking at the simulation results from the ATV post-processing window, the actual sprocket frequency is equal to:

$$n_{act,sprocket} = 300.21^\circ/s \Rightarrow n_{act,sprocket} = 50.035 \text{ rpm}$$

$$\Rightarrow f_{act,sprocket} = n_{teeth} \cdot \frac{n_{act,sprocket}}{60} = 9.173 \text{ Hz}$$

Similarly, the actual vehicle velocity is:

$$V_{act,vehicle} = 1.448 \text{ m/s}$$

As is to be expected, the PSD of the vertical acceleration of the center of gravity in this case has a peak at nearly 9.17 Hz, as shown in the figure below.

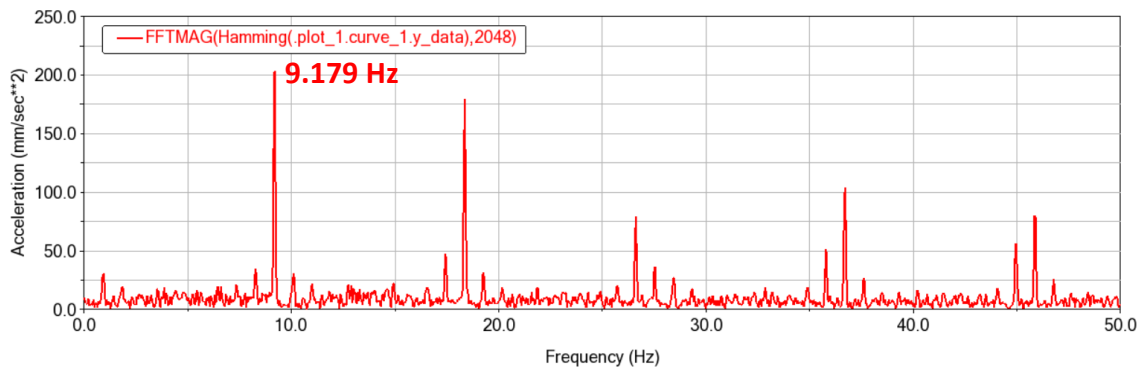


Figure 5.25. Vertical acceleration PSD for the flat road simulation (only sprocket excitation).

Knowing these values of velocity and frequency, the wavelength of the road profile can be calculated as (this is the value shown in the road parameters):

$$\lambda = \frac{V_{act,vehicle}}{f_{act,sprocket}} = 0.1579 \text{ m}$$

A simulation is performed on this sinusoidal profile, with the following parameters:

- *Idle wheel tension*: 15000 N

- *Velocity:* 1.478 m/s (this value is the sprocket tangential velocity, the actual one will be lower due to slip).
- *Duration:* 20 s

As in the previous simulations, the results of will be elaborated in MATLAB, where the PSD will be obtained. It is reported in the figure below.

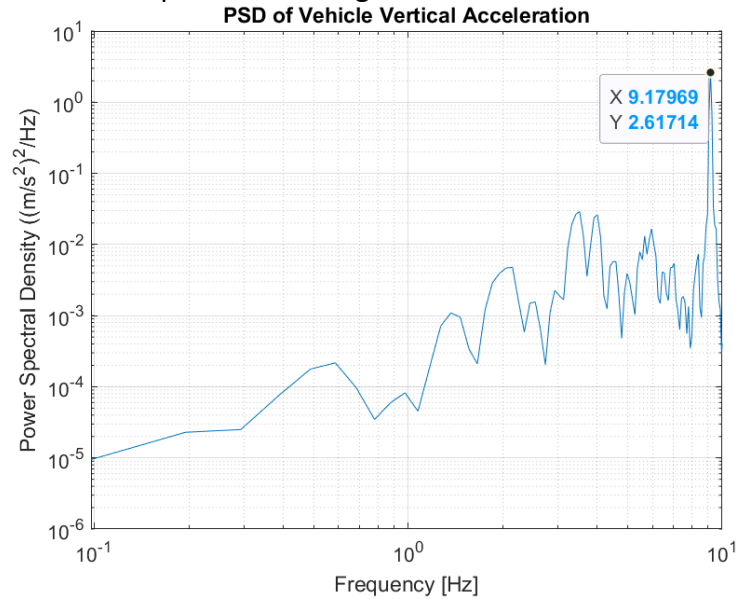


Figure 5.26. Vertical acceleration PSD (sinusoidal road).

The PSD of the road profile will be obtained once again in a manner similar as for the first road profile. Its temporal frequency will be obtained with a velocity of 1.448 m/s.

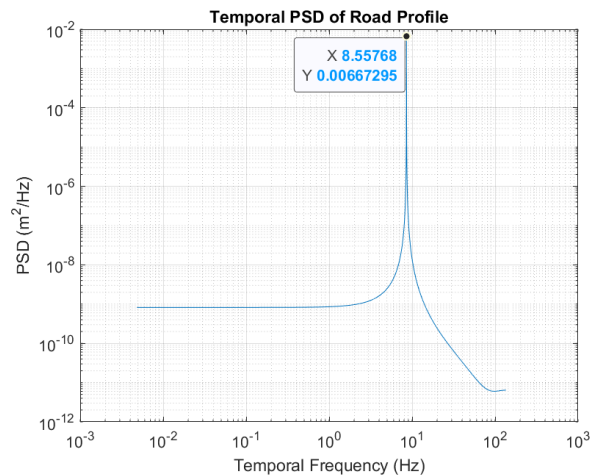


Figure 5.27. Time domain PSD of the sinusoidal road.

Performing the ratio between the PSD of the acceleration and the PSD of the road profile, we can obtain the response of the vehicle.

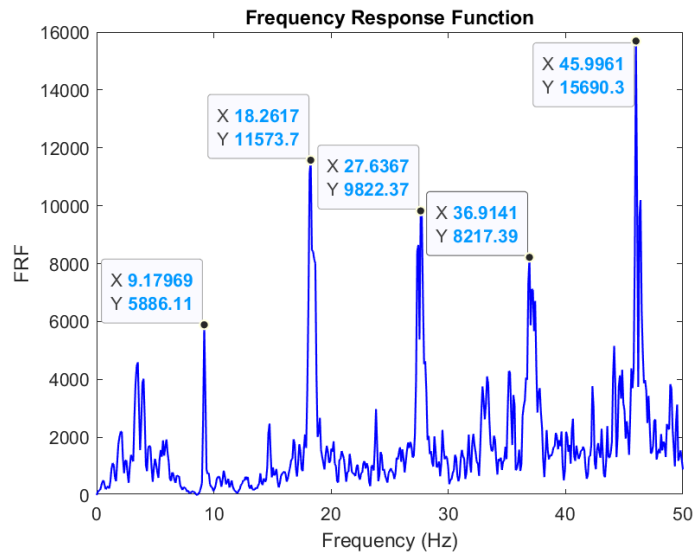


Figure 5.28. Response of the vehicle under combined excitation.

6 Conclusions

The results obtained throughout this thesis work can be grouped in two categories.

- The first consists on the modeling of the upper portion of track chain through analytical methods that require only geometrical characteristics of the chain and some contact properties, which might be known a priori. These are the tension on the chain, the stiffness (either linear or torsional) between the track elements, and track material properties. From the user's point of view, some knowledge and understanding of structural mechanics and dynamics of systems is required, in order to setup an analytical procedure following the steps described in this thesis, while performing minor adjustments to the methodology to account for differences between the tracked vehicle models under investigation.
- The second category contains results related to the vertical dynamics of the tracked vehicle, which is studied by monitoring the tracked vehicle's center of gravity vertical acceleration, while it travels through a known road profile at constant speed. Knowing these, the response of the vehicle to the road excitation can be evaluated. Additional contributions to the vehicle's response, arising from the chain excitation, can also be identified, combining the results of this part with the track chain modeling studied in previous sections.

The procedure followed to obtain the first group of results is the following:

- Performing static simulations, with different tensioner force values, to obtain the frequencies of the chain mode shapes. The mode shapes can be of three kinds:
 - Chain bending in the (X-Z) plane.
 - Chain bending in the (X-Y) plane.
 - Chain torsion around the X-axis.
- Each of these three behaviors will be modeled considering a different element.
- The chain bending in the (X-Z) plane will be modeled by an equivalent model consisting of strings in tension. More specifically, the upper chain portion (for the default tank) will be considered as made by two strings, in such a way that one string ranges from the sprocket wheel to the support roll and the other from the support roll to the idle wheel. The strings being continuous systems, we can calculate their natural frequencies by knowing the tension on the string, its length and its linear mass density. The frequencies of the harmonics are compared with the ones of the simulation. The chain was also studied considering it as a discrete system, made on "n" rigid elements, that are connected by linear and torsional springs. The mass and stiffness matrices were obtained with the Newtonian approach. They were then implemented in MATLAB and the EVP was solved.

- The chain torsion around the X-axis will be modeled by an equivalent shaft in torsion. This equivalent shaft will span the entire length of the upper chain. In this case, an equivalence between the continuous system (shaft) and the discrete system (chain) is established (the equivalence is set considering a Wave Motion Demonstrator). The wave equation of the shaft in torsion is adjusted considering this equivalence with the discrete system and the expression of natural frequency is found. The frequencies for the first five harmonics are compared with the ones that the simulation provides.
- The chain bending in the (X-Y) plane will be modeled by an equivalent Euler-Bernoulli beam. Similar to the other cases, the expression of the natural frequencies will be computed and the results will be compared with the simulation. In this case, the results obtained from the Euler-Bernoulli beam model were not satisfactory, so another method was proposed. The alternative consists in studying the upper portion of the chain as a discrete system consisting of “n” rigid bodies, connected to each other by means of linear and torsional springs. Each of these rigid bodies has two DOFs. The system was studied using the Newtonian approach. The mass and stiffness matrices were obtained with the Newtonian approach and implemented in MATLAB, where the EVP was solved.

Summary of the results:

- The bending in the (X-Z) plane modeled with the equivalent strings gives results that are close to the ones of the simulation. There is a minor diverging trend at the higher harmonics, but in the lower frequency range, the approximation with the string is good enough. The discrete model, on the other hand, gives very good results not only for the low harmonics. The relative error between the discrete model and the simulation is only a few percent. For these reasons, if ease of computation is important, the suggested model is the continuous string, while if the quality of results is more important, the discrete model is recommended.
- The torsion around the X-axis modeled as a shaft in torsion yields very good results, except for the first harmonic. The consecutive harmonics give an increasingly good approximation, meaning that the decision of performing the equivalence between the continuous and discrete system gives very good results.
- The bending in the (X-Y) plane was initially modeled with a Euler-Bernoulli beam. The approximation at low harmonics can be considered good enough, but as the harmonics increase, the trend is very diverging. For this reason, this model is not recommended. The other possibility is modeling the upper chain as a discrete system. This discrete system considers each pad as a rigid body, and consecutive

pads are linked by means of linear and torsional springs, given that the connection is modeled by ATV as having a linear (translational) and torsional (rotational) stiffness. Each pad has two degrees of freedom, namely translation (Y-axis) and rotation (around the Z-axis). The presence of the support roll and its contact with one of the pads means that it has to be modeled as a lumped linear spring, but this does not add any additional complexity to the system computation-wise. By using a Newtonian approach, the eigenvalue problem is solved (implementing the problem in MATLAB) and the natural frequencies of the multi-degree of freedom system are obtained. These frequencies are compared with the ones of the simulation, and the result is that the approximation is very good, especially at higher harmonics. The conclusion of this section is that the discrete system model gives the best results and its implementation is straight-forward.

To conclude the results related to the modeling of the upper portion of the track chain, it can be said that the approach suggested on this thesis is both easy to implement and provides good results, especially at an initial design stage, where experimental work, or access to a proper simulation software, such as the Adams Car ATV toolkit used throughout this work, is not possible due to the considerable cost of any of them. However, there is always room for improvement, as the models proposed can be further refined to obtain an even better approximation of the real behavior of the track chain.

The procedure performed to obtain the vertical dynamics results is summarized below:

- The road profile is generated in MATLAB starting from the “ride_quality_3inch_measured”. Its PSD is generated following the steps reported in section 5.1.
- The simulation is set at a constant forward velocity. The results of the simulation are converted from “.res” files to “.mat” files, so the post-processing can be made in MATLAB. The vertical acceleration of the center of gravity is plotted in time and its frequency content studied by generating its PSD.
- Some system parameters, such as tensioner force, stiffness and damping of the suspension are changed one at a time, to see how this variation influences the tank behavior in terms of its center of gravity vertical acceleration.
- Finally, the response of the default tank model is obtained through the acceleration PSD and road PSD. Other contributions to the FRF, in addition to the road excitation, are identified and plotted in the FRF.

Summary of the vertical dynamics results:

- The road profile that was used to perform the analysis is at first glance random, but studying its frequency content through the spatial PSD, a quite remarkable similarity between it and the standard road profile E, as defined in ISO8608 [7], is found. Moreover, looking at the spatial spectrogram of this road, highlighted a region of very low frequency excitation that was high in amplitude. Removing the trend of the road signal, kept the spectrogram unchanged, with the exception of this low frequency excitation, that was completely removed. This lead to the conclusion that this road profile is not exactly linear in its trend, but is part of a greater sinusoidal profile, with much higher amplitude and wavelength than the road profile, meaning that the road was linearized due to being a portion of this sinusoid. These results are quite interesting, because they provide more insight on what looks like a random road profile, but that is actually made to resemble a standard ISO road and that is generated as a small portion of a much bigger wave.
- An increase in the tensioner force, should theoretically cause an increase in the overall stiffness of the system, which would bring an increase of the RMS acceleration. However, the simulations show that the tensioner force is not necessarily related to the RMS acceleration. Furthermore, the increase in RMS acceleration between two consecutive tensioner force values is not constant. For instance, the ordering of the RMS acceleration (increasing) as related to the tensioner force, goes as follows:
 - 30000 N
 - 45000 N
 - 15000 N
 - 60000 N
 - 90000 N
- When it comes to the rotational springs stiffness variation, increasing the stiffness brings an increase of RMS acceleration, with the exception of second and third lowest RMS acceleration, where the higher of the two gives a lower acceleration. The ordering of the stiffness values, corresponding to an increase in RMS acceleration is as follows:
 - $4.0E+05$ Nmm/°
 - $4.6E+05$ Nmm/°
 - $4.3E+05$ Nmm/°
 - $4.9E+05$ Nmm/°
 - $5.4E+05$ Nmm/°
- Varying the rotational damping shows a direct link between the damping coefficient and the RMS acceleration, in such a way that increasing it results in a RMS acceleration increase. This is due to the fact that the system is overdamped. Decreasing damping to the point that it goes below the optimal damping, would have the opposite effect, namely show an increase in RMS acceleration.

- FRF of the vertical acceleration of the center of gravity shows many peaks and valleys. For this reason, it becomes obvious that the response of the vehicle is due to many contributions and not only the road profile irregularity. By performing a modal analysis of the dynamic model, it is possible to obtain the frequencies of the pitch, bounce and chain mode shapes in longitudinal bending. These frequencies, if inserted in the FRF plot as vertical lines, intersect many of the peaks and valleys, highlighting the importance the chain dynamics has in the behavior of tracked vehicles, as compared to conventional wheeled vehicles.

To sum up the vertical dynamics study, some models were developed and the sensitivity of the default tank model to common modifications was observed. Being able to identify the chain contribution to the response of the vehicle is also quite interesting. That said, vertical dynamics can be studied in even more detail. Starting from the work presented in this thesis, one can go even deeper, by identifying the optimal damping of the model and by combining different setup in terms of tensioner force, stiffness and damping to achieve the best overall results.

Appendix A

A.1 ATV simulation setup for the static frequency analysis.

The mode shapes of the chain can be obtained by performing a static simulation and using the correct command in the simulation file that allows the linearization and modal analysis of the system. The simulation is static, because the goal is understanding the modes of the chain, without considering any additional contribution. Furthermore, even if the simulation is dynamics, ATV works in such a way that the system is linearized for the instant of time that the user is interested in. This means that during a dynamic simulation, if more than one linearization and modal analyses are performed, the results of these analyses will be different. A guide on how to perform a simulation of this kind is given below.

1) Loading the tank model.

The tank model is loaded by going to the “File” menu, clicking on “Open” and then on “Assembly”. On the dialog box that appears, the user can right-click on the “Assembly name” field and search the databases for the tank model. In this case, the “tank” assembly from the “shared_atv_database” was used. This is the simplest tank model, with all the default parameters and no means of controlling its velocity (not required since the simulation is static).

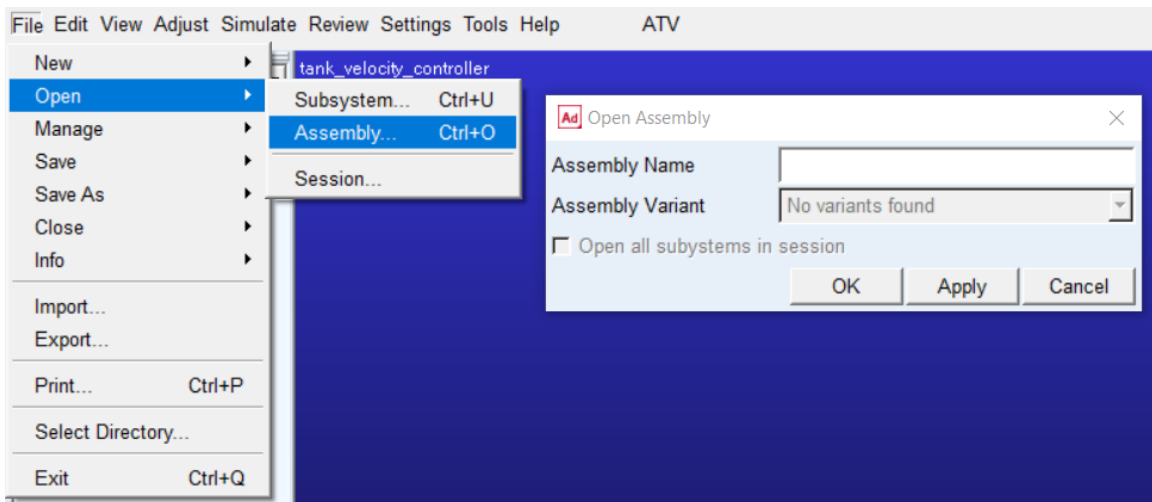


Figure A.0.1. Generating the default tank assembly.

2) Wrap the chain around the wheels.

Once the model is loaded, the chain has to be wrapped around the wheels. This can be easily done by clicking on the “ATV” menu, “Tracked Vehicle – Dynamic Track”, “Dynamic Track Wrapping”. At this point, the user has the choice between “Half

Vehicle” and “Full Vehicle”, which means that the simulation will be performed either considering the left half of the vehicle or the entire vehicle respectively. The simulations throughout this thesis were performed with “Half Vehicle”, as it is less time-consuming and since there are no steering maneuvers, there would be no difference between the half and full vehicle models.

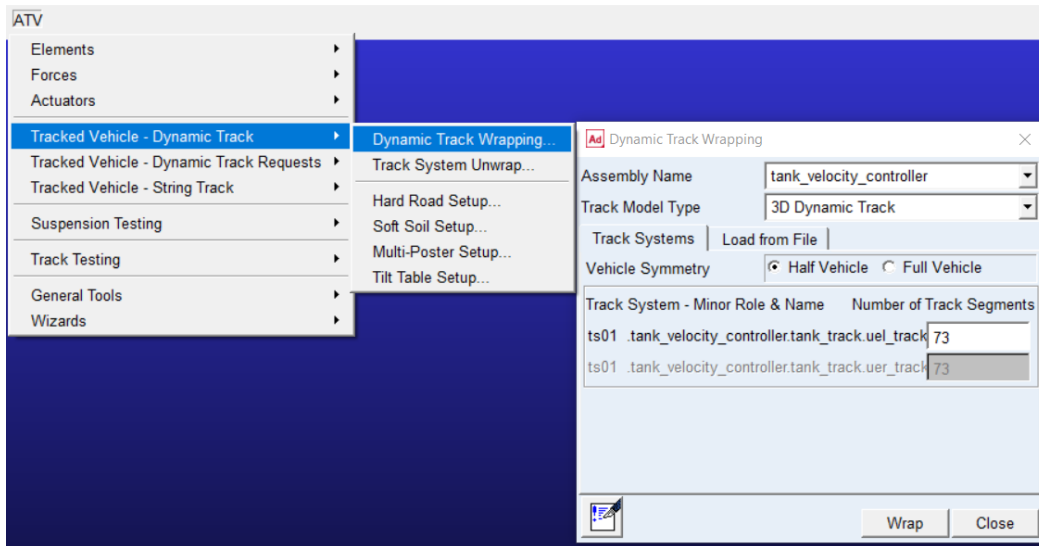


Figure A.0.2. Performing the dynamic track wrapping.

3) Loading the road profile.

The road profile is loaded from “ATV”, “Tracked Vehicle – Dynamic Track”, “Hard Road Setup”. The “Number of Road Data Files” is set to 1. In “Road Data File” is chosen “flat” and in “Soil Property File” is chosen “dry_asphalt”.

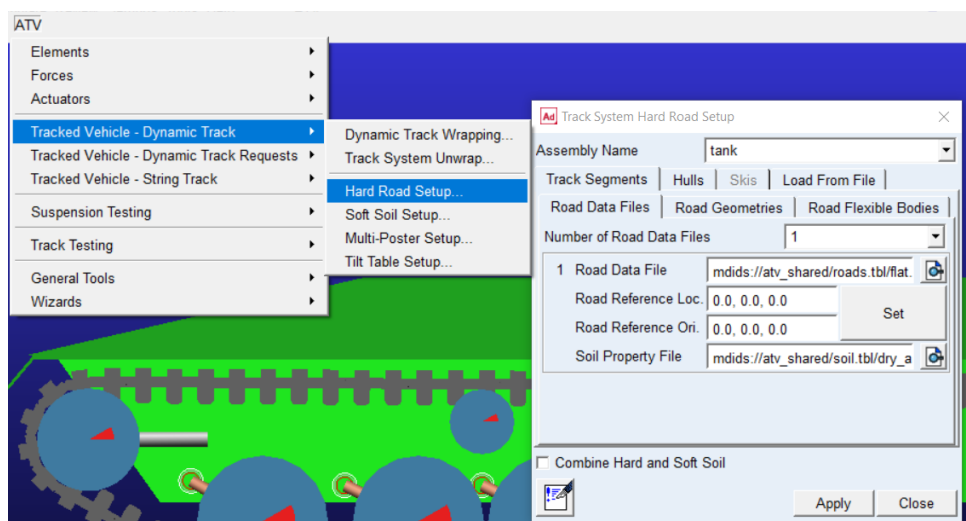


Figure A.0.3. Loading the road profile.

4) Creating track segment requests.

This step is not strictly necessary, but it is useful if the user wants to extract additional information about the displacements and forces that track segments exchange between each other and the ground. To create track segment requests, click on the “ATV” menu, “Tracked Vehicle – Dynamic Track Requests”, “Track Segment Request”, “Create”. On the dialog box that appears, by right-clicking the “Track Segment” field, the user can choose for which track segment the request will be created, or alternatively click on “Select All”, to create request for every track segment. Additionally, the kind of request required can be specified. The results of these request can be seen after the simulation in the “Post-processing window”.

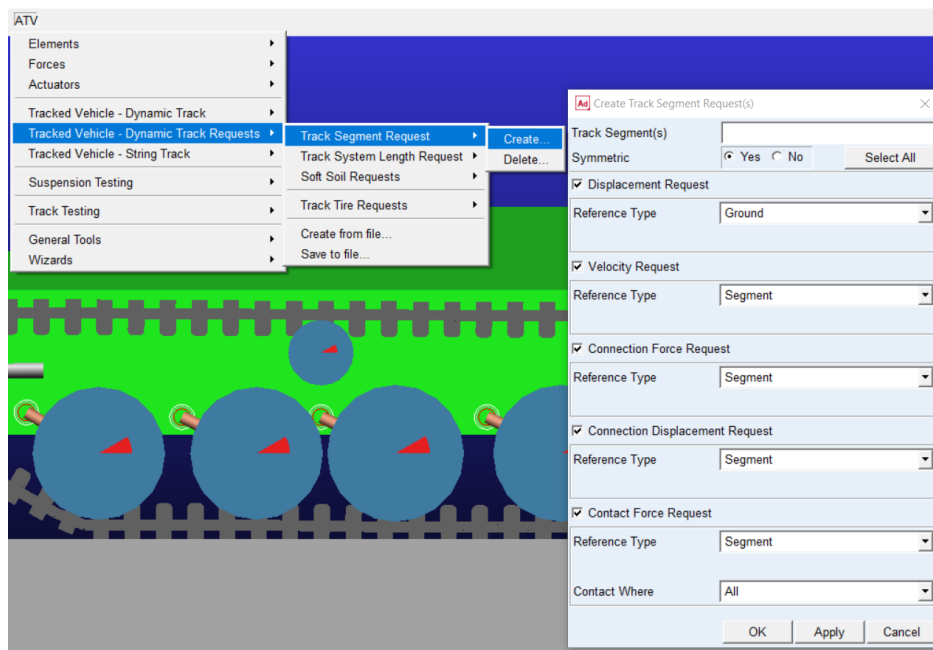


Figure A.0.4. Creating track segment requests.

5) Setting the solver settings.

The solver settings can be modified from the “Settings” menu, “Solver”. The parameters set on the solver have a big influence on the simulation. It is recommended, due to the presence of many contacts, to change the “Integrator” from “GSTIFF” to “HHT”. Furthermore, the thread count can be changed by changing the “Category” to “Executable”, clicking on “More” and typing the number of threads on the “Thread Count” field.

6) Setting the simulation.

The simulation can be set from the “Simulate” menu, “Tracked Vehicle Analysis”, “Full Vehicle Submit”. On the dialog box that appears, the user can choose the analysis name, the simulation duration, the initial velocity of the maneuver and more. For what was done on the static analyses throughout this thesis, the simulations were set to a duration of 20 seconds with step size of 0.01, and the “Mode of Simulation” was set to “files_only”. Another important parameter to tune at this point is the tensioner. This can be done through the “Setup” button. On the window that appears, the “Setup Type” was changed from “Tensioner Design Length”, which controls the tension by adjusting the length of the tensioner and usually gives very high tension values, to “Tensioner Force”, which allows typing the value of tension that the tensioner should impose.

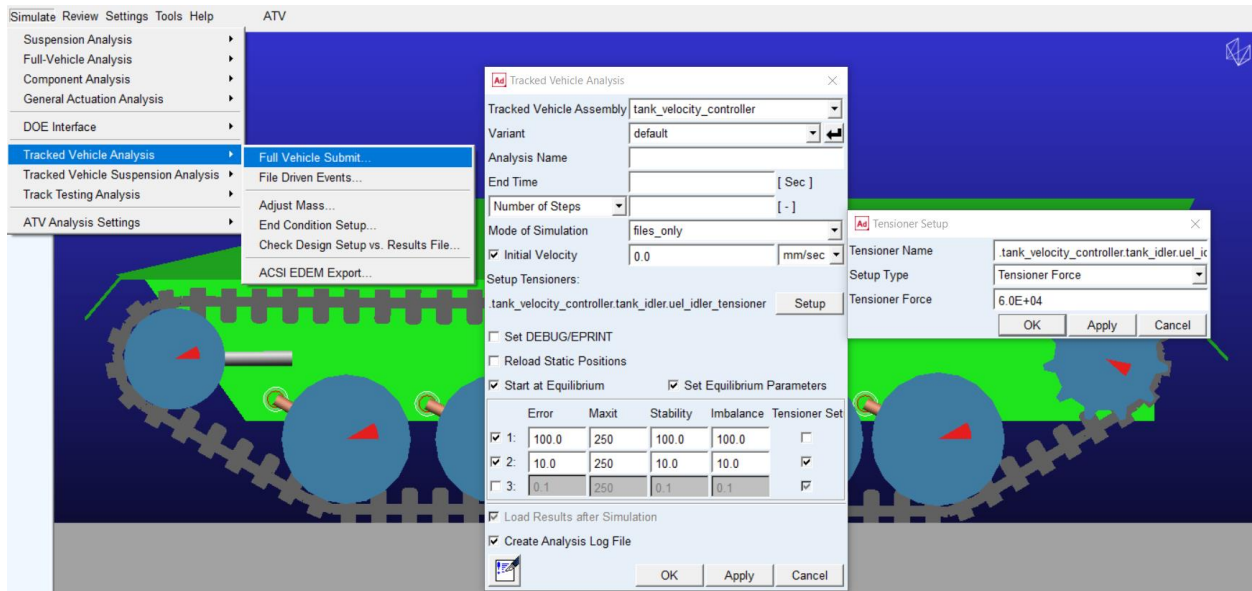


Figure A.0.5. Setting the tracked vehicle simulation.

After clicking “OK”, the analysis is read and the user has to modify the simulation file by including the command that will perform the modal analysis. The file can be usually found on “Users” and it has the “.acf” extension. It should be opened with a text editor and the line “linear/eigensol” should be inserted before the last row. This modification can then be changed the “.batch” file can be opened to continue running the simulation. The running duration will depend on many factors.

```

1
2 file/model=mode_shapes_new_support_roll_30kN
3 !
4 preferences/solverbias=cxx
5 !
6 !
7 equilibrium/error=100.000000,maxit=250,stability=100.000000,imbalance=100.000000
8 simulate/static
9 !
10 equilibrium/error=10.000000,maxit=250,stability=10.000000,imbalance=10.000000
11 ! The next line will perform a static simulation and set the tensioners
12 control/routine=atv_solver::atv_TensionerConsub,function=USER(1, 6)
13 !
14 simulate/dynamics, end=20.0, dtout=0.010000
15 !
16 linear/eigensol
17 stop
18

```

Figure A.0.6. Modifying the simulation file to perform the modal analysis.

7) Reading the simulation results.

The results of the simulation can be read by clicking on the “Review” menu, “Analysis Management”, “Read”. Right-click on the “Analysis Name”, and search for the “.res” file on the folder where the results were saved. By default, the results are saved under “Users”.

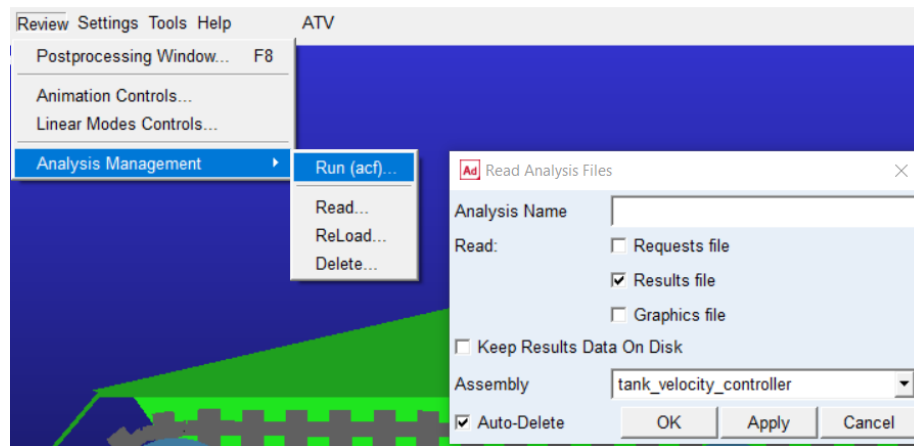


Figure A.0.7. Reading the simulation results.

The modal analysis results can be read by clicking on “Review”, “Postprocessing window”. On the window that appears, click on “View”, “Load Mode Shape Animation”. The window that shows the mode shapes appears. On the “Table of Eigenvalue” tab, the user can see the list of eigenvalues, ordered according to the imaginary part of the eigenvalue. It is recommended to start the mode shape analysis starting from the first mode that has a non-zero imaginary part of eigenvalue.

A.2 ATV simulation setup for the vertical dynamics study of the tracked vehicle.

The following guide will show how the simulation for the vertical dynamics study was setup. Some of the steps are the same as in the previous section, but there are quite a few differences.

- 1) Loading the tank model (done exactly as in the previous section).
- 2) Adding the velocity controller subsystem.

These simulations, contrary to the previous ones, are dynamic. This means that throughout the maneuver, we have to ensure that the tank maintains the correct speed. This can be done through the velocity controller subsystem, that is not part of the default tank model, but has to be added by the user. After loading the default tank model, the velocity controller can be added by clicking on the “File” menu, “Manage”, “Assemblies”, “Add Subsystem”. On the dialog box that appears, right-click on “Subsystem(s)” and from the “ATV_shared_subsystems” choose “tank_controller_powertrain”. In this way, a PID controller that ensures the correct velocity is added to the model.

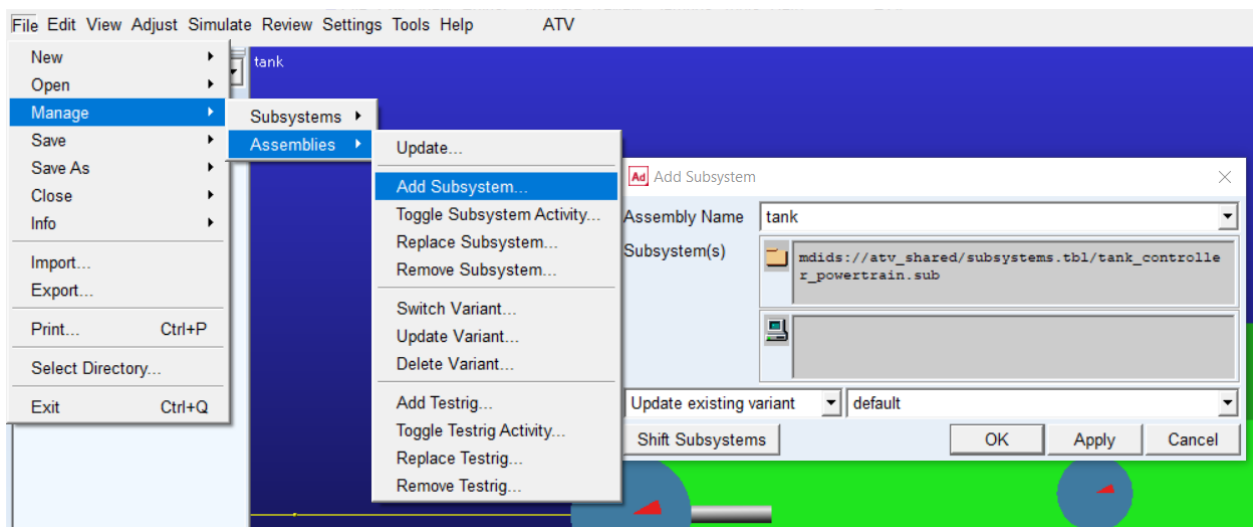


Figure A.0.8. Adding the velocity controller subsystem.

- 3) Wrapping the chain around the wheels (as done in the previous section).
- 4) Loading the road profile.

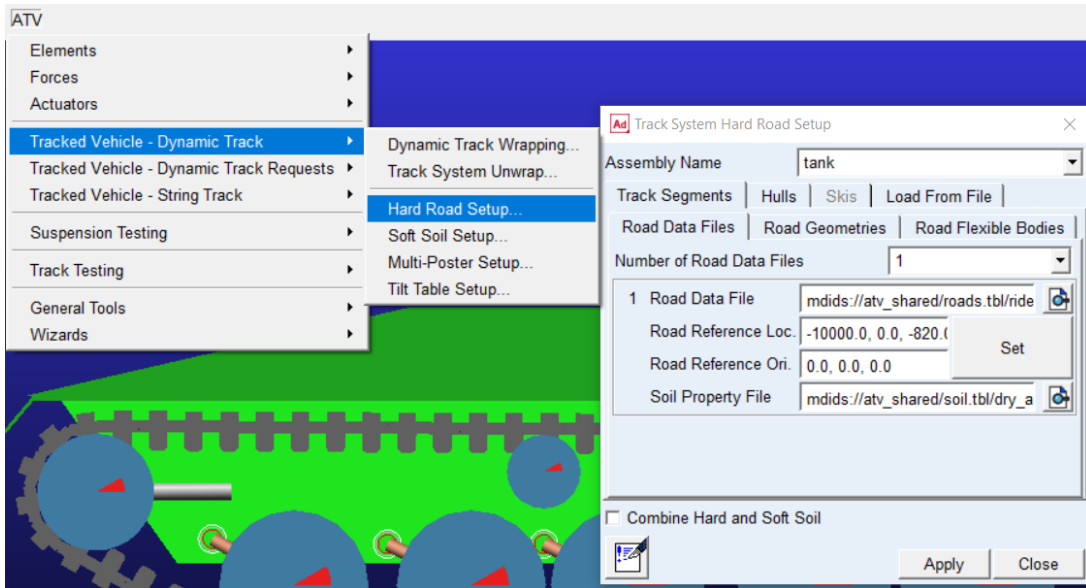


Figure A.0.9. Loading the rough road profile.

In this case, the road is loaded in the same way as in the previous section, but in the “Road Data File” the “ride_quality_3inch_measured.rdf” is chosen. This generates the rough road profile on which the vehicle will be tested. The “Road Reference Loc” is chosen as (-10000, 0, -820), to ensure that the maneuver starts on the correct portion of the road, which is before the rough profile starts.

- 5) Tuning the velocity controller.

The velocity controller parameters are set through “ATV”, “Actuators”, “Modify Velocity Control”. The parameters for the simulations performed are set as in the figure that follows.

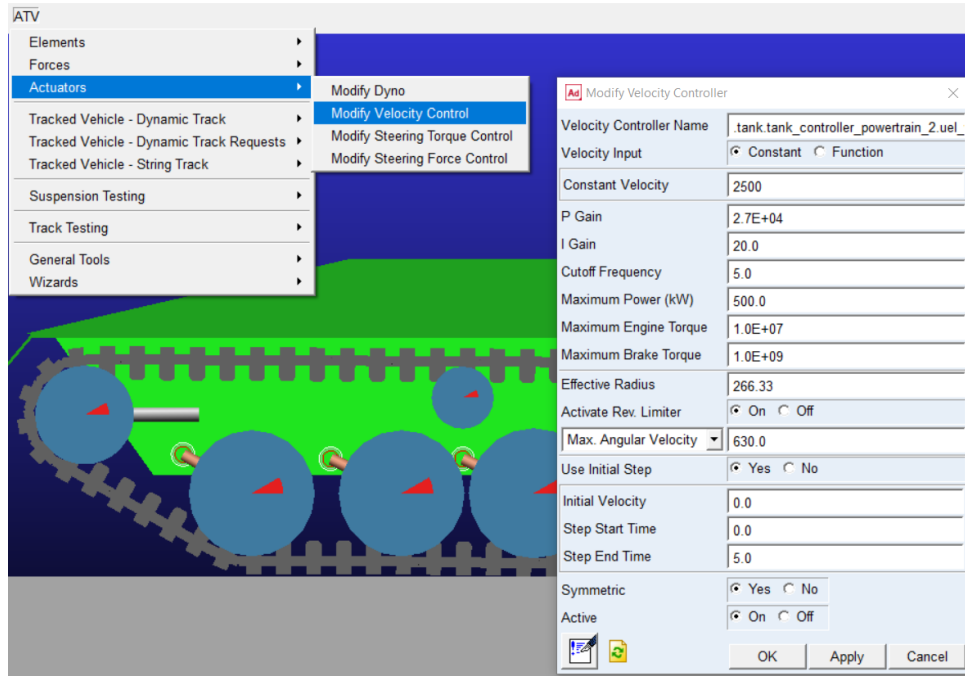


Figure A.0.10. Setting the velocity controller parameters.

- 6) Setting the solver settings (as in the previous section).
- 7) Setting the simulation.

The simulation is set as in the previous case, with the difference being in the “Mode of Simulation”, that is kept as “background”. This means that the simulation will start with pressing “OK” and no modifications have to be performed on the simulation file.

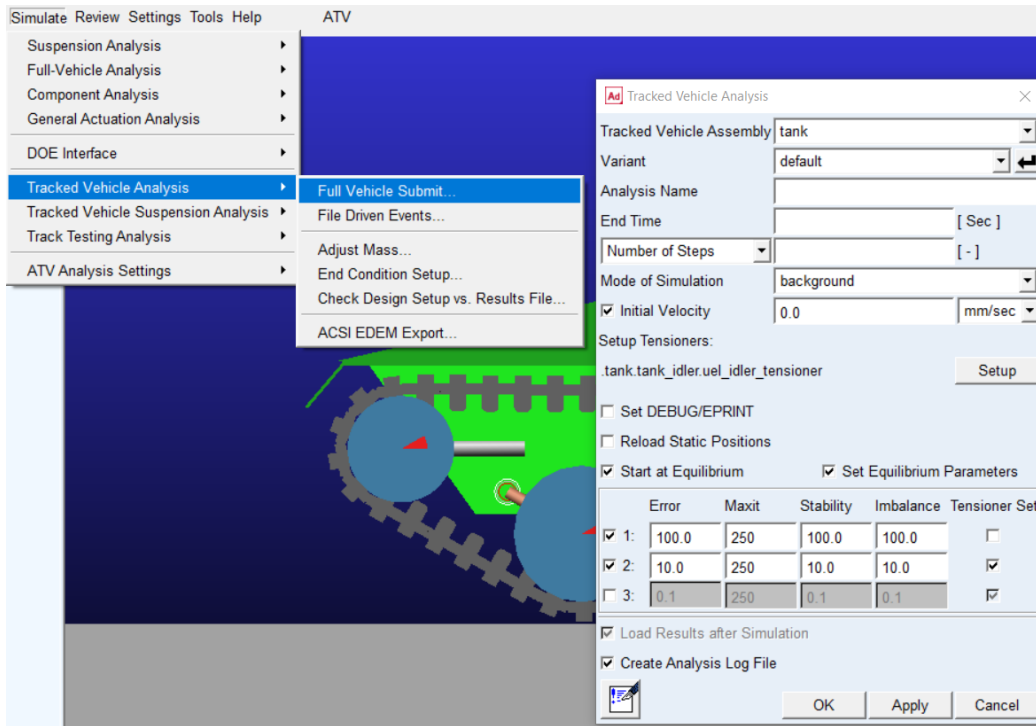


Figure A.0.11. Setting the simulation settings.

Appendix B

In this appendix, the passages used to obtain the natural frequency expressions for the string in tension, shaft in torsion and Euler-Bernoulli beam models will be detailed. The procedures shown are introduced in the Mechanical System Dynamics[5] course of this university. As a general rule, the procedure starts with the FBD of the continuous element. The equilibrium is performed, with the goal of obtaining the wave equation. The boundary conditions are imposed to get the corresponding shape function, from which the expression of natural frequency can be obtained.

B.1 Procedure to obtain the natural frequency of the equivalent continuous string in tension.

The free body diagram of a portion of string in tension is shown in Figure B.1.

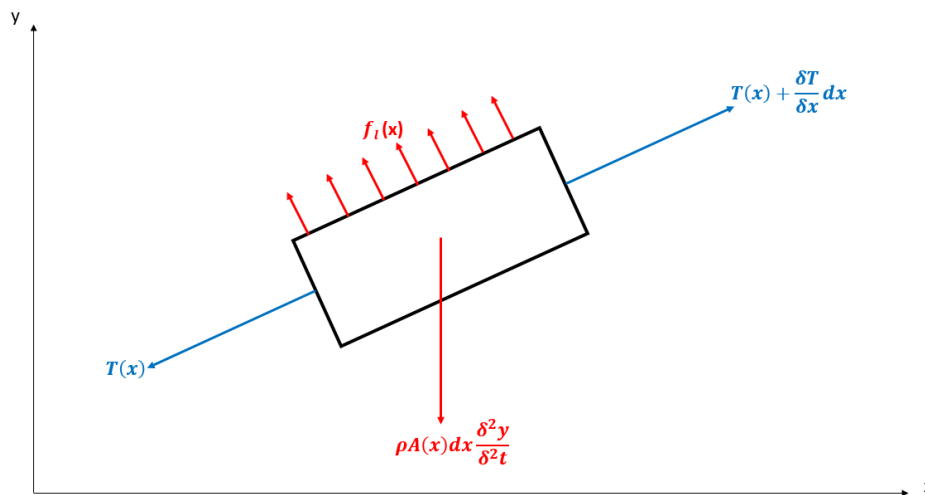


Figure B.0.1. FBD of the string.

The string is linearized by considering small angles, which allows expressing the rotation as a function of coordinates x and y . The vertical equilibrium of the system is performed.

$$\uparrow) [T(x) + \frac{\delta T}{\delta x} dx] - T(x) \frac{\delta y}{\delta x} + f_l(x) dx - \rho A(x) dx \frac{\delta^2 y}{\delta t^2} = 0$$

Elaborating this expression and assuming that the higher order terms are neglected, the wave equation is obtained.

$$\frac{\delta^2 y}{\delta t^2} = \frac{T}{\rho A} \frac{\delta^2 y}{\delta x^2}$$

- y : vertical (transverse) displacement of the string.
- x : longitudinal displacement of the string.
- $\rho \left[\frac{kg}{m^3} \right]$: density of the string material.
- $A [m^2]$: cross-sectional area of the string.

The general solution of the wave equation is given as:

$$y(x, t) = \eta(t)\phi(x)$$

- $\eta(t)$: time function.
- $\phi(x)$: shape function.

Substituting this solution in the wave equation expression, we obtain:

$$\frac{1}{\eta(t)} \frac{\delta^2 \eta(t)}{\delta t^2} = c^2 \frac{1}{\phi(x)} \frac{\delta^2 \phi(x)}{\delta x^2} = -\omega^2$$

- $\omega \left[\frac{rad}{s} \right]$: frequency of the string.
- $c \left[\frac{m}{s} \right]$: wave propagation speed in the string.

The solution of the equation is separated in time dependent and space dependent terms.

$$\begin{aligned} \ddot{\eta} + \omega^2 \eta &= 0 \\ \phi'' + \left(\frac{\omega}{c} \right)^2 \phi &= 0 \end{aligned}$$

These ordinary differential equations have the following solutions:

$$\begin{aligned} \eta(t) &= A * \cos(\omega t) + B * \sin(\omega t) + IC \\ \phi(x) &= C * \cos\left(\frac{\omega}{c} x\right) + D * \sin\left(\frac{\omega}{c} x\right) + BC \end{aligned}$$

- A, B, C, D: non-dimensional coefficients.
- A, B: depend on the initial conditions.
- C, D: depend on the boundary conditions.

Applying the boundary conditions (BC) for a clamped-clamped string, requires imposing a zero transversal displacement at the string's extremes:

$$\begin{aligned} y(0, t) &= 0 \\ y(L, t) &= 0 \end{aligned}$$

This means that:

$$\begin{aligned}\phi(0) &= 0 \\ \phi(L) &= 0\end{aligned}$$

At $x = 0$:

$$\phi(0) = C * \sin(0) + D * \cos(0) = D = 0$$

At $x = L$:

$$\phi(L) = C * \sin\left(\frac{\omega}{c}L\right) = 0$$

$$\Rightarrow \sin\left(\frac{\omega}{c}L\right) = 0 \Rightarrow \left(\frac{\omega}{c}L\right) = \pi * i, \text{ where } i = 1, 2, 3, \dots$$

$$\Rightarrow \omega_i = \frac{\pi * i}{L} \sqrt{\frac{T}{\rho A}}$$

$$\Rightarrow f_i = \frac{i}{2L} \sqrt{\frac{T}{\rho A}}$$

B.2 Procedure to obtain the natural frequency of the equivalent shaft in torsion model.

To obtain the expression of natural frequency of the torsion model, an equivalence between the continuous system and the discrete system should be made. This will require obtaining the wave equation for the shaft in torsion, and then substituting parameters that appear on this wave equation with ones that describe the discrete system. For this reason, this approach can be considered as in-between the continuous and discrete models.

The FBD of a portion of the shaft in torsional loading is shown in Figure B.2.

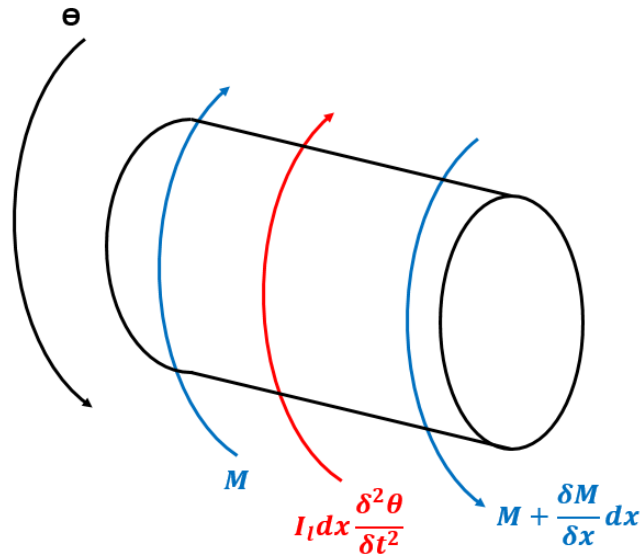


Figure B.2. FBD of the shaft in torsion.

The equilibrium of the system is performed by considering a rotation along the centerline of the shaft.

$$\curvearrowright) \left(M + \frac{\delta M}{\delta x} dx \right) - M - I_l dx \frac{\delta^2 \theta}{\delta t^2} = 0$$

Elaborating this expression, the wave equation for the shaft in torsion is obtained.

$$\frac{\delta^2 \theta}{\delta t^2} = \frac{GJ}{I_l} \frac{\delta^2 \theta}{\delta x^2}$$

- θ : rotation coordinate of the shaft.
- x : longitudinal coordinate of the shaft.
- $G \left[\frac{N}{m^2} \right]$: shear modulus of the shaft material.
- $J [m^4]$: polar moment of inertia of the shaft.
- $I_l [kg * m]$: mass moment of inertia of the shaft per unit length.

The general solution of the wave equation is given as:

$$\theta(x, t) = \eta(t)\phi(x)$$

- $\eta(t)$: time function.
- $\phi(x)$: shape function.

Substituting this solution in the wave equation expression, we obtain:

$$\frac{1}{\eta(t)} \frac{\delta^2 \eta(t)}{\delta t^2} = c^2 \frac{1}{\phi(x)} \frac{\delta^2 \phi(x)}{\delta x^2} = -\omega^2$$

- $\omega \left[\frac{rad}{s} \right]$: frequency of the string.
- $c \left[\frac{m}{s} \right]$: wave propagation speed in the string.

The solution of the equation is separated in time dependent and space dependent terms.

$$\begin{aligned} \ddot{\eta} + \omega^2 \eta &= 0 \\ \phi'' + \left(\frac{\omega}{c} \right)^2 \phi &= 0 \end{aligned}$$

These ODEs have the following solutions:

$$\begin{aligned} \eta(t) &= A * \cos(\omega t) + B * \sin(\omega t) + IC \\ \phi(x) &= C * \cos\left(\frac{\omega}{c} x\right) + D * \sin\left(\frac{\omega}{c} x\right) + BC \end{aligned}$$

- A, B, C, D: non-dimensional coefficients.
- A, B: depend on the initial conditions.
- C, D: depend on the boundary conditions.

Applying the boundary conditions (BC) for a clamped-clamped shaft, requires imposing zero rotation at its extremes:

$$\begin{aligned} \theta(0, t) &= 0 \\ \theta(L, t) &= 0 \end{aligned}$$

This means that:

$$\begin{aligned} \phi(0) &= 0 \\ \phi(L) &= 0 \end{aligned}$$

At $\theta = 0$:

$$\begin{aligned} \phi(0) &= C * \sin(0) + D * \cos(0) = D = 0 \\ \Rightarrow \phi(x) &= C * \sin\left(\frac{\omega}{c} x\right) \end{aligned}$$

At $\theta = L$:

$$\begin{aligned}\phi(L) &= C * \sin\left(\frac{\omega}{c}x\right) = 0 \\ \Rightarrow \sin\left(\frac{\omega}{c}L\right) &= 0 \Rightarrow \left(\frac{\omega}{c}L\right) = \pi * i, \text{ where } i = 1,2,3, \dots \\ \Rightarrow \omega_i &= \frac{\pi * i}{L} \sqrt{\frac{GJ}{I_l}} \\ \Rightarrow f_i &= \frac{i}{2L} \sqrt{\frac{GJ}{I_l}}\end{aligned}$$

These was the procedure to obtain the natural frequency expression for the shaft in torsion. As can be seen, the frequency depends on material and cross-section properties, which in the case of the track chain cannot be easily defined, due to the irregularity of the chain's cross-section. At this point, it is useful to define a link between the parameters of the continuous system and an equivalent discrete system. The procedure to do this is taken from a practical lecture held in the course of Mechanical System Dynamics^[ref]. To pass from the MDOF system to the continuous system, the following step is performed:

$$c^2 = \frac{GJ}{I_l} \left[\frac{Pa * m^4}{\frac{kg * m^2}{m}} \right] = L^2 \frac{k_t}{I} \left[m^2 \frac{\frac{Nm}{rad}}{kg * m^2} \right]$$

In this way, the expression of the wave speed is expressed through parameters that describe a discrete system, and that in our case, can be obtained directly from ATV. For this reason, the wave equation of the equivalent clamped shaft in torsion becomes:

$$f_i = \frac{i}{2L} \sqrt{\frac{k_t}{nI}}$$

B.3 Procedure to obtain the natural frequency expression of the equivalent Euler-Bernoulli beam model.

The FBD of a portion of a Euler-Bernoulli beam is shown in Figure B.3.

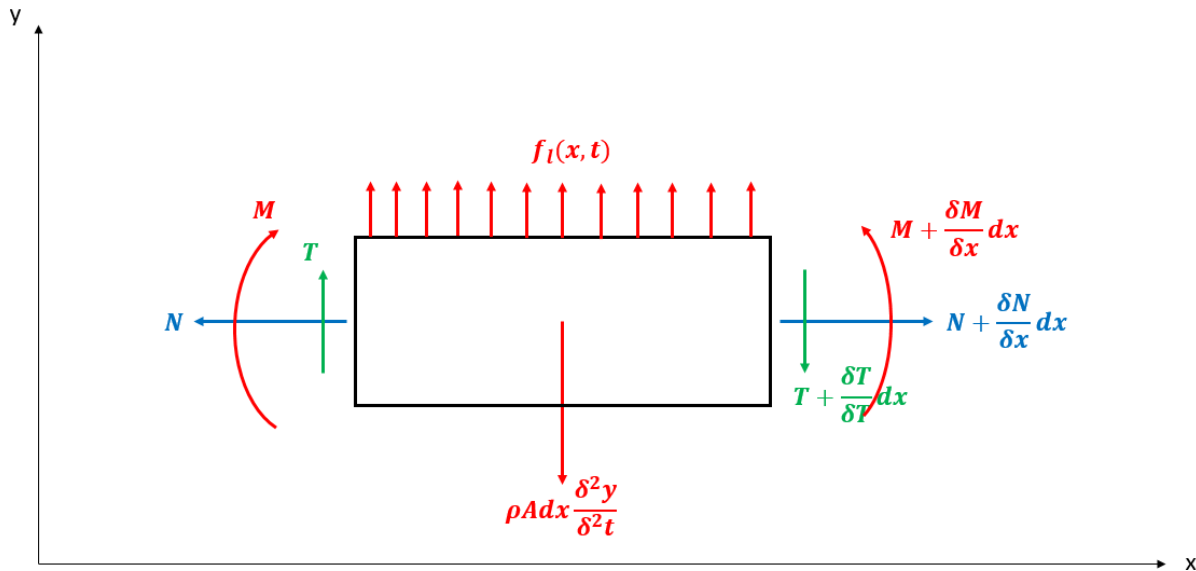


Figure B.3. FBD of the Euler-Bernoulli beam.

Performing the equilibrium in the vertical direction and around the center of mass of the beam portion:

$$\begin{aligned} \downarrow) \quad & \left(T + \frac{\delta T}{\delta x} dx\right) - T - f_l(x, t) dx + \rho A dx \frac{\delta^2 y}{\delta t^2} = 0 \\ \curvearrowright) \quad & \left(M + \frac{\delta M}{\delta x} dx\right) - M - \left(T + \frac{\delta T}{\delta x} dx\right) * \frac{dx}{2} - T * \frac{dx}{2} = 0 \end{aligned}$$

Elaborating these expression, it is possible to obtain the wave equation for the Euler-Bernoulli beam:

$$\frac{\delta^2 y}{\delta t^2} = - \frac{EJ}{\rho A} \frac{\delta^4 y}{\delta x^4}$$

- y : vertical coordinate of the beam displacement.
- x : longitudinal coordinate of the beam displacement.
- $E \left[\frac{N}{m^2} \right]$: Young's modulus of the beam material.
- $J [m^4]$: second order area moment of inertia of the beam's cross-section.

- $\rho \left[\frac{kg}{m^3} \right]$: beam density.
- $A [m^2]$: beam cross-section area.

As can be seen, the shape term of the wave equation for the Euler-Bernoulli beam is a fourth order PDE, so the shape function will have a slightly different form from the previous cases.

$$\phi(x) = A * \cos(\beta x) + B * \sin(\beta x) + C * \cosh(\beta x) + D * \sinh(\beta x)$$

- A, B, C, D: constants that depend on BC.
- $\beta^4 = \frac{\rho A}{EJ} \omega^4$

Imposing the BC for a pinned-pinned beam, implies zero displacements and zero bending moments at the extremes of the beam.

Zero displacement:

$$\begin{aligned} y(0, t) = 0 &\Rightarrow \phi(0) = 0 \\ y(L, t) = 0 &\Rightarrow \phi(L) = 0 \end{aligned}$$

This means that:

$$\begin{aligned} M(0) = EJ \left[\frac{\delta^2 y}{\delta x^2} \right]_{x=0} = 0 &\Rightarrow \phi''(0) = 0 \\ \phi(L) = EJ \left[\frac{\delta^2 y}{\delta x^2} \right]_{x=L} = 0 &\Rightarrow \phi''(L) = 0 \end{aligned}$$

$$\Rightarrow \phi(x) = B * \sin(\beta x) + D * \sinh(\beta x)$$

The characteristic equation of the beam is:

$$2 * \beta * \sin(\beta L) * \sinh[\beta L] = 0$$

The solution of this characteristic equation can be analytically computed, since this equation is very easy.

$$\sin(\beta L) = 0 \Rightarrow \beta L = \pi * i \Rightarrow \omega^2 = \beta^4 \frac{EJ}{\rho A}$$

$$\Rightarrow \omega_i = \frac{\pi^2 * i}{L^2} \sqrt{\frac{EJ}{\rho A}}$$

$$\Rightarrow f_i = \frac{\pi * i}{2L^2} \sqrt{\frac{EJ}{\rho A}}$$

For what concerns the discrete models, the procedure to develop them was already detailed in their respective sections.

References

- [1] Wong, J.Y. (2010) *Terramechanics and Off-Road Vehicle Engineering*, 2nd ed., London: Elsevier.
- [2] Galvagno, E., Rondinelli, E. and Velardocchia, M. (2012) 'Electro-mechanical transmission modelling for series-hybrid tracked tanks', *Int. J. Heavy Vehicle Systems*, Vol. 19, No. 3, pp.256–280.
- [3] Lessem, A.S. and Murphy, N.R. Jr. (1972) 'Studies of the dynamics of tracked vehicles'
- [4] Madsen, J. and Negrut, D. (2010) 'Methods for Tracked Vehicle System Modeling and Simulation'
- [5] Galvagno, E. (2024-2025) 'Mechanical System Dynamics', Mechanical System Dynamics course, Politecnico di Torino, academic year 2024-2025.
- [6] Galvagno, E. (2023-2024) 'Motor Vehicle Mechanics', Motor Vehicle Mechanics course, Politecnico di Torino, academic year 2023-2024.
- [7] "Mechanical vibration — Road surface profiles — Reporting of measured data", International Standard, BS ISO 8608:2016